Development of electrode array based biosensors for detecting the activity of cancer related proteases

by

Yang Song

B.S., Hebei Normal University of Science and Technology, 2011

M.S., Hunan Normal University, 2014

AN ABSTRACT OF A DISSERTATION

submitted in partial fulfillment of the requirements for the degree

DOCTOR OF PHILOSOPHY

Department of Chemistry
College of Arts and Sciences

KANSAS STATE UNIVERSITY
Manhattan, Kansas

2020

Abstract

As an essential biomolecule involved in many physiological and metabolic processes, proteases are potential targets in cancer diagnosis and therapy. We have developed an electrochemical method for measuring the activity of proteases using two different working electrodes: vertically aligned carbon nanofiber nanoelectrode arrays (VACNF NEAs) and gold microelectrode arrays (MEAs). A conductive Cr layer coated on SiO_2-covered Si chip served as the substrate for the growth of VACNFs which were subsequently encapsulated in a SiO_2 matrix. After polishing and reactive ion etching, VACNF tips were exposed to form a NEA. Specifically designed ferrocene (Fc) labeled peptide substrates were covalently functionalized to the exposed NEA tips. The Fc moiety at the distal end of the peptide can be oxidized and measured with AC voltammetry (ACV). Compared with ordinary macro-electrodes, VACNF NEA has distinct properties due to its unique structure. The optimal ACV frequency is up to 1 kHz, enabling the kinetic measurement of proteolysis of surface-functionalized peptides by proteases. Different peptide substrates (tetrapeptide, hexapeptide, and octapeptide), designed and synthesized in Hua's laboratory, have been used to functionalize the VACNF NEA. The detected proteolysis rate is highest for the hexapeptide, followed by the octapeptide and tetrapeptide. These results indicate the potential of using hexapeptide as a peptide probe for protease activity profiling of specific cancer-relevant proteases.

In another study, we fabricated a gold MEA for multiplex protease activity profiling. The MEA contains nine individual microelectrodes, which have dimensions of 200 x 200 micrometers. The MEA shows highly consistent cyclic voltammetry signals in Au surface cleaning experiments and reliably detects benchmark redox species in solution, which indicates the identical surface area and electrochemical activity of the electrodes. The individual Au microelectrodes were selectively

functionalized with three different Fc-labeled peptide substrates. The proteolytic kinetics were profiled by monitoring the Fc oxidation signal through AC voltammetry as the peptide substrates were cleaved by cathepsin B. Cathepsin B activity was derived with an improved fitting algorithm and the heterogeneous Michaelis-Menten model. The multiplex functionalization of an Au MEA for simultaneous detection of the proteolysis of cathepsin B on a single chip shows the potential of this sensor platform for a fast and multiple protease activities profiling in various diseases, including different types of cancer. The Au MEAs were further explored for detecting multiple proteases (such as cathepsin B and ADAM-17) in a common physiology-compatible buffer at pH = 7.4 for measuring human serum samples. This Au MEA shows a great potential toward multiplex detection.

Development of electrode array based biosensors for detecting the activity of cancer related proteases

by

Yang Song

B.S., Hebei Normal University of Science and Technology, 2011
M.S., Hunan Normal University, 2014

A DISSERTATION

submitted in partial fulfillment of the requirements for the degree

DOCTOR OF PHILOSOPHY

Department of Chemistry
College of Arts and Sciences

KANSAS STATE UNIVERSITY
Manhattan, Kansas

2020

Approved by:

Major Professor
Dr. Jun Li

Copyright

Abstract

As an essential biomolecule involved in many physiological and metabolic processes, proteases are potential targets in cancer diagnosis and therapy. We have developed an electrochemical method for measuring the activity of proteases using two different working electrodes: vertically aligned carbon nanofiber nanoelectrode arrays (VACNF NEAs) and gold microelectrode arrays (MEAs). A conductive Cr layer coated on SiO_2-covered Si chip served as the substrate for the growth of VACNFs which were subsequently encapsulated in a SiO_2 matrix. After polishing and reactive ion etching, VACNF tips were exposed to form a NEA. Specifically designed ferrocene (Fc) labeled peptide substrates were covalently functionalized to the exposed NEA tips. The Fc moiety at the distal end of the peptide can be oxidized and measured with AC voltammetry (ACV). Compared with ordinary macro-electrodes, VACNF NEA has distinct properties due to its unique structure. The optimal ACV frequency is up to 1 kHz, enabling the kinetic measurement of proteolysis of surface-functionalized peptides by proteases. Different peptide substrates (tetrapeptide, hexapeptide, and octapeptide), designed and synthesized in Hua's laboratory, have been used to functionalize the VACNF NEA. The detected proteolysis rate is highest for the hexapeptide, followed by the octapeptide and tetrapeptide. These results indicate the potential of using hexapeptide as a peptide probe for protease activity profiling of specific cancer-relevant proteases.

In another study, we fabricated a gold MEA for multiplex protease activity profiling. The MEA contains nine individual microelectrodes, which have dimensions of 200 x 200 micrometers. The MEA shows highly consistent cyclic voltammetry signals in Au surface cleaning experiments and reliably detects benchmark redox species in solution, which indicates the identical surface area and electrochemical activity of the electrodes. The individual Au microelectrodes were selectively

functionalized with three different Fc-labeled peptide substrates. The proteolytic kinetics were profiled by monitoring the Fc oxidation signal through AC voltammetry as the peptide substrates were cleaved by cathepsin B. Cathepsin B activity was derived with an improved fitting algorithm and the heterogeneous Michaelis-Menten model. The multiplex functionalization of an Au MEA for simultaneous detection of the proteolysis of cathepsin B on a single chip shows the potential of this sensor platform for a fast and multiple protease activities profiling in various diseases, including different types of cancer. The Au MEAs were further explored for detecting multiple proteases (such as cathepsin B and ADAM-17) in a common physiology-compatible buffer at pH = 7.4 for measuring human serum samples. This Au MEA shows a great potential toward multiplex detection.

Table of Contents

List of Figures

List of Tables

Acknowledgements

First, I would like to thank my advisor, Dr. Jun Li, for his support in the past five and a half years. I am admired for his hardworking attitude and profound knowledge. Without his pushing, my Ph.D. period will not be such splendid.

I would also like to thank former and present members in Dr. Jun Li's group: Dr. Morgan Anderson, Dr. Foram Madiyar, Dr. Emery Brown, Dr. Ayyappan Elangovan, Dr. Yiqun Yang, Dr. Tao Liu, Kamalambika Muthukumar, Archana Sekar, Fahat Kurshid, Sabari Rajendran, Levan Leban, and Gage Wright. Thanks Dr. Emery Brown for helping me on SEM images and carbon nanofiber growth. Thanks the help from Foram Madiyar in the nanoelectrode fabrication. Thanks Dr. Morgan Anderson and Gage Wright for all the help on the protease detection project. The Au MEA chip was fabricated and SEM imaged by Dr. Morgan Anderson at NASA Ames Research Center and Stanford University. Part of the electrochemical measurements and ELISA experiments were operated by Gage Wright.

I express my gratitude to my committee member. Professor Duy Hua designed all peptide substrates which have been used in this study. Professor Christopher Culbertson, and Professor Kunyan Zhu for the guidance and help on my doctoral program. I also want to thank Professor Michael Kanost to serve as an outside chair in my final defense exam.

Special thanks to Professor Huafang Fan and Zhaoyang Ren in Hua's laboratory for the design and synthesis of substrate peptides and all HPLC characterization. Without these specific peptide substrates, we could not publish the electronic biosensor manuscripts. I would also like to thank the staffs in the chemistry department who gave me great help: Ron Jackson for all the mechanical work, Tobe Eggers for saving my computer and instruments uncountable times, Jim

Hodgson for all those brilliant glassware jobs, and Bart Bath for calling the vendor to push the progress of the purchase order.

Finally, I would like to give thanks to my family for their unconditional love and support. Without my parents' love, guidance, and discipline, I would have no chance to go this far. Special thanks to my wife, Zhongjie Li, and son Karl. Thank you for making my days brighter.

Dedication

“To my beautiful wife Jie and lovely son Karl”

Preface

This dissertation consists of the following sections:

Chapter 1. Introduction of biosensors and the application of nanomaterials for biosensors. In addition, several traditional and modern techniques toward protease detection are discussed. This part also provides the motivation to develop a fast and reliable biosensor for protease detection.

Chapter 2. Description of vertically aligned carbon nanofiber nanoelectrode arrays (VACNF NEAs) fabrication and characterization. The surface functionalization of VACNF NEAs with peptide substrate are discussed as well.

Chapter 3. A paper published in *Analytical Chemistry*. This chapter describes an electrochemical method using ferrocene-labeled peptide sequence functionalized VACNF NEAs to profile cathepsin B activities. Using the heterogeneous Michaelis-Menten model, the activity of cathepsin B is defined by the "specific constant" k_{cat}/K_m. This is the first example of using three peptide substrates with different length on the study of protease activities. The study demonstrates that the proteolysis rate of cathepsin B on hexapeptide is higher than that from tetrapeptide and octapeptide substrates.

Chapter 4. A paper published in *Biosensors and Bioelectronics*. This chapter describes a gold microelectrode array (Au MEA) for cathepsin B activity profiling. A modified algorithm is introduced to fit the exponential decay, which gives better fitting quality. Moreover,

the MEA is successfully functionalized with three different substrates for cathepsin B activity detection, illustrating the potential for further multiplexed detection by using this MEA.

Chapter 5. ELISA experiments for a manuscript in preparation. This chapter discusses the ELISA test on pooled human serum and the cathepsin B spiked diluted human serum. The purpose of this chapter is to use a standard method to detect the cathepsin B level in real patient samples and to compare them with the electrochemical method result.

Chapter 6. Summary of the major finding of the work and discussion of the future direction for the VACNF NEA biosensor and Au MEA biosensor.

Chapter 1 - Introduction

1.1 Principles and Significance of Biosensors

Principles

Biosensor is an analytical device that presents a synergistic combination of biotechnology and microelectronics.[1] Typically, there are three components in biosensor: a biorecognition component (also called bioreceptor, which includes enzyme, antibody, DNA, etc.); a transducer (usually use electrochemical, optical, thermal, mass, etc. techniques); and a signal amplification unit. The purpose of developing a biosensor is to detect small molecules to monitor human health, lethal pathogen or environmental pollutants rapidly and at a low cost. These small molecules, also called analytes, can interact with biorecognition elements by kinetic reaction based on the specific metabolic catalytic activity (such as enzymes) or changing the structure of the surface through specific binding with the bioreceptor (such as DNA probes, pathogen or antibody) (Figure 1.1). Both strategies work towards the fundamental aims of changes in the biochemical signal which is converted by the transducer and processed by the signal amplifier unit. Based on the transduction mechanisms, there are several transducer categories, such as mass biosensors, electrochemical biosensors and optical biosensors.

A mass biosensor is based on the mass change induced by the interaction between the analyte and the sensor surface. For example, the piezoelectric biosensor is based on the resonant frequency change of an oscillating piezoelectric crystal, which is caused by the increased mass due to the adsorption of analyte on the functionalized crystal surface. The applications of the piezoelectric biosensors include the study of the interaction of DNA and RNA with complementary sequences, specific recognition of protein ligands by immobilized receptors and virus or bacteria detection, as demonstrated in many immunosensors.[2]

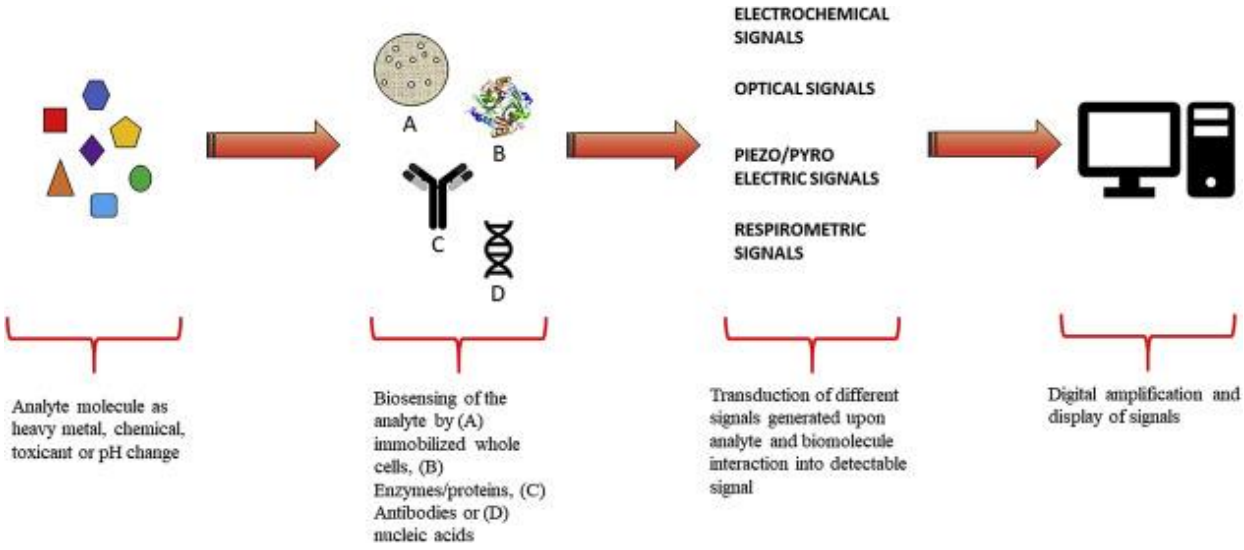

Figure 1.1 Description of different component of biosensors.[3] (Adapted with permission from ref. 3. Copyright © 2019 Elsevier Publisher. License number: 4875570933799.)

An optical sensor is a powerful detector and analytical tool. It usually involves two detection protocols that can be implemented in optical sensing: label-free detection and labeled detection. In label-free detection, the target molecules are not labeled, and they are detected in their natural forms. This design makes it to be a cheap platform and allows it to measure the kinetic molecular interaction quantitatively. In labeled detection, either the target molecules or bio-recognition units are labeled with optical tags (such as fluorescence molecules). These fluorescence labeling tags emit fluorescence after excited by a light source with a certain wavelength. The fluorescence intensity reveals the amount of the bound analytes which is defined by the interaction strength between target molecules and the biorecognition units and the concentration of the target molecules in the sample. Compared with label-free detection, fluorescence-labeled detection is sensitive but expensive and requires a laborious labeling process. The fluorescence tag may also affect the biofunctions of the target molecules.

The electrochemical sensor is based on the change in electron transfer rate, which is caused by the interaction between the target molecule and the biorecognition component. Among the biosensors, the electrochemical biosensor is of particular interest because of their simplicity of fabrication, fast response, low cost, and high sensitivity.[4] The transduction of the chemical signal to an electrical signal can be done by voltammetry, potentiometry, impedance spectroscopy, or amperometry. The voltammetric and amperometric sensors measure the current-potential relationship in an electrochemical cell. In the case of amperometry, a potential is applied on the cell, and the current is measured, and there must be an electroactive reagent that can undergo a redox reaction at the electrode.[5] However, in potentiometry, the voltage is measured without any current pass through the cell. The impedance sensor measures the response in the resistance and capacitance across the electrode electrolyte interface. The impedance signal is sensitive to the change in the electric double layer structure following analyte capture.[6] Since there is no need to set a reference electrode in the impedance sensor system, the change in capacitance is easier to measure, and the whole sensor is more durable. However, the biggest challenge of the impedance sensor is the nonspecific binding and the low sensitivity.

Besides classifying the biosensor according to the signal transduction method, another strategy to classify the biosensor is based on the bioreceptor: concentration-based biosensor and activity-based biosensor. The former focuses on the quantification of the overall concentration of the target. Enzyme-linked immunosorbent assays (ELISA) is a good example. These concentration-based methods use the antibodies to bind the epitopes on the antigen selectively, but they usually cannot distinguish the inactive target like proenzyme Thus they cannot provide accurate information regarding the biological function (such as activity) of the target enzymes. The second category focuses on the quantification of the activity of the target. The significant

difference comparing to the former one is that it tells the activity of the target enzymes instead of the overall concentration, especially the overall enzyme concentration may vary drastically from different sources of the patient. The activity of certain enzymes in cancer patients gives more information about the cancer progress than the enzyme concentrations.

For biosensor design, there are several aspects to be considered: (1) Accuracy: false positive or false negative should be as low as possible; (2) Sensitivity: it is desired to increase the sensitivity and decrease the detection limit as much as possible; (3) Specificity: the biosensor should easily discriminate the target molecule from the sample matrix; (4) Reproducibility: Each experiment should be highly reproducible, which is a fundamental criterion for all sensors; (5) Assay time: the ultimate goal of a biosensor is to do a point-of-care test, which requires biosensors to have a real-time response; (6) User friendly: the biosensor should only require minimal operator skills for routine detection.[7]

Significance

Cancer is the second most important cause of death in the world, after cardiovascular disease. In 2012, there were 14.1 million new cancer cases, and over half of them occurred in the underdeveloped areas. In 2015, there were 8.8 million deaths and over two-third of which occurred in the underdeveloped areas. The WHO estimates that by 2030, there will be 23.6 million new cases of cancer each year.[8] Also, the cost of cancer patients' treatment is expensive. If we take breast cancer as an example, the average price of 0 to 12 months for stage 0 patient is more than 60k dollars, 82k dollars for stage I/II patient, 129k dollars for stage III patient, and 134k for stage IV patient. In the meantime, the survival rate has dramatically decreased with the cancer

progression, from 100% (stage 0) to 28% (stage IV).[9] Thus, there is an urgent need for a fast and accurate method to diagnose cancer as early as possible.

1.2 Nanomaterials for biosensors

In the last two decades, nanomaterials show great promise for the development of biosensors. Because of their nanoscale dimension, quantum-size effect, and large surface area, nanomaterials exhibit unique chemical, physical, and electric properties compared with the traditional bulk materials. For example, nanomaterials have an excellent electronic property, and electrocatalytic effect. This property facilitates the electron transfer between the enzyme's redox center and the electrode, and decreases the working potential of the reaction, which is an important factor in amperometric biosensor design. Secondly, the favorable catalytic properties of nanomaterials can reduce the overpotential of electrochemical reactions and omit the need for chemical mediators. Thirdly, the high surface-to-volume ratio guarantees a high bioreceptor loading, which leads to much higher sensitivity and lower detection limit than traditional bulk material-based biosensor. Another reason to cause the lower detection limit is the high signal to noise (S/N) ratio and high surface energy of the nanomaterials. High surface free energy prompts the adsorption of the biomolecules on the nanomaterials. Moreover, the nanomaterials have a similar dimension with the biomolecules, which make it possible to generate a novel functional hybrid system that show promising analytical behavior.[10-11] Currently, there are many kinds of nanomaterials like nanoparticles (0 D), nanorods (1D), nanotubes (1 D), nanoclusters (0 D), which have been used in biosensor system where they have been shown to improve the performance of biosensors (Figure 1.2).[12] Here, I present some representative nanomaterials which have been widely used in biosensor design.

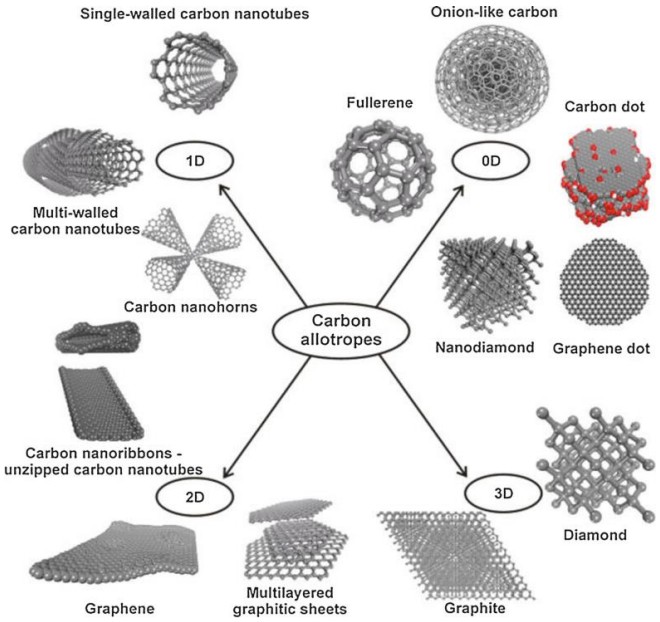

Figure 1.2 Different types of carbon nanomaterials.[13] (Adapted with permission from ref. 13. Copyright © 2015, American Chemical Society.)

Carbon nanotubes (CNTs)

Carbon nanotubes have a hollow cylindrical structure which contains one or more concentric graphite layers. The end of the tube shows a hemisphere structure. As the most extensively used nanomaterial in the past decade, carbon nanotubes have numerous unique properties: high conductivity and mechanical strength, excellent thermal conductivity, chemical stability, electrocatalytic activity, and surface-to-volume ratio. CNTs based biosensors have been studied for decades in pathogen detection, disease diagnosis, environment monitoring, and food safety inspection. It also has been used as the tip of atomic force microscopy to increase the lateral resolution, which is governed by the shape of the tip and the geometry of the apex at the end of the tip.[14]

Typically, there are three ways to synthesize carbon nanotubes: arc discharge, laser ablation, and chemical vapor deposition (CVD). In arc discharge, the current through two graphite electrodes deposits CNTs on the cathode electrode. By using the metal catalyst, either SWCNTs or MWCNTs can be synthesized.[15] Laser ablation is using a silica tube loaded graphite. By applying high temperature with laser pulse and under the help of metal catalysts, MWCNTs or SWCNTs can be obtained. CVD carbon nanotube synthesis method is a widely used commercial method. It generates CNTs during the pyrolysis of hydrocarbon gases at high temperature. Changing the parameter such as temperature, gas flow rate and reagent gas allows for the control of nanotube properties, such as purity and diameter.[15-16]

As synthesized CNTs need further treatment before surface functionalization. The most common method to activate the surface is using strong acid to remove the cap of the CNTs or introduce defects on the cylinder. This treatment may also shorten the CNTs length. The consequence of acid treatment is to add oxide groups such as -OH and -COOH. As we know, -COOH group can react with the amine group to form a strong covalent amide bond. In the meantime, the defect sites and oxide groups can enhance the solubility of the CNTs in water, which is a crucial factor in biosensor fabrication. Non-covalent bond (π-π stacking) is another way to modify CNTs' surface. Both covalent and non-covalent functionalization has played a role in the electrocatalytic properties of CNFs.

Graphene

Graphene is a single atomic layer of sp^2-hybridized carbon. It has been extensively used for biosensor projects in the last two decades. Like most carbon nanomaterials, graphene has high mechanical strength, high thermal conductivity, tunable optical properties. Currently, graphene

has been extensively employed in electrochemical, fluorescence, impedance biosensor for the detection of a wide range of targets including but not limited to adenosine triphosphate (ATP), pathogen, glucose, DNA, and heavy metal ions.

Graphene has been synthesized in various ways. The first and easiest way is exfoliated of graphite. This cheap and straightforward method was found by Novoselov, Geim, and co-workers. However, this method has poor control over graphene quality. The shape of the graphene topology is usually irregular and at a size of several microns, which is not acceptable in many technological applications. Hence, synthesizing a graphene flake sample with specific azimuthal orientation and on a large scale is in urgent. In 1965, single layer graphite had been found by Hagstrom, et al. at the surface of the bulk of Pt crystals.[17] But until 1969, it was explicitly interpreted as a single layer of graphite by J.W. May.[18] After that, researchers started to study the graphite by surface segregation of carbon during annealing of carbon-doped metals. At the beginning, the carbon source gas is decomposed and dissolved in the metal, creating a concentration gradient between the bulk and surface. After saturation, the carbon atom started to secrete from the metal on the surface. Once the temperature cooled down, the carbon atom turned to the graphene layer. H_2 annealing can eliminate the impurities and make the carbon solubility uniform. Cooling rate also plays a role in the carbon segregation.[19-21]

In the biosensor field, graphene is not only referred to as a 2D nanomaterial presenting non-covalent interaction, π-π stacking, high electrostatic force, but also has a huge surface to volume ratio.[22] Hence, graphene-based biosensor usually has high sensitivity because of the extraordinary substrate loading. Like carbon nanotubes, the biomolecule can interact with graphene either through a non-covalent bond or an oxide group located at the edge and defect sites.[23]

Carbon nanofibers (CNFs)

The first carbon fiber material was prepared by carbonizing cotton and bamboo and used as the filament of the light bulb in 1879. Although CNFs have a similar fiber shape, there are some different traditional carbon fibers and CNFs. First, the size of these two is different. Conventional carbon fiber has a diameter of several micrometers. However, CNFs have a diameter of 50-200 nm.[24] Second, CNFs have diverse structures and shapes. For example, plasma enhanced chemical vapor deposition (PECVD) fabricated CNFs have a unique stacking conical structure. Electrospinning method fabricated CNFs is recognized as an easy method for producing extremely long nanofibers. Third, the preparation methods are different. Typically, traditional carbon fibers are prepared from high-strength polyacrylonitrile or mesophase pitch by using electrospinning. Thermal annealing coverts polymer to carbonized CNTs. However, CNFs are usually prepared by catalytically vapor deposition.

Like other carbon nanomaterials, the functionalization of CNFs includes physical adsorption and covalent bonding. Electrochemical techniques or strong nitric acid are often used to produce functional groups on the surface of CNFs for further modifications.[25] Different types of biosensors have been established, targeting glucose, DNA, and proteins. For example, Lee *et al.* used the electrochemical method to generate amino groups on the CNFs and finally attach the DNA sequence through the amide bonds.[26] Baker used other strategies to functionalize amino groups on the CNFs and then covalently modify DNA molecules on the CNFs.[27] Both methods successfully functionalized DNA on the CNFs and exhibiting excellent reversibility in binding to complementary sequences. In 2019, Song *et al.* used the CNFs nanoelectrode array for quantification of protease activity. They covalently functionalized ferrocene labeled peptide

sequence onto the CNFs through an amide bond. The electrochemical signal decays exponentially concerning the reaction time, and the decay time constant reflects the protease activity.[28]

Although the synthesis and application of nanomaterials for biosensing are attracting a lot of attention, it is still facing many challenges. For example, the interaction (physical adsorption or chemical immobilization) between biomolecules and nanomaterials may change the properties of the molecules, which may affect the biofunction of the molecules. How to enhance the specificity or sensitivity of nanomaterials-based biosensor is another aspect under consideration. Furthermore, currently, most biosensors are in vitro, which may cause contamination during the sampling process. If we want to implant the biosensor in the human body, biocompatibility is also challenging. Future work should focus on developing the multiplexing system and discovering novel materials which have good biocompatibility. In the meantime, we should also put effort into non-invasive biosensors for daily health monitoring.

1.3 Protease detection

1.3.1 Introduction

Proteases are one of the most important group of enzymes. It conducts proteolysis, which is the process to describe the hydrolysis of a peptide bond to degrade the polypeptide chain forming the protein. Currently, there are more than 600 protease genes have been found in humans.[29] Usually, proteases play a significant role in metabolisms, such as the digestion of food protein, cell division, and apoptosis. However, it has been proved that proteases are also an important signaling proteins that play crucial roles in many pathological processes such as cardiovascular, neurological disease and cancer. For example, proteases have been associated with tumor progression due to their ability to degrade extracellular matrices, facilitating tumor cell metastasis

and invasion to surrounding tissues (Figure 1.3).[30-31] Cathepsin B is one of the lysosomal proteases associated with breast cancer.[32] It is released from malignant human breast tumor explants and can be extracted in the serum of patients. In the process of tumor growth, invasion, and metastasis, cathepsin B is involved in the dissolution and remodeling of connective tissue and basement membrane. Up to now, there are many cancers that can be diagnosed through cathepsin B, including breast cancer,[33] colorectal cancer,[34] tongue or laryngeal carcinoma,[35-36] and pancreatic cancer.[37]

Hence, it is not surprising to see that proteases have been widely studied as potential diagnosis and therapeutic targets. For example, various biosensors are established to detect the protease level or activity in the patients, trying to diagnose the cancer patients at an early stage and to monitor treatment responses.[38] Also, recent technological developments in molecular imaging can directly identify and monitor protease in living organisms by covalent tag, thereby allowing unambiguous diagnosis of protease activities observed in imaging studies.

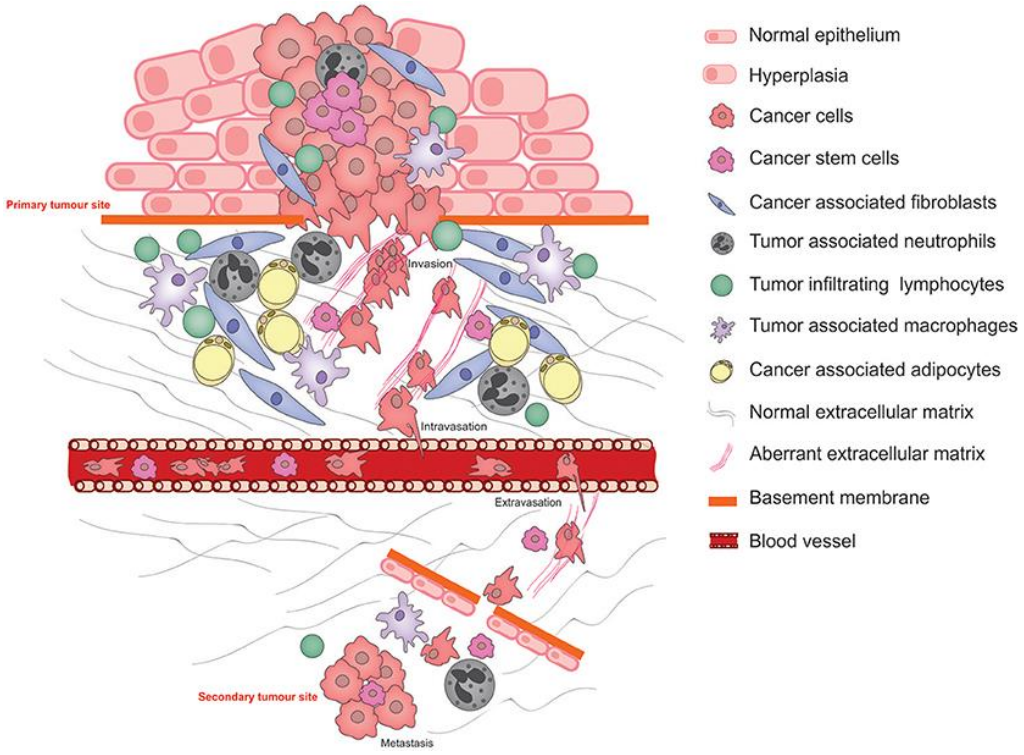

Figure 1.3 The scheme of tumor progression, invasion, and metastasis.[39] (Adapted with permission from ref. 39. Copyright © 2018 Taylor and Francis Ltd.)

1.3.2 Traditional protease detection method

Traditional protease detection methods include mass sensitive biosensor, fluorescence biosensor, surface plasmon resonance imaging, enzyme-linked immunosorbent assay (ELISA), electrochemical biosensor, and high-performance liquid chromatography (HPLC) based biosensor, etc.

Mass sensitive biosensor

The most representative mass sensitive biosensor is the quartz crystal microbalance (QCM) biosensor, which was widely applied as a sensor in the liquid phase since the 1980s. Because the QCM sensor has advantages in fast analysis speed, simple design, low cost, and sensitivity, more

attention has been paid. Currently, the QCM sensor has been developed as real-time and *in situ* detection by passing the sample through a modified QCM sensor. The commercialization of QCM has also been achieved on agriculture and other industries applications. Typically, antibody plays an important role in the fabrication of the QCM sensor. They are either covalently or non-covalently combined on the Au surface, which is usually used as a surface of QCM. Regardless of what kind of method is chosen, the objective is to immobilize as much antibody as possible on the QCM sensor surface and make sure that the active sites of the antibody are exposed outwards.[40] Apart from the antibody, the peptide-based thin film was explored as a bioreceptor as well. Stair *et al.* found simple imine linkages between aldehyde groups in oxidized dextran, and a peptide sequence can form hydrogel cross-links. This peptide sequence is susceptible to protease cleavage.[41] Thus, they obtained a direct relationship between the hydrogel degradation rate and protease activity. However, there are some limitations to the QCM sensor. For example, QCM sensor lacks the ability for multiplexed detection.

Surface plasmon resonance imaging

The surface plasmon resonance imaging (SPRI) technique is a promising tool to investigate the label-free protein-protein interactions, as well as for the development of biosensors for biomolecules.[42] Typically, one of the interacting proteins is immobilized onto a chip surface to interact with the other protein in the solution. The refractive index changes due to the target proteins bound to the sensor surface, and the change alters the coupling condition between the light wave and the surface plasmon, which finally captured by the SPRI sensor. In 2011, Gorodkiewicz *et al.* have developed a method for highly selective determination of protease using the SPRI technique. This method based on the highly selective covalent binding between one of the subunits

of protease and immobilized inhibitors. The inhibitor is a peptide aldehyde, which covalently binds to the N-terminal ThrlOγ located on the protease subunits and powerfully and reversibly blocks the catalytic center of the protease.[43]

Fluorescence biosensor

During the 1970s, fluorescence quenching mechanism has been used to measure oxygen in microenvironment.[44] Today, fluorescence-based biosensors have become critical players in monitoring cellular, molecular dynamics and cell-cell interaction. As one of the most widely used fluorescence biosensors, fluorescence resonance energy transfer (FRET) biosensor is based on chemical transduction. It requires the utilization of donor and acceptor fluorophores. FRET can only allow energy transfer when the distance between the donor and the acceptor fluorophores are within about 10 nm. The excited donor emits an essential virtual photon, and the photon is then adsorbed by the acceptor.[45] The donor and acceptor can be brought together in several ways, including covalently attached to DNA or peptide sequence (Figure 1.4). Alternatively, the donor and acceptor can be attached to the same protein. Due to the environmental constraints, the conformation change forces the donor and acceptor approaching each other, then initial FRET.[46]

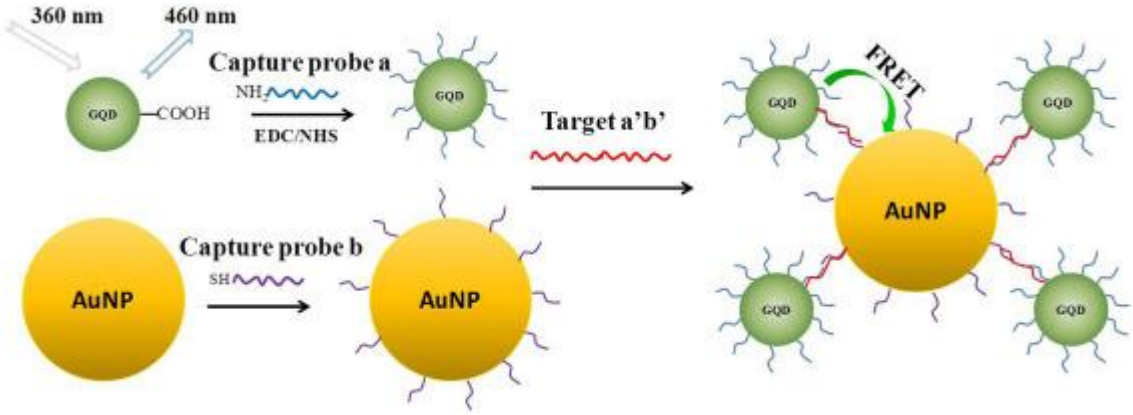

Figure 1.4 Schematic of FRET-based biosensor for S. aureus gene detection.[47] (Adapted with permission from ref. 47. Copyright © 2015 Elsevier.)

Although FRET is a useful technique in biosensor fabrication, it still has limitations. The first limitation is the donor fluorophore emission range, and the acceptor fluorophore excitation range must overlap by at least 30%.[48] This limitation dramatically narrows down the available choices of fluorophore donors and acceptors. Another limitation is the auto-fluorescence. It is known that some organelles can release energy in the form of the photon after excited by light photons, such as mitochondria and lysosomes. These photons can be detected by the sensor and cause high background signal to interfere with the expected signal. Photobleaching is also a disadvantage in FRET biosensors.

ELISA

ELISA is an antigen-antibody binding method used to measure the concentration of antigens in a sample.[49] It was introduced by Peter Perlmann and Eva Engvall in 1971. This method requires the antibody to be immobilized on a surface to quantify an antigen. The amount of captured antigen is proportional to the amount of antigen present in the sample. Using

spectrophotometry to measure the conversion of a clear substance to a colored product by the enzyme that is linked to the antibody or antigen, the amount of antigen in the sample can be quantified. There are four major types of ELISA: direct ELISA, indirect ELISA, competitive ELISA, and sandwich ELISA (Figure 1.5). For sandwich ELISA, the surface is incubated with the first antibody (capture antibody) overnight. After washing out the unbound first antibody, the surface is passivated with bovine serum albumin (BSA). Next, the sample is added to generate the target-first antibody complex. After removing the unbound target, the second antibody (detection antibody) is added to form the sandwich structure. Following that, the enzyme-streptavidin is added to bind with the biotin modified on the second antibody. Finally, the substrate is added, converted by the enzyme into a product with specific wavelength adsorption. After 50 years, the ELISA method is still the most widely used technique in clinical diagnosis. However, it has some inevitable problems. First, long incubation time leads ELISA to be a time-consuming technique. Second, the cost of the ELISA kit is expensive because it requires a specific antibody. Third, cross-reactivity or contamination may cause a false-positive result. Hence, a skilled experiment operator is necessary.

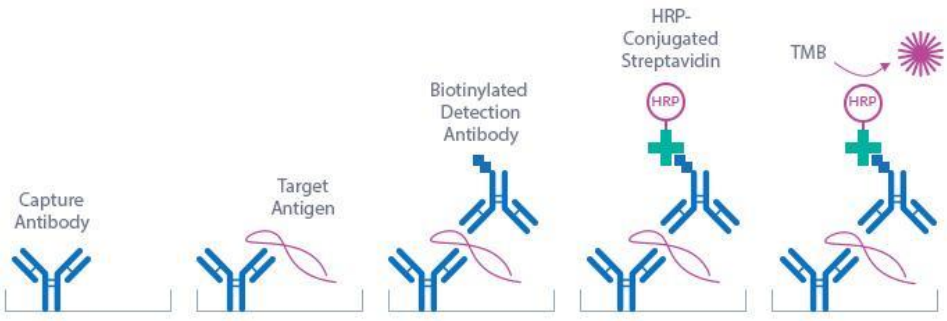

Figure 1.5 Schematic graph of sandwich ELISA experiment. (Courtesy: Biomedica. https://www.bmgrp.com/product/infectious-disease/borrelia-igm-elisa-biomedica/)

Electrochemical biosensor

Traditional electrochemical biosensors include cyclic voltammetry (CV), differential pulse voltammetry (DPV), electrochemical impedance spectroscopy (EIS), and amperometry. For the voltammetry and amperometry method, a redox tag labeled probe is required. The probe can be a DNA sequence or peptide sequence modified on traditional working electrodes such as glassy carbon electrode (GCE) or gold disk electrode. The voltage can oxidize the redox tag applied to the working electrode and gave a current passing through the electrode. The target molecule usually binds with the probe or hydrolyze these it in which the probe serves as a substrate for the proteolytic reaction. For the DNA biorecognition sequence, the most common structure is the hairpin structure. A typical hairpin-structure is a single-stranded oligonucleotide consisted of two short complementary sequences at two ends and a free sequence complementary to the target molecule in the middle.[50] The redox tag is functionalized at one end of the oligonucleotide while the other end is immobilized on the electrode surface through a covalent bond or non-covalent bond. Initially, the redox tag is close to the electrode surface because of the hairpin structure. After the free sequence is hybridized with the complementary DNA sequence, the hairpin structure will be opened and transferred to a rigid DNA duplex. The redox tag will be driven away from the electrode surface. This structural transformation changes the electron transfer rate between the redox tag and the electrode. For the peptide sequences, the hydrolysis of the peptide substrate will cause the redox tag to dissolve in the bulk solution and subsequently give a decreased signal. Finally, the concentration of the target molecule or enzyme activity can be detected by the decrease of the redox tag signal (Figure 1.6).

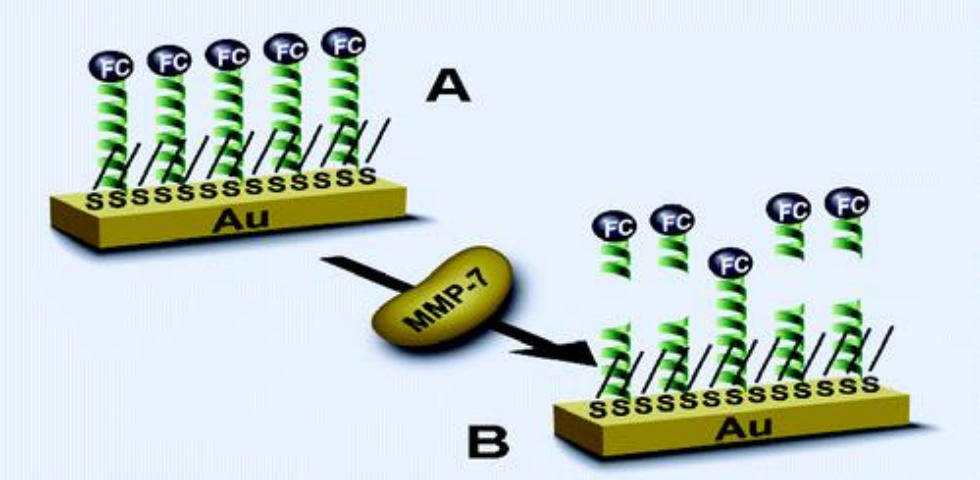

Figure 1.6 The schematic graph of electrochemical biosensor for peptide target.[51] (Adapted with permission from ref. 51. Copyright © 2006 American Chemical Society.)

1.3.3 Modern protease detection method

The modern detection method shares basic concepts with traditional detection methods but adapts modern equipment or technology with greater sensitivity and more satisfactory resolution. Therefore, the purpose of the modern technology is to improve the conventional method, leading them to fulfill higher-level requirements. For example, the electrochemical method has already been used for decades. However, the conventional technique cannot do multiplex detection. As we know, cell function and behavior are shaped by the coordinated actions of multiple biochemical activities. In the meantime, one biochemical activity may serve multiple cell functions or behavior. These activities correlate with each other and form networks. Thus, simply choosing one specific biomarker for diagnosis of the disease is meaningless and unreliable. How to enhance the sensitivity and achieve parallel profile of correlated biochemical activities simultaneously become challenging.

CNTs-based fluorescence biosensor for multiplex detection of protease

In 2013, Huang *et al*. developed a multiplex protease assay based on the FRET technique. They designed three different peptide sequences that were specific to three different cancer-related proteases, including matrix metalloprpteinase-7 (MMP-7), matrix metalloproteinase-2 (MMP-2), and urokinase-type plasminogen activator (uPA). These three substrates were labeled with a different fluorescent dye (i.e., fluorescein isothiocyanate FITC, cyanine dye Cy3, cyanine dye Cy5). By conjugating the peptide substrates on the CNTs, the fluorescence is significantly quenched due to the energy transfer from the dyes to CNTs. After incubating the functionalized CNTs with proteases, the hydrolysis of specific peptides occurs, and the dye releases from the CNTs surface, resulting in the fluorescence signal recovery. Because different peptide substrates are labeled with different fluorophores, the specific detection of the proteases is based on the respective fluorophore-labeled on each substrate.[52] This experiment offers a strategy on multiplex proteases detection. However, the fluorophore selection is the limiting factor. Balancing the resolution of the emission spectrum of different fluorophores and maximizing the throughput of multiplex detection is a great challenge. How to further improve the throughput of the biosensor is the question that we need to solve.

Multiplexed electrochemical sensor combined with microfluidics

Low-cost, high-throughput, short detection time, and high sensitivity are four requirements for modern biosensors. Electrochemical biosensors have perfectly fulfilled the requirement listed above, and it also can be miniaturized to be incorporated in a small portable electronic device. With the development of microfabrication technology, the integration of multiple electrochemical biosensors into a microfluidic device has attracted considerable attention. To successfully design

a multiplexed biosensor, the first question that should be settled is how to discriminate signals without mutual interference.[53] Multilabel system and single label but spatially resolved system are two main solutions now. The Multilabel systems emphasize the biorecognition elements labeled with different redox tags, which have distinct oxidation voltage. The benefit of this strategy is the immobilization process is simple. However, multiplex detection is challenging. For example, the redox peaks of multiple labels may overlap and have a poor resolution between two adjacent peaks. The single label can lower the cost of the material or substrate, but it needs a specific design to separate signals correlated to different targets.

Electrochemical immunoassays have been proposed in which multiple targets can be detected simultaneously by tracking variant labels. Ferrocene and thionine show great potential in a series of biosensor applications such as α-fetoprotein (AFP) and carcinoembryonic antigen (CEA) detection. The interaction of each immune recognition event generates a corresponding voltammetric redox peak. By analyzing the peaks, the concentration of each component can be obtained. Nevertheless, similar to the fluorescence sensor using multiple fluorophore labels, finding a proper redox tag is not easy. The available choices of labels limit the throughput.

The single-label strategy has the unique advantage of simplicity. The biggest challenge for this design is to discriminate different detections from a combined signal efficiently. The most direct way is to use an electrode array allowing simultaneous recognition of multiple targets. Each target only interacts with the corresponding substrate immobilized on a designed location. For example, Pursey *et al.* developed an electrode array for routine operates to detect three bladder cancer biomarkers.[54] Each electrode is immobilized with a porphyrin labeled hairpin probe. In a second example, our group has designed a 3 x 3 gold microelectrode array (Au MEA) for multiplex detection towards cancer early diagnosis. The electrodes are 200 x 200 μm and separated by 1000

μm to provide enough space to functionalize each electrode individually. According to our preliminary data, these nine electrodes can be functionalized with different ferrocene-labeled peptides and proteolyzed by cathepsin B.

Chapter 2 - Fabrication and Characterization of Vertically Aligned Carbon Nanofiber Nanoelectrode Array (VACNF NEAs)

2.1 Introduction of VACNF NEAs

As a relative novel carbon nanomaterial, plasma enhanced chemical vapor deposition (PECVD) grown vertically aligned carbon nanofibers (VACNFs) have similar conductivity and stability to CNTs. However, the inner structure of these two are different. CNFs have a distinct stacking of conical graphene sheets providing more edge sites on the outer wall, which can improve the electron transfer of electroactive species. Also, owing to the stacking graphene structure, the whole surface of CNFs can be activated either by nitric acid or electrochemical oxidation to introduce an assortment of oxygen-containing groups without degradation of the structural integrity of their backbones (Figure 2.1). Hence, the CNFs are easier for functionalization than CNTs. Especially, the surface-active groups-to-volume ratio is much higher for CNFs. Such unique properties make CNFs an extraordinary candidate for electrochemical biosensor design. Vertically aligned carbon nanofibers (VACNFs) refer a specific structure, in which CNFs are grown perpendicular to a substrate. This structure can be fabricated by plasma-enhanced chemical vapor deposition (PECVD). Both the spacing between CNFs and the diameter of CNFs can be controlled by modifying the thickness of the catalyst deposited on the substrate. It has been proven that VACNFs can be effectively functionalized with biomolecules such as peptide sequences or DNA probes through either a photochemical route or by a combined chemical and electrochemical route.[55] In this chapter, I briefly introduce the synthesis of VACNFs by the PECVD method,

followed by silicon dioxide encapsulation (silanization) and reactive ion etching (RIE) for biosensor applications.

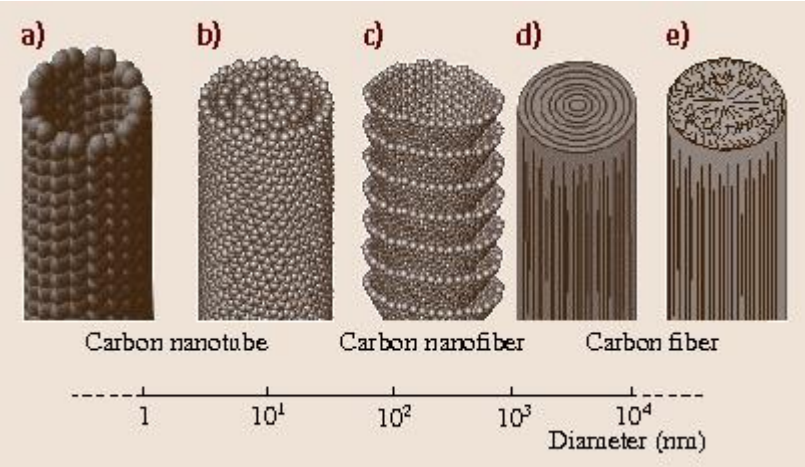

Figure 2.1 Schematic comparison of the dimensions of carbon materials.[56] (Adapted with permission from ref. 56. Copyright © 2013 Springer.)

2.2 Fabrication of VACNF NEAs

The fabrication process of VACNF NEAs includes 1) Contact and catalyst layer deposition; 2) VACNF growth by PECVD; 3) Encapsulation of VACNF NEAs, and 4) Mechanical polishing and reactive ion etching to expose the VACNF tips. More details were illustrated in the following sections.

2.2.1 Contact layer and catalyst deposition

SiO_2-covered Si substrate was cleaned with *Piranha* solution and sonicated in isopropanol for 15 min, then stored in 100 ℃ oven overnight, followed by chrome and nickel deposition. Ion beam sputtering coater was used to deposit 100 nm of Cr and 22 nm of Ni on the SiO_2 surface. The energy of the ion beam was around 9.6 keV and 8.9 keV for Cr and Ni, respectively. A 5^o

tilting, 12 °/s rocking, and 35 rpm rotating speed were applied on the sample holder during the sputtering to make the deposition more uniform. The coating rate for Cr and Ni were 1.2 Å/s and 0.7 Å/s, respectively.

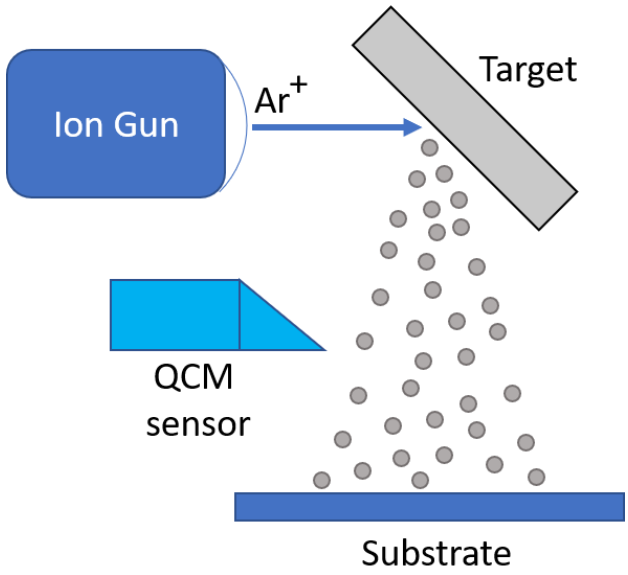

Figure 2.2 Schematic graph of ion beam sputtering coater.

2.2.2 Plasma enhanced chemical vapor deposition (PECVD) for VACNF growth

The VACNFs were grown on the Cr covered SiO_2 surface by using PECVD assisted by Ni catalyst. First, the sputtered sample was placed on a cathode graphite sample heater in the vacuum chamber under an inverted quartz jar. After boosting up the graphite heater to 500 °C for 60 s at 0.13 mbar, acetylene and ammonia were introduced into the quartz jar at flow rates of 63 and 250 sccm, respectively, which increased the processing pressure to 6.1 mbar. Then the cathode plate was heated up to 750 °C while the DC plasma was started (520 V and 45 W). Under such conditions, 35 min growth time will generate a VACNF array with the average CNF diameter of ~100 nm and a length of 5 μm on the Cr/SiO_2 surface.

2.2.3 Encapsulation of VACNF NEAs

To enhance the mechanical strength of the VACNF arrays, SiO_2 was filled into the gap between CNFs. In the meantime, non-conductive SiO_2 was able to reduce the electrochemical background from the contact Cr layer. A chemical vapor deposition (CVD) system containing a tube furnace (Thermo Electron Corporation, Asheville, NC, USA) was used in the SiO_2 deposition. The base pressure of the quartz tube furnace was ~45 mTorr, the heating element heated up the sample loaded quartz tube to 720 ℃. Tetraethyl orthosilicate (TEOS) was then introduced into the tube and filled the space between CNFs at a vapor pressure of ~195 mTorr for 6 hrs and followed by ~395 mTorr for another 6 hrs. Finally, all VACNFs were embedded in the solid SiO_2 matrix.

2.2.4 Planarization and reactive ion etching (RIE)

Twelve hours TEOS deposition introduced a 3 μm thick SiO_2 layer on top of the VACNFs. Polishing with varying diameter alumina slurries produced a mirror-like silicon dioxide surface. First, 0.3 μm alumina slurry was used for 20 min for a rough polish, then switched to 0.1 μm for another 20 min. Finally, by using 50 nm slurry for 30 min polishing, a mirror shiny SiO_2 surface was obtained. Reactive ion etching (RIE) was used to further remove the SiO_2 layer above the VACNFs. A mixture of CHF_3 and O_2 with 2 and 10 sccm flow rates, respectively, were introduced in the RIE chamber, while 200 W plasma was applied to the sample. CHF_3 selectively etched away SiO_2 with a rate of 28 nm/s. It exposed 20% to 60% of the VACNF tips based on the length variation of the fiber. The VACNF NEA used in this study has been controlled to have randomly distributed CNF tips with an average spacing around 1 μm, which corresponds to a density of ~(1-10) x 10^7 CNFs/cm^{-2}.

2.3 Characterization of VACNF NEAs

It is known that there are a lot of benefits to reduce the electrode size, such as high current density at the electrode surface and enhanced mass transport in the nanometer regime. These make the study of faster electrochemical and chemical reactions possible. Since the average diameter of VACNFs were ~100 nm, which was a nanoelectrode, it presents unique physical and chemical properties that are investigated.

2.3.1 Scanning electron microscopy characterization

Figure 2.3 shows the top view and 30° perspective view by scanning electron microscopy (SEM) with an as-grown VACNF array of 5 μm in length. These VACNFs are uniformly aligned within 5° from the surface normal. The average diameter is about 100 nm. Figure 2.3D shows a representative image of a single VACNF tip with an exposed length of about 100 nm. Only the longest VACNFs are exposed due to variation of individual VACNF length (within ±350 nm from the mean length), leaving a large average neighboring distance >1 μm between the exposed VACNF tips (indicated by the arrows in Figure 2.3C). The smaller "grass" features (~20–30 nm in size) in Figure 2.3D are polymers formed on the SiO_2 surface during RIE, which do not affect the electrochemical measurements.

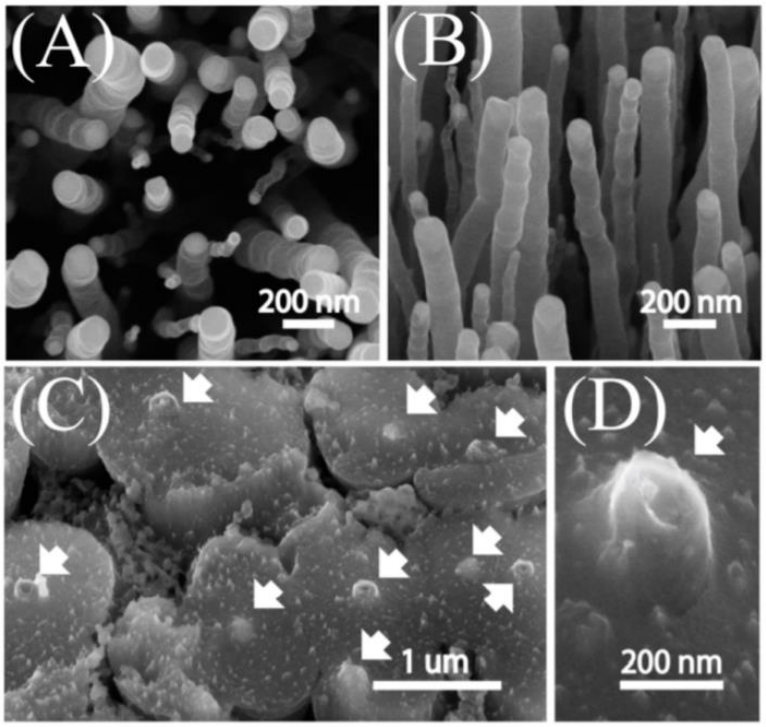

Figure 2.3 SEM images of as-grown VACNF array (A and B) and the VACNF NEA embedded in SiO_2 (C and D). A is the top view. B, C and D are 30^o tilted view. Arrows indicate the exposed tips. (SEM images was accomplished by Dr. Morgan Anderson at NASA Ames Research Center.) Copyright (2019) American Chemical Society.

2.3.2 Electrode functionalization with ferrocene

The tips of the exposed VACNF NEAs were first electrochemically etched in 1.0 M NaOH for activation. This activation process introduced carboxylic groups on the tips. It helps to functionalize ferrocene amine ($Fc\text{-}CH_2\text{-}NH_2$) on the VACNF tips by forming an amide bond facilitated by the coupling reagent EDC and NHS. Lyophilized $Fc\text{-}CH_2\text{-}NH_2$ was mixed with EDC and NHS and dissolved in DI water. The final concentrations of $Fc\text{-}CH_2\text{-}NH_2$, EDC, and NHS were 2 mM, 2 g/l, and 2 g/l, respectively. This process was finished in a hybridization cassette

(Arrayit, Sunnyvale, CA, USA) for 2 hrs at room temperature (RT). Then the electrode was rinsed with ethanol and DI water followed by drying in N_2 stream.

2.3.3 Electrochemical measurements

Electrochemical measurement involving direct current cyclic voltammetry (CV) and alternating current voltammetry (ACV) were done on CHI 440A potentiostat (CH Instrument, Austin, TX, USA) in a standard 3 electrodes system using a Teflon cell with a 2 mm diameter O-ring to seal against the working electrode (WE). Figure 2.4 shows the setup of the electrochemical cell. Platinum wire and Ag/AgCl (4M KCl with saturated Ag^+) were used as the counter electrode (CE) and the reference electrode (RE), respectively.

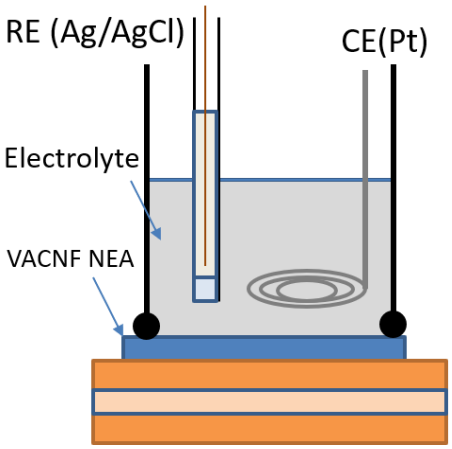

Figure 2.4 Schematic graph of the electrochemical measurement setting.

DC CV measurement of redox species in bulk solution

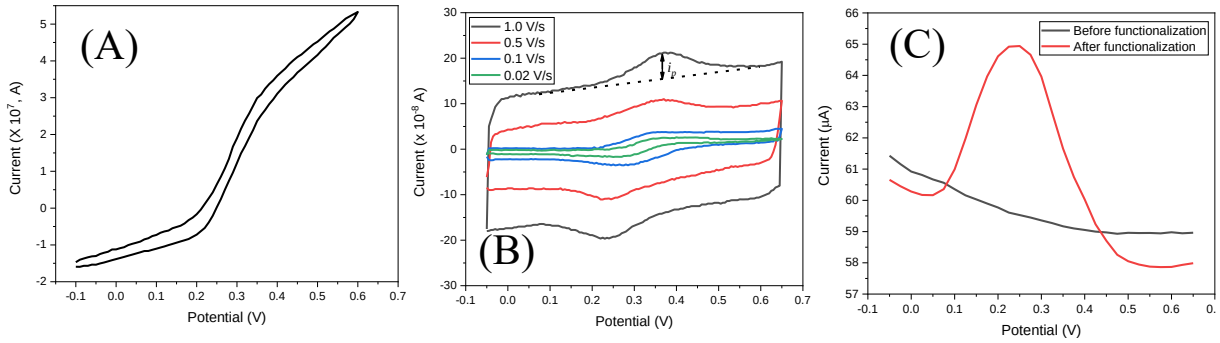

Figure 2.5 (A) CV of SiO_2 insulated VACNF NEA. The measurement was done in 50 mM $K_3Fe(CN)_6$ and 1.0 M KCl electrolyte at a scan rate of 50 mV/s. (B) CV of Fc-functionalized VACNF NEA in 1.0 M KCl. Measurements were performed at a series of scan rates of 0.020, 0.10, 0.50, and 1.0 V/s. (C) ACV of VACNF NEA before and after Fc-functionalization. Frequency and amplitude were 1000 Hz and 150 mV, respectively.

Redox species in bulk solution (50 mM $K_4Fe(CN)_6$ in 1.0 M KCl solution) were used as an electrolyte to test the performance of a VACNF NEAs using CV. CV was measured by ramping the WE potential from -0.1 to +0.6 (vs. RE) at different scan rates. Figure 2.5A is the current vs. potential. Due to the small size of the nanoelectrode, the CV curve shows a sigmoidal shape indicating the presence of a steady-state diffusion-limited current on each CNF. The CV signal is defined as the corresponding steady-state current (limiting current) which can be applied by the equation for hemisphere equation:

$$I_{lim} = 2\pi nFDcr \tag{2.1}$$

where n is the number of electrons involved in the redox reaction, F is the Faraday constant (96485 C/mol), D is the diffusion coefficient (cm^2/s), r is the radius of the nanoelectrode, and c is the concentration of redox species (mol/cm^3) in bulk solution.

DC CV measurement of redox species surface functionalized with substrate peptides

The surface functionalized VACNF NEAs was tested with CV in 1.0 M KCl solution. The potential of WE was ramped from -0.05 to +0.65 V at different scan rates, and the data was plotted in Figure 2.5B. The peak current was proportional to the scan rate, revealing redox tag was immobilized on the electrode surface.

ACV measurements

ACV experiments were carried out in 1.0 M KCl solution before and after surface functionalization. The DC current was ramped from -0.05 to +0.65 V at a scan rate of 5 mV/s, the amplitude of AC current was 150 mV, the AC frequency was 1000 Hz. Figure 2.5C shows the ACV data of VACNF NEAs before and after functionalization. Fc was oxidized at 0.25 V and the background current was decreased after passivation.

2.4 VACNF NEAs Passivation and Functionalization toward Protease Detection

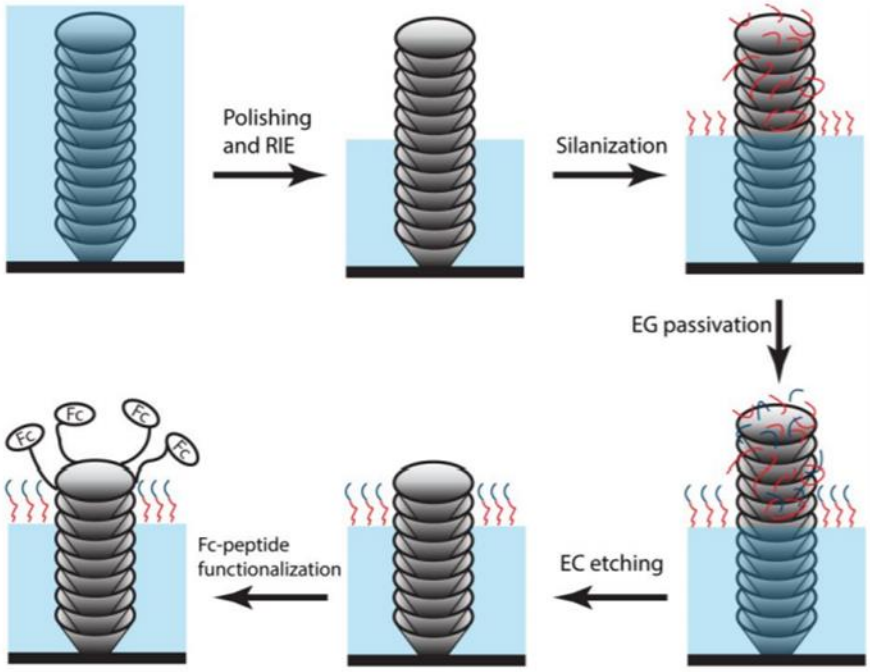

Figure 2.6 The passivation and functionalization procedure of the VACNF NEA chip. Copyright (2019) American Chemical Society.

The activated VACNF NEAs was passivated with (3-aminopropyl)triethoxysilane (APTES) and 2-(2-methoxyethoxy)ethoxyacetic acid to reduce nonspecific adsorption on SiO_2 surface. The VACNF NEA chip was dipped in the 8 g/L APTES solution in ethanol for 20 min to generate an amine group terminated surface. The chip was then treated with 50 µL mixed solution of 0.1 mM of 2-(2-methoxyethoxy)ethoxyacetic acid, 50 g/L of EDC and 50 g/L of sulfo-NHS, and was incubated at room temperature for 2 h in an Arrayit incubation chamber. The carboxylic acid group from 2-(2-methoxyethoxy)ethoxyacetic acid formed an amide bond with the amine group on the chip surface and generated an ethylene glycol group on the top surface. The residuals formed on the VACNF tips during the passivation processes were removed by electrochemical

etching at 1.2 V (vs. Ag/AgCl (3 M KCl)) for 10 s in 1.0 M NaOH. Eventually, clean VACNF tips with abundant carboxylic acid groups were obtained, which were surrounded by the passivated SiO_2 surface.

The Fc-labeled peptides were covalently attached to the exposed CNF tips through a -$(CH_2)_4$-NH_2 linker by an amide bond. 1-Ethyl-3-(3-dimethylaminopropyl)carbodiimide hydrochloride (EDC) and sodium 1-hydroxy-2,5-dioxopyrrolidine-3-sulfonate (sulfo-NHS) were used as the coupling reagents. Firstly, Fc-labeled peptide was diluted into 20 mM mother stock solution. Then, 10 μL mother stock solution was mixed with 90 μL coupling reagent containing 2.0 g/L EDC and 2.0 g/L sulfo-NHS. Then, it was applied on the VACNF NEA chip and incubated in a sealed hybridization chamber at room temperature for 2 hrs.

2.5 Conclusion

The fabrication, passivation, and functionalization procedures of VACNF NEAs have been discussed. The PECVD grown CNF has a brush like a vertically aligned structure, which is mechanically supported by the filling SiO_2. RIE process can selectively etch away the SiO_2 and expose the tips of the VACNFs, which provides enough carboxylic groups for surface functionalization through an amide bond. The sigmoidal shape of the CV curve indicates the nanoscale size of the CNF electrode and the small diffusion layer compared with the separation between the adjacent fibers. By functionalizing the ferrocene-attached peptide, the VACNF NEAs can be used as an electrochemical biosensor with high sensitivity and low background signals.

Chapter 3 - Cancer-related Protease Activity Biosensor Based on AC Voltammetry Using VACNF NEAs

3.1 Introduction

Proteolysis, as one of the most important biological catalytic reactions has been attributed to a class of enzyme called proteases. Currently, there are more than 600 protease genes have been found in humans.[57] Proteases hydrolyze the peptide bond by attacking the carbonyl group of the peptide to degrade the protein. It regulates a diversity of cellular progresses such as gene expression, differentiation, and apoptosis.[58-59] However, according to recent studies, proteases also play key roles in many diseases, such as oncologic, inflammatory, and cardiovascular diseases. For example, over-expression and increased activity are involved in invasion metastasis, and angiogenesis in tumor growth and progression. Cathepsins and matrix metalloproteases (MMPs) can digest the extracellular matrix and enable the malignant cells to cross the basement membrane.[60]

As a member of the cathepsin family, cathepsin B is one of the most studied proteases, which hydrolyzes peptides and proteins in lysosome in an acidic environment. Typically, there are three subgroups in the cathepsin family (cysteine, aspartic, and serine cathepsins). Cathepsin B is a cysteine protease, functioning in protein hydrolysis, cell death, antigen presentation, and tissue homeostasis. According to recent studies, cathepsin B has been implicated in cancer progression to degrade the extracellular matrix. It is overexpressed in various cancers, including breast, colorectal, prostate, and gastric cancer. Therefore, developing a rapid, sensitive, and specific

method for detecting cathepsin B is critical for cancer diagnosis and therapeutic efficacy assessment.

In recent years, various technologies have been developed targeting proteases detection, including enzyme-linked immunosorbent assay (ELISA) and fluorescence method.[61-62] These methods need fluorescence labels and sophisticated instruments, which is not feasible for point of care (POC). Compared with traditional methods, electrochemical methods are rapid and straightforward, it is possible to build a portable system to analyze the protease activity, and it is also possible for the patients to do POC tests at home. Recently, electrochemical methods using the CV technique to detect redox-labeled peptides on the gold electrode has have been established to detect high activity proteases such as plasmin and thrombin.[63-64] However, quantitative analysis of protease, which has lower catalytic activity, is still challenging. To enhance the sensitivity of the electrochemical method, we apply AC voltammetry method on a nanoscale carbon electrode array.

It is well known that ultrasmall electrodes, such as microelectrode and nanoelectrode, have many advantages when employed in electrochemical applications. These benefits include enhanced mass transport, the dominance of radial diffusion, decreased deleterious effect of solution resistance and decreased charging currents.[65] Because of the reduced dimension, the radial diffusion becomes dominant and results in faster mass transport, which is less likely to limit the electron transfer process. In the meantime, the faster mass transport offers analytical measurement shorter response time of nanoelectrodes to diffusing species in solution. Due to the nanoscale size of the electrode, several electrodes can be packed on a given sensor device to form a nanoelectrode array, which provides a large number of interaction points between the device and matrix. Furthermore, the nanoelectrode array can be functionalized with different substrates, poised at

different potentials, or even applied with different electrochemical techniques to detect different targets of the same sample matrix.

The biggest challenge to utilize the above benefits of nanoelectrode on protease activity detection is their fabrication and handling. Methods producing single nanoelectrodes have been based on micropipette pulling, electrochemical or chemical etching followed by photoresist or Teflon deposition, using carbon nanotubes or nanofibers, and etched metal array electrodes.[66] Carbon based NEAs trigger more attention than metal array electrodes because it has a broader applicable potential window than metal electrodes. Also, it easier to functionalize biomolecules on the carbon electrode surface through a covalent bond. However, a reliable carbon NEAs requires a fabrication method capable of producing a uniform carbon nanotube/nanofiber with a well-defined shape and property. Also, electrochemical sensors also need high conductivity and low background nanoarrays. Currently, there are many methods to fabricate well-controlled NEAs using the chemical vapor deposition method. In 1999, Li et al. have manufactured a carbon NEAs of parallel carbon nanotubes on an aluminum substrate using pores in an anodic alumina film as a template.[67] After electrochemically depositing cobalt catalyst into the pores, acetylene was introduced in the growth chamber for 2 hrs while the temperature was controlled around 650 ℃. By using this method, all nanotubes are parallel to each other and vertically stand on the substrate. Such uniform carbon nanotube array could be used in various applications that have been demonstrated, including DNA hybridization,[68] glucose detection,[69] and neuronal recording, and stimulation.[70] Typically, to increase the carboxylic group density of carbon nanotubes, nitric acid, and sulfate acid treatment are required,[71] which also cause defects on the carbon nanotubes. Compared with carbon nanotubes, carbon nanofibers have a higher carboxylic group density on the surface, which provides more functionalization spot. Here we have demonstrated that an NEA

fabricated with vertically aligned carbon nanofibers (VACNFs) can serve as a unique electrochemical platform for enzymatic studies. This VACNFs have a unique conically stacked structure perpendicular to the substrate. SiO_2 was used to embed VACNF NEAs and then selectively etched by plasma to expose ~100 nm long CNF tips. The average spacing between the exposed VACNFs was around 1000 nm. Specific peptide substrates were functionalized at the CNF tips and subjected to the hydrolysis by protease. The large separation and the hemisphere VACNF tips eliminated the steric hindrance which encountered on a plane working electrode.

Instead of using CV, we applied ACV as the electrochemical technique. Hence, the redox tag ferrocene can be oxidized and reduced back and force by the AC voltage bias applied to the direct current. The fast electron transfer rate between the ferrocene label and the CNFs was guaranteed by the high conductive conical structure. Moreover, the VACNFs NEA can sustain a much higher frequency compared with other plane macro electrode. Because the magnitude of the signal is proportional to the frequency, the sensitivity of the VACNFs NEA sensor can be significantly enhanced. Here we report the study on the quantitative analysis of cathepsin B activity using a peptide-functionalized nanoelectrode array (NEA), which can be potentially developed into multiplex electronic chips for rapidly profiling the activity of many proteases simultaneously.

3.2 Design and characterization of VACNF NEAs for protease detection

As reported previously, the VACNFs grown by PECVD consist of conical graphitic cups stacked along the fiber axis. This generates abundant –COOH groups at graphitic edges along the VACNF sidewall in the exposed tips. The Fc-labeled peptide substrate H_2N-$(CH_2)_4$CO-peptide-NH-CH_2-Fc can be covalently linked to the exposed CNF tip through the amide bond formed between the amine group in the linker H_2N-$(CH_2)_4$CO- and –COOH group at the VACNF tip. The

Fc label provides a reversible oxidation peak at ~0.25 V versus Ag/AgCl (3.0 M KCl) in ACV. After adding the specific target protease into the electrochemical cell, the enzyme recognizes its cognate peptide sequence and cleaves it at the particular sites. The Fc-containing fragments are released from the VACNF tip and causing the ACV signal to decrease over time. Higher protease activity induces a faster decrease in the Fc signal. For non-cognate proteases, the enzyme-peptide interaction is much weaker, resulting in a lower proteolysis rate. Thus, measuring the proteolysis kinetics of specific peptide probes allows quantitative estimation of the activity of its cognate proteases.

As shown in Figure 3.1, the electrochemical proteolytic curves pass through the same starting point (t = 0, i_p/i_{p0}=1) to normalize the signal. The observed signal was quite stable, indicating a negligible variation of the Fc amount attaching to the CNF tips through the peptide. At t = 0, the 5 mM dithiothreitol (DTT) buffer activated cathepsin B (R&D Systems Inc. Minneapolis, MN) was added into the electrochemical cell. As the enzyme cleaves the peptide, more Fc moieties are dissociated from the CNF tips. Consequently, the curve shows an exponential decay which can be fitted with the following equation (black line):

$$\frac{i_p}{i_{p0}} = exp\left(-{}^{t}/_{\tau}\right) + (bt + c)\,, \tag{3.1}$$

where the exponential term (with a time constant τ) associates with the proteolysis reaction, and the linear term (bt + c) account for the slow background drift. Because of the steric hindrance, not all Fc-labeled peptides can be cleaved by the protease as reflected by a small nonzero value (~ 0.3) at the end of the proteolysis (t = ~ 50 min). The protruding VACNF tips in this study substantially reduce the steric hindrance comparing to the common planar electrodes, but some Fc residues remain adsorbed on the surface.

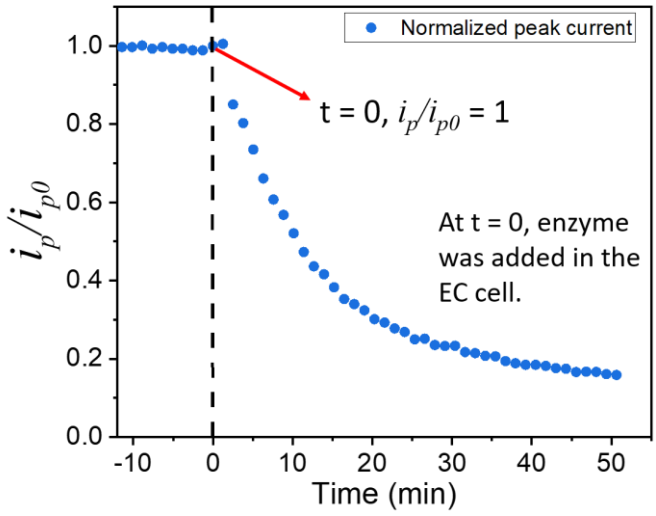

Figure 3.1 Normalized electrochemical proteolytic curve. The enzyme was added at t = 0.

Passivation procedure

In order to reduce nonspecific adsorption, the SiO_2 surface needs to be passivated with protective moieties containing ethylene glycol. The VACNF NEA chip was dipped in the 8 g/L APTES solution in ethanol for 20 min to generate an amine group terminated surface. The chip was then treated with 50 µL mixed solution of 0.1 mM of 2-(2-methoxyethoxy)ethoxyacetic acid, 50 g/L of EDC and 50 g/L of sulfo-NHS, and was incubated at room temperature for 2 hrs in an Arrayit incubation chamber. The carboxylic acid group from 2-(2-methoxyethoxy)ethoxyacetic acid formed an amide bond with the amine group on the chip surface and generated an ethylene glycol group on the top surface. The residuals created on the VACNF tips during the passivation processes were removed by electrochemical etching at 1.2 V (vs. Ag/AgCl (3 M KCl)) for 10 s in 1.0 M NaOH. Eventually, clean VACNF tips with large carboxylic acid groups were obtained, surrounded by the passivated SiO_2 surface.

Figure 3.2A shows the electrochemical characterization of a VACNF NEA chip at each of the above steps using 1.0 mM $K_4Fe(CN)_6$ with 1.0 M KCl and an Ag/AgCl (3 M KCl) reference electrode. After passivation, the peak separation increased to over 300 mV and the peak current decreased, both due to passivation to the VACNF tips besides the SiO_2 surface. After electrochemical etching in 1.0 M NaOH at 1.2 V for 10 s, the peak separation decreased to 150 mV. Figure 3.2B shows the method to extract the background current and calculate the capacitance (with $\Delta i = 2C\nu$). The derived specific capacitance (C_0) of the VACNF NEA was 45.6 μF/cm2. Considering that the effective surface area of the embedded VACNF array is over ten times the geometric surface area, the ions (particularly Na^+ ions) may penetrate through the SiO_2 coating and access to about one-tenth of the VACNF surface. A large portion of this leaking current is due to the voids (as shown in Figure 2.3C) in the gap-filled SiO_2 between the high-density brush-like VACNFs. In the future, the uniform SiO_2 coating on the well-separated regular VACNF NEAs fabricated with nanolithography will substantially reduce the background current and significantly enhance the sensor performance.

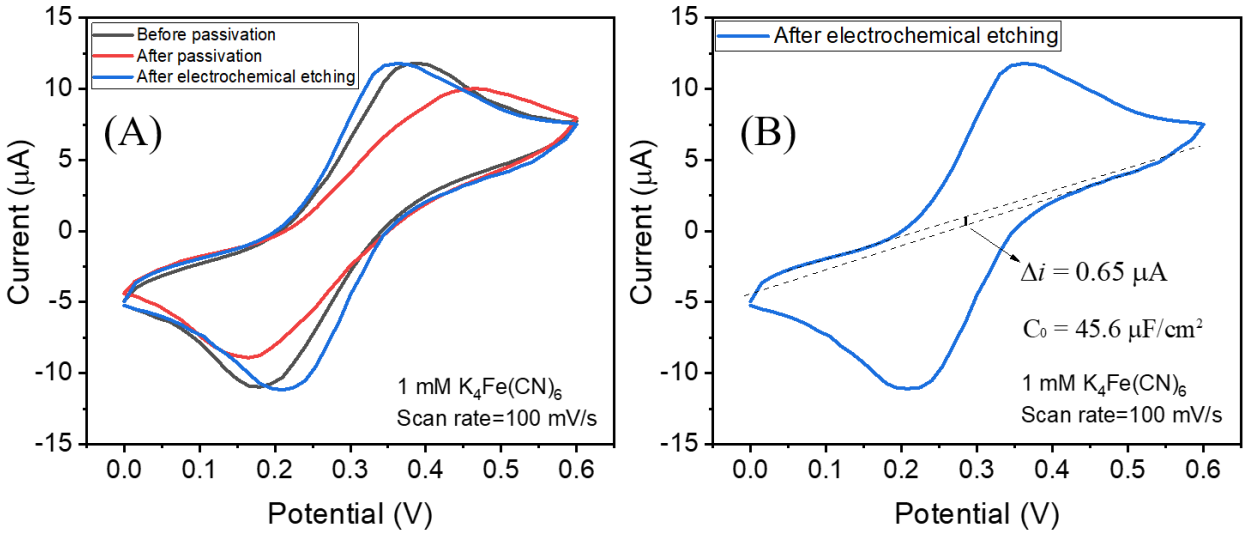

Figure 3.2 (A) Electrochemical characterization of VACNF NEA chip using cyclic voltammetry in benchmark redox solution of 1.0 mM $K_4Fe(CN)_6$ in 1.0 M KCl at the scan rate of 100 mV/s.

The reference electrode was Ag/AgCl (3.0 M KCl). (B) The specific capacitance of the VACNF NEA chip after electrochemical etching was extracted to be 45.6 mF/cm^2. Copyright (2019) American Chemical Society.

Peptide substrates for fluorescence and electrochemical methods

Two commercial fluorescence substrates (Z-Leu-Arg-AMC and Mca-Lys-Pro-Leu-Gly-Leu-Dpa-Ala_Arg-NH_2) were acquired from R&D Systems Inc. (Minneapolis, MN, USA). Z-Leu-Arg-AMC was designed for cathepsin B ((Z is N-carbobenzyloxy, AMC is 7-amino-4-methylcoumarin). Mca-Lys-Pro-Leu-Gly-Leu-Dpa-Ala_Arg-NH_2 was designed for ADAM10 and ADAM17, where Mca is (7-methoxycoumarin-4-yl)acetyl and Dpa is N-3-(2, 4-dinitrophenyl)-L-2,3-diaminopropiony. Over twenty Fc labeled peptides for electrochemical methods were synthesized by Dr. Huafang Fan in Duy H. Hua's laboratory at Kansas State University. The analyses of the cleavage sites of the substrate peptides using LC-MS were carried out by Dr. Huafang Fan. The synthetic procedure and characterization of peptide sequences are described in Appendix A. Representative synthesized peptides 3-6 and two commercially available fluorescence peptide 1 and FRET peptide 2 for cathepsin B and ADAM17 are summarized in Table 3.1.

Table 3.1 Peptide substrate sequences and cognate proteases. (Peptide substrates were designed by Dr. Duy H. Hua and synthesized by Dr. Huafang Fan.) Copyright (2019) American Chemical Society.

Peptide #	Peptide substrate sequences	Protease	Detection method
1	Z-Leu-Arg-AMC	Cathepsin B	Fluorescence
2	Mca-Lys-Pro-Leu-Gly-Leu-Dpa-Ala-Arg–NH_2	ADAM10 ADAM17	Fluorescence
3	A-Leu-Arg-Phe-Gly-B[a]	Cathepsin B	Electrochemical
4	A-Pro-Leu-Arg-Phe-Gly-Ala-B	Cathepsin B	Electrochemical
5	A-Ala-Pro-Leu-Arg-Phe-Gly-Ala-Ala-B	Cathepsin B	Electrochemical
6	A-Lys-Pro-Leu-Gly-Leu-Ser-Ala-Arg-B	ADAM17	Electrochemical

[a]A, linker $H_2N(CH_2)_4CO$– at the N-terminus; B, redox tag –$NHCH_2Fc$ at the C-terminus.

Functionalization procedure

The Fc-labeled peptides were covalently attached to the exposed CNF tips through a -$(CH_2)_4$-NH_2 linker by an amide bond. 1-ethyl-3-(3-dimethylaminopropyl)carbodiimide hydrochloride (EDC) and sodium 1-hydroxy-2,5-dioxopyrrolidine-3-sulfonate (sulfo-NHS) were used as the coupling reagents. Firstly, Fc-labeled peptide was diluted into 20 mM mother stock solution. Then, 10 μL mother stock solution was mixed with 90 μL coupling reagent containing 2.0 g/L EDC and 2.0 g/L sulfo-NHS and then applied on the VACNF NEA chip and incubated in a sealed chamber (Arrayit, Sunnyvale, CA) at room temperature for 2 hrs.

3.3 Validation of enzyme activity with fluorescence and HPLC methods

Different concentrations of AMC were measured to calibrate the fluorescence intensity versus AMC concentration using a GloMax Multi+ Microplate Reader (Promega, Madison, WI, USA) in 96-well plates. As shown in Figure 3.3, the concentration of AMC and fluorescence

intensity shows a linear relationship between 6.9 μM to 139 μM. Above 139 μM, the slope of the curve starts to decrease and then reaches a plateau around 1,256 μM. Figure 3.4A shows the fluorescence intensity versus reaction time at four different substrate concentrations (100 μM, 50 μM, 25 μM, and 12.5 μM) but with the same cathepsin B concentration (3.4 nM). Figure 3.4B shows the produced AMC concentration converted using the calibration curve in Figure 3.3B, which clarifies the change of reaction product versus reaction time.

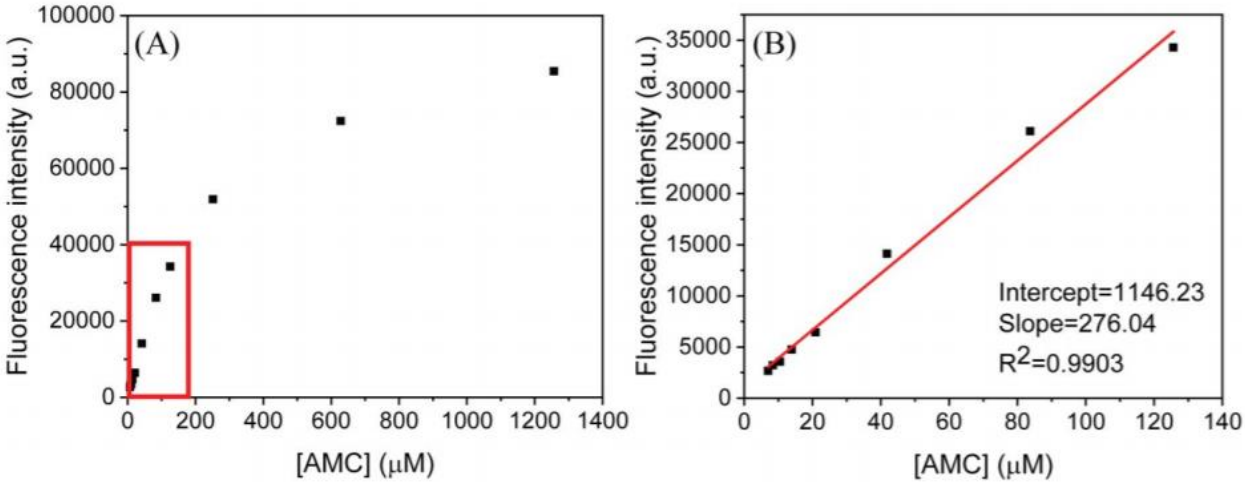

Figure 3.3 Calibration curves of the fluorescence emission of free AMC dye using Promega GloMax Multi+ Microplate Multimode Reader with the excitation and emission wavelength of 365 and 460 nm, respectively. (A) Plot of AMC concentration (in μM) versus fluorescence intensity (a.u.) from 6.9 μM to 1,256 μM. (B) A linear fitting of the fluorescence intensity (a.u.) in a narrower range of the free AMC concentration from 6.9 μM to 139 μM Calibration curve of the fluorescence emission of free AMC dye using Promega GloMax Multi+ Microplate Multimode Reader with the excitation and emission wavelength of 365 and 460 nm, respectively. (A) Plot of AMC concentration (in μM) versus fluorescence intensity (a.u.) from 6.9 μM to 1,256 μM. (B) A linear fitting of the fluorescence intensity (a.u.) in a narrower range of the free AMC concentration from 6.9 μM to 139 μM. Copyright (2019) American Chemical Society.

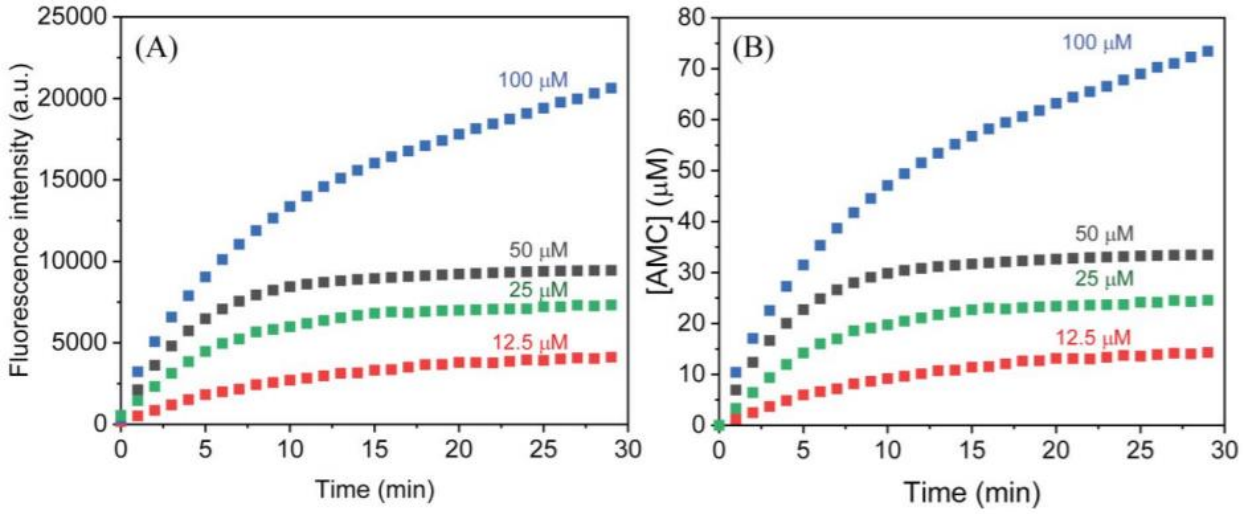

Figure 3.4 (A) The kinetic proteolytic curve is represented by fluorescence intensity (a.u.) versus the reaction time using 12.5, 25, 50, and 100 μM cathepsin B substrate (Z-L-R-AMC) concentration. The concentration of the activated cathepsin B is 3.45 nM. The excitation and emission wavelengths were 365 and 460 nm, respectively. (B) The kinetic proteolytic curve converted into produced free AMC concentration versus the reaction time (converted using the linear calibration curve in Figure 3.3B). Copyright (2019) American Chemical Society.

ADAM10 and ADAM17 use the same FRET substrate Mca-KPLGL-Dpa-AR-NH_2. The excitation wavelength of the fluorophore 7-methoxycoumarin-4-acetic acid (Mca) is 290 nm and the emission wavelength is 405 nm, beyond the light source and filter range of GloMax Multi+ reader. Thus a StellarNet fluorescence spectrophotometer (Tampa, FL, USA) was used for these measurements. The cathepsin B proteolysis was repeated with this instrument for direct comparison. Figure 3.5 shows the measured fluorescence emission spectra at different reaction time during cathepsin B proteolysis of substrate Z-L-R-AMC (Figure 3.5A), ADAM10 (Figure 3.5B), and ADAM17 (Figure 3.5C) proteolysis of the commercial FRET substrate Mca-

KPLGLDpa-AR-NH_2. The curves labeled blank are the spectra before adding the proteases. All experiments were carried out at room temperature.

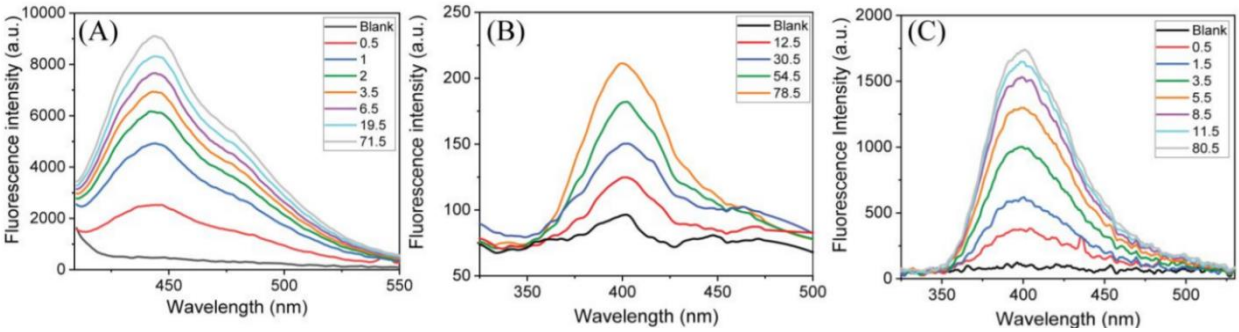

Figure 3.5 (A) The fluorescence emission spectra collected at different proteolytic time (in unit of min) by 35.4 nM cathepsin B on 20.6 μM FRET substrate (Z-L-AMC). The excitation light is from a 390 nm LED. (B) and (C) Similar fluorescence emission spectra collected at different proteolytic time (in unit of min) by 34.5 nM of ADAM10 and 35.4 nM ADAM17, respectively, on the same 20.6 μM fluorescence substrate (Mca-K-P-L-G-L-Dpa-A-R-NH_2). The excitation light is from a 290 nm LED. All experiments were carried out at room temperature with a StellarNet fluorescence spectrophotometer. Copyright (2019) American Chemical Society.

Figure 3.6 summarizes the kinetic proteolysis processes shown in Figure 3.5. The fluorescence emission intensity at 405 nm from Mca is plot versus the reaction time for ADAM10 and ADAM17, while the fluorescence emission intensity at 460 nm from AMC is used for cathepsin B. In all experiments, the protease concentration was controlled at 35.4 nM, and the FRET substrate concentration at 20.6 μM. The experiments were carried out at room temperature. Clearly, cathepsin B generated a much higher fluorescence signal than ADAM17 and ADAM10. However, since these experiments use different fluorophores, light sources, and filters, the quantum yields are very different. Thus it is not practical to directly compare the fluorescence intensity. Notably, the proteolytic activity of cathepsin B is higher than that of ADAM17. To overcome this problem, each set of the raw kinetic proteolytic curve is normalized relative to its maximum fluorescence intensity. As shown in Figure 3.6B, it is now much easier to compare the relative kinetic changes. Apparently, cathepsin B and ADAM17 show very close activity as reflected in the fast rise of the proteolysis curve. In contrast, ADAM10's activity is much lower using the same commercial FRET substrate Mca-KPLGL-Dpa-AR-NH_2 for ADAM17.

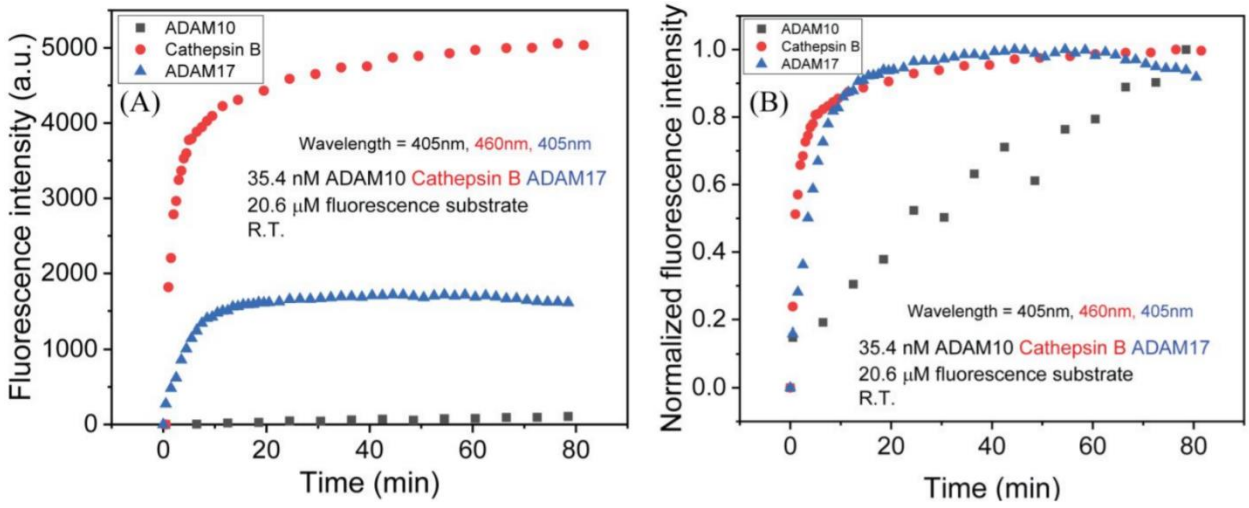

Figure 3.6 Comparison of kinetic proteolytic curves by 35.4 nM of ADAM10, ADAM17 and cathepsin B, respectively, on 20.6 μM corresponding FRET substrates, with the fluorescence intensity corresponding to the peak emission in Figure 3.5 at the wavelength of 405 nm for Mca

(from the proteolyzed ADAM10 and ADAM17 substrate) and 460 nm for AMC (from the proteolyzed cathepsin B substrate), respectively. All experiments were carried out at room temperature. Panel (A) is the raw data, and panel (B) is the normalized data relative to each curve's maximum fluorescence intensity. Copyright (2019) American Chemical Society.

3.4 Michaelis-Menten model for kinetic proteolysis reaction

As derived in our previous studies, the exponential kinetic proteolysis can be described by a Michaelis-Menten model for the heterogeneous enzymatic reaction:

$$E + S_s \underset{k_{-1}}{\overset{k_1}{\leftrightarrow}} ES_s \overset{k_{cat}}{\Longrightarrow} E + P_s + P\,, \tag{3.2}$$

where E is the enzyme, S_s is the Fc-labeled peptide substrate attached on VACNF tips, ES_s is the enzyme-substrate complex on CNF tips, P_s is the surface attached product, and P is the released product containing Fc. The steady-state reaction rate can be defined as:

$$\upsilon = -\frac{d\Gamma_{Ss}}{dt} = \frac{k_{cat}[E_0]\times\Gamma_{Ss}}{K_M+[E_0]}\,, \tag{3.3}$$

where Γ_{Ss} is the amount of Fc-labeled peptide substrate on the VACNF tips, k_{cat} is the catalytic dissociation rate constant and $K_M = (k_{cat}+k_{-1})/k_1$ is the Michaelis-Menten constant. For the system after subtracting the linear background term in Equation (1), one has $\Gamma_{Ss} \propto i_p/i_{p0}$. The following relationship can be derived at low $[E_0]$ (with $[E_0] << K_M$):

$$-\frac{d(\frac{i_p}{i_{p0}})}{dt} = \frac{k_{cat}[E_0]\times(\frac{i_p}{i_{p0}})}{K_M+[E_0]} \approx \frac{k_{cat}[E_0]\times(\frac{i_p}{i_{p0}})}{K_M}. \tag{3.4}$$

Rearranging Equation (3.4) gives

$$-\frac{\frac{d\left(\frac{i_p}{i_{p0}}\right)}{dt}}{\left(\frac{i_p}{i_{p0}}\right)} = \frac{k_{cat}}{K_M}[E_0]. \quad (3.5)$$

Integrating Equation (3.5) leads to the exponential function which links to the exponential term in equation (3.1):

$$\frac{i_p}{i_{p0}} = \exp\left(-\frac{k_{cat}}{K_M}[E_0]t\right) = \exp(-t/\tau). \quad (3.6)$$

This indicates the relationship between experimentally observed quantity τ and the fundamental properties of the protease by,

$$\frac{1}{\tau} = (\frac{k_{cat}}{K_M})[E_0], \quad (3.7)$$

where (k_{cat}/K_M) is the "specificity constant" representing the intrinsic catalytic efficiency of a protease to a specific peptide substrate. Clearly, the activity represented by 1/τ is not only proportional to the concentration of the protease [E_0], but also proportional to the "specificity constant". It is the overall value of (k_{cat}/K_M)[E_0] rather than [E_0] alone that defines the decay rate (i.e. the proteolysis rate). The affinity techniques to detect [E_0] (such as ELISA) only reveal information of [E_0] but not (k_{cat}/K_M)[E_0]. In this study, we focus on enhancing the (k_{cat}/K_M) value of the target protease over other non-target proteases using optimized peptide substrates so that a higher selectivity can be obtained.

3.5 Analysis of cathepsin B activity

In principle, longer peptides may provide higher binding with the protease and thus give higher (k_{cat}/K_M) value. However, longer peptide may give lower electron transfer rate due to larger distance between Fc and the VACNF tip. To assess these effects, we have designed a tetrapeptide

substrate, a hexapeptide substrate and an octapeptide substrate by adding extra amino acids at the two ends of the tetrapeptide (Table 3.1). In addition, the proteolysis process requires the peptide substrates to access the protease domain, and it has been proposed that the structure of the protease domain changed at different temperatures.[72] Thus, the k_{cat}/K_M value and the proteolysis rate may be significantly altered by the temperature, leading to varied proteolysis rates at the same protease concentration. Here, proteolysis was measured with ACV using VACNF NEAs at four different temperatures, i.e., 19.3, 29.5, 38.6, and 44.2 °C. The measurement conditions (400 Hz, 100 mV amplitude, and 30.7 nM cathepsin B) are same.

3.5.1 Peptide substrates with different length: tetrapeptide, hexapeptide, and octapeptide

Figure 3.7A shows the dependence of the peak current on the applied frequency in ACV for the tetrapeptide, hexapeptide, and octapeptide, respectively. The peak current is normalized to the maximum value ($i_{p,max}$) of each peptide substrate for easier comparison. Clearly, each peptide shows a maximal i_p at a specific frequency which shifts to a lower value as the peptide length increases, being ~600 Hz for the tetrapeptide, ~400 Hz for the hexapeptide, and ~200 Hz for the octapeptide. This is consistent with a decrease in the electron transfer rate as the average distance between Fc and VACNF tip increases with the peptide length. Such frequency dependence is good evidence that peptide molecules likely stand up rather than lying flatly on the surface of the VACNF tips, which is beneficial in reducing the steric hindrance on the surface. From an electrochemical detection point of view, higher AC frequency is desired to achieve higher detection speed and higher sensitivity.

The AC voltage amplitude is another factor that affects the ACV measurements. In Figure 3.7B, tetrapeptide, hexapeptide, and octapeptide show similar trends in the normalized i_p versus the AC voltage amplitude. The peak current linearly increases with the amplitude from 25 to 100 mV. When the voltage amplitude goes above 100 mV, the peak current slowly drops. Thus the optimal amplitude is between 100 mV and 150 mV, notably higher than the small amplitude (< 25 mV) used in ACV on planar electrodes. The high AC voltage would induce dielectrophoresis to concentrate biomolecules near the electrode surface due to the large electric field gradient. This is a unique advantage of the VACNF NEA demonstrated in our previous study of AC dielectrophoretic capture of bacteria and virus particles. In this study, concentrating protease molecules near the VACNF tips would further enhance the proteolysis rate and increase the detection sensitivity.

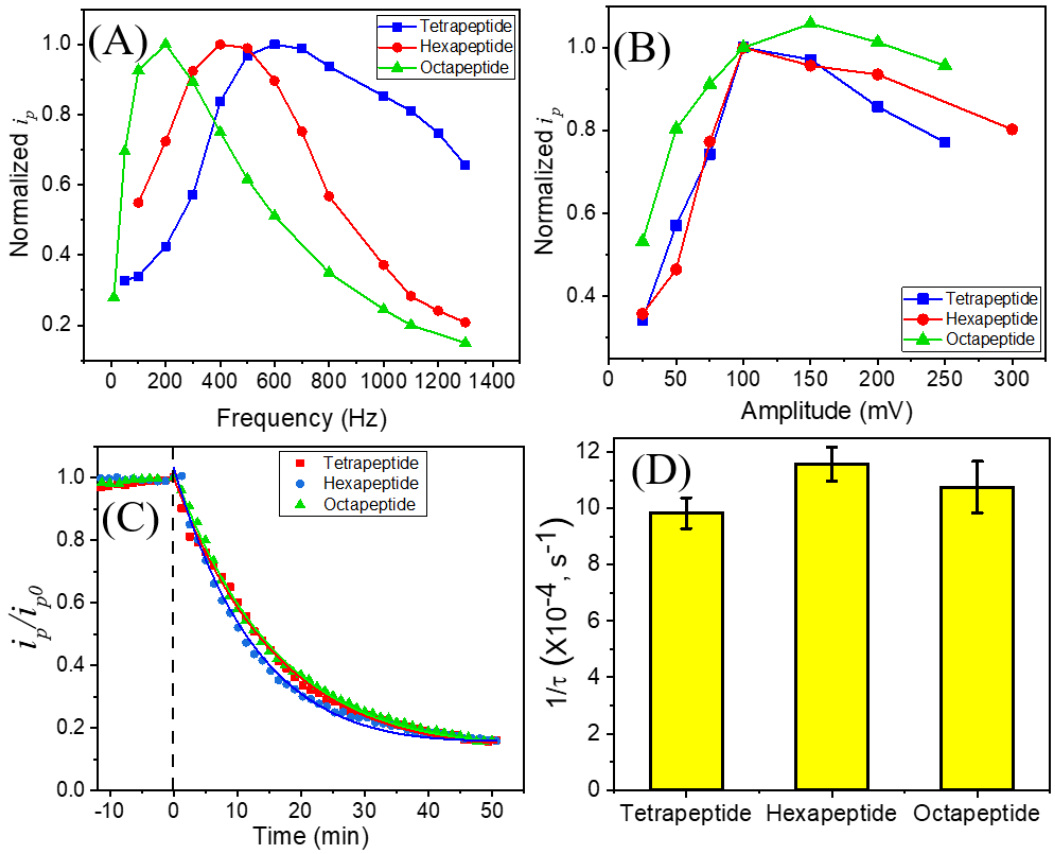

Figure 3.7 (A) Normalized peak current of the peptide-Fc functionalized VACNF NEA in AC voltammetry at different frequencies for tetrapeptide, hexapeptide and octapeptide, respectively. (B) Normalized peak current of peptide-Fc functionalized VACNF NEA in AC voltammetry at different voltage amplitudes for tetrapeptide, hexapeptide and octapeptide, respectively. The electrochemically measured kinetic proteolytic curves of the three peptide substrates by 30.7 nM cathepsin B at room temperature (~26 °C). (D) Bar chart plot of 1/t versus different peptides. The error bars represent the standard deviation from three replicates (n=3). Copyright (2019) American Chemical Society.

Figure 3.7C shows the kinetic proteolysis curves, in the form of i_p/i_{p0} versus time, for the three peptides with 30.7 nM activated cathepsin B at room temperature. All measurements were

done by continuously repeated ACV at 400 Hz and 100 mV amplitude. The fitted time constant τ is 1059, 846, and 1030 s for the tetrapeptide, hexapeptide, and octapeptide. The hexapeptide gives the fastest kinetic decay and smallest τ value. Figure 3.7D summarizes these results in the form of a bar chart. The average $1/\tau$ values from the three replicates are 9.8×10^{-4}, 11.6×10^{-4}, and 10.7×10^{-4} s^{-1}, respectively, representing the activity of cathepsin B on each peptide substrate. Even though the concentration of cathepsin B is the same (30.7 nM), peptide substrates interact differently with cathepsin B and give different k_{cat}/K_M values, leading to varied activities. The central tetrapeptide sequence seems to play a significant role in defining the peptide-protease interaction and longer peptides only induce small modulations. Overall, the hexapeptide produced the highest proteolysis rate which balances the protease-peptide binding and electron transfer rate.

3.5.2 Cathepsin B proteolysis rate at different temperature

As shown in Figure 3.8A, the curve decays fastest at 38.6 °C and slowed down when the temperature was off to either side, with τ = 1447 s at 19.3 °C, τ = 1038 s at 29.5 °C, τ = 274 s at 38.6 °C, and τ = 552 s at 44.2 °C. The measured activity (i.e. $1/\tau$) in Figure 3.8B slowly increased from 7.6×10^{-4} s^{-1} at 19.3 °C to 10.6×10^{-4} s^{-1} at 29.5 °C, reached the maximum of 36.3×10^{-4} s^{-1} at 38.6 °C, and then dropped to 15.4×10^{-4} s^{-1} at 44.2 °C. This reflects a dramatic effect on the activity, about 5 times at 38.6 °C compared to that near room temperature (19.3 °C). It is not surprising that the proteolysis activity is the highest near body temperature (~37 °C), the natural physiology condition.

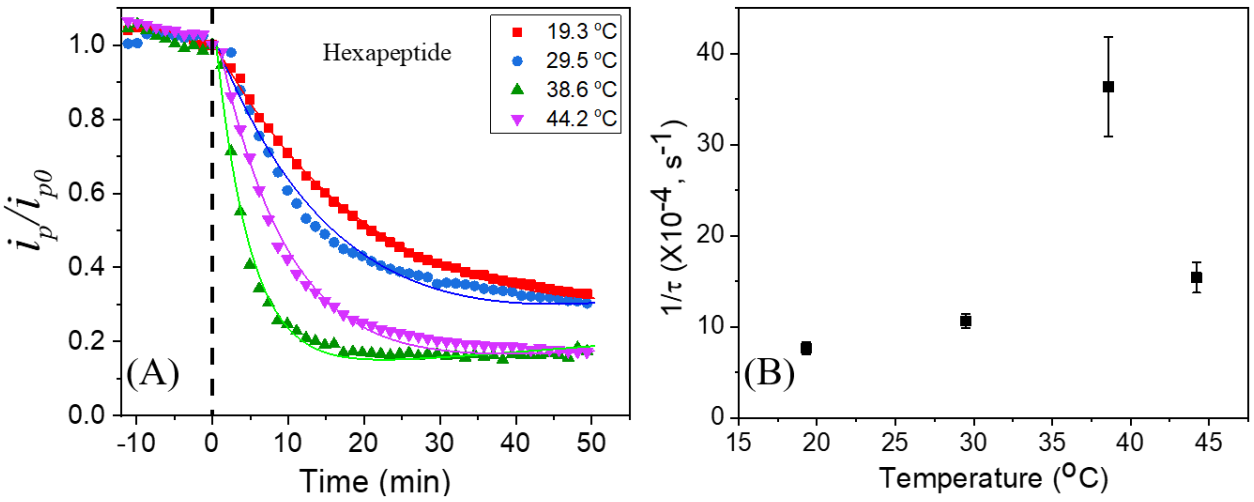

Figure 3.8 (A) The kinetic proteolysis curve by 30.7 nM cathepsin B at four different temperatures with AC voltammetry on the hexapeptide-Fc modified VACNF NEA. (B) Scattered plot of 1/τ (× 10^{-4} s^{-1}) versus the measuring temperature. The error bars represent the standard deviation from three replicates (n=3). Copyright (2019) American Chemical Society.

3.5.3 Assessment of the limit of detection in measuring cathepsin B

A series of proteolysis measurements have been carried out at different cathepsin B concentrations using VACNF NEA chips functionalized with the Fc-labeled hexapeptide (peptide #4) to assess the limit of detection (LOD) for cathepsin B activity and concentration. All measurements are at the optimized ACV conditions (400 Hz and 100 mV amplitude) and the optimal temperature (38.6 °C) based on the above studies. As shown in Figure 3.9A, the proteolytic curve decays faster as the enzyme concentration is increased. The fitted τ values at 0.50, 1.0, 2.56, and 10.2 nM cathepsin B are 3305, 1976, 1277, and 326 s, respectively. Figure 3.9B shows the bar chart of 1/τ at six protease concentrations. The 1/τ values, i.e. the activity, are 1.87 × 10^{-4}, 3.02 × 10^{-4}, 5.24 × 10^{-4}, 6.56 × 10^{-4}, 12.30 × 10^{-4}, and 27.66 × 10^{-4} s^{-1} for the blank, 0.50, 1.0, 2.56, 6.0, and 10.2 nM cathepsin B, respectively. The error bars are the standard deviation of three replicates

for each measurement. The LOD of activity (i.e. 1/τ) can be determined as 2.49 x 10^{-4} s^{-1} (represented by the dashed line in Figure 3.9B) by

$$LOD\ of\ activity = 3\sigma_{blank} + (1/\tau)_{blank}, \quad (3.8)$$

where σ_{blank} = 2.06 x 10^{-5} s^{-1} is the standard deviation and $(1/\tau)_{blank}$ = 1.87 × 10^{-4} s^{-1} is the mean value of blank experiments. This involves adding blank activity buffer into electrochemical cell filled with the assay buffer. Thus it causes some disturbance to the electrochemical signal and causes the i_p/i_{p0} value to decrease slowly. However, it is clear in Figure 3.9B that even adding 0.50 nM cathepsin B gives an activity (i.e. 1/τ value from fitting the proteolytic curve) above the blank buffer. This illustrates the necessity to measure the whole kinetic proteolytic curve rather than measure the single-point signal at the end of a fixed proteolysis time, as done in many studies.

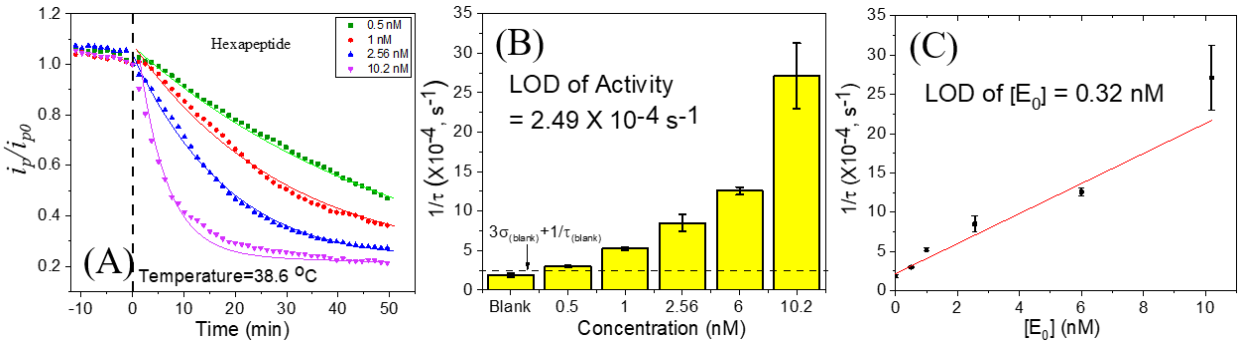

Figure 3.9 (A) The kinetic proteolysis profiles measured at cathepsin B concentration of 0.50, 1.0, 2.56 and 10.2 nM, respectively. (B) Bar plot of 1/ τ versus cathepsin B concentrations. The error bars are one standard deviation obtained with three replicates. (C) The linear calibration curve of the protease activity represented by 1/τ versus the cathepsin B concentration from 0.5 nM to 10.2 nM. Copyright (2019) American Chemical Society.

The LOD of cathepsin B concentration can also be accurately derived from the calibration curve. Figure 3.9C shows the best linear fit to the data of $1/\tau$ versus the enzyme concentration $[E_0]$. A total of six enzyme concentrations (including the blank) are included. Instrument fitting was used to get the best fitting line. The LOD of the cathepsin B concentration $[E_0]$ can be calculated as 0.32 nM by

$$LOD\ of\ [E_0] = {}^{3\sigma_{blank}}/_{m}, \tag{3.9}$$

where $m = 1.9 \times 10^5\ M^{-1}s^{-1}$ is the slope of the fitting line.

Since $1/\tau = (k_{cat}/K_M)[E_0]$, the slope of the fitting line in Figure 3.9C represents the specificity constant (k_{cat}/K_M) of cathepsin B, which is $1.9 \times 10^5\ M^{-1}s^{-1}$ in this study, about 4.6 times of the value $(4.11 \pm 0.67) \times 10^4\ M^{-1}s^{-1}$ in our previous reports. As described above, the larger specificity constant gives a higher catalytic efficiency. Raising the temperature from room temperature (~20 °C) to 38.6 °C effectively enhances the specificity constant, leading to a higher sensitivity and a lower LOD.

3.5.4 Selectivity of the hexapeptide substrate

As shown from the above results, the hexapeptide (peptide #4) serves as a highly sensitive probe for detecting cathepsin B. The next question is whether it can be cleaved by other proteases due to cross-reactions. To assess this, we have tested it with two other cancer-related proteases, i.e., ADAM10 and ADAM17. Figures 3.5 and 3.6 are measurements with the fluorescence substrates to validate their activity. The activity of ADAM17 on its cognate peptide substrate, peptide #2, is comparable to cathepsin B on peptide #1, but that of ADAM10 is much lower.

Figure 3.10A shows that the kinetic curves of 6.0 nM ADAM10 and 6.0 nM ADAM17 are almost overlapped with that of the blank buffer. In contrast, the curve of 6.0 nM cathepsin B shows a fast decay, giving $1/\tau = 12 \times 10^{-4}$ s^{-1}, well above all other controls in Figure 3.10B. It is clear that peptide #4 has a very high selectivity for cathepsin B. Furthermore, as shown in Figures 3.10C and 3.10D, the VACNF NEAs functionalized with the cognate octapeptide (peptide #6) of ADAM17 present negligible cross-reactions with cathepsin B and ADAM10. Both 6.0 nM cathepsin B and 6.0 nM ADAM10 show very small $1/\tau$ values comparable to the blank buffer, while a large value $1/\tau = \sim 9 \times 10^{-4}$ s^{-1} is obtained in 6.0 nM ADAM17.

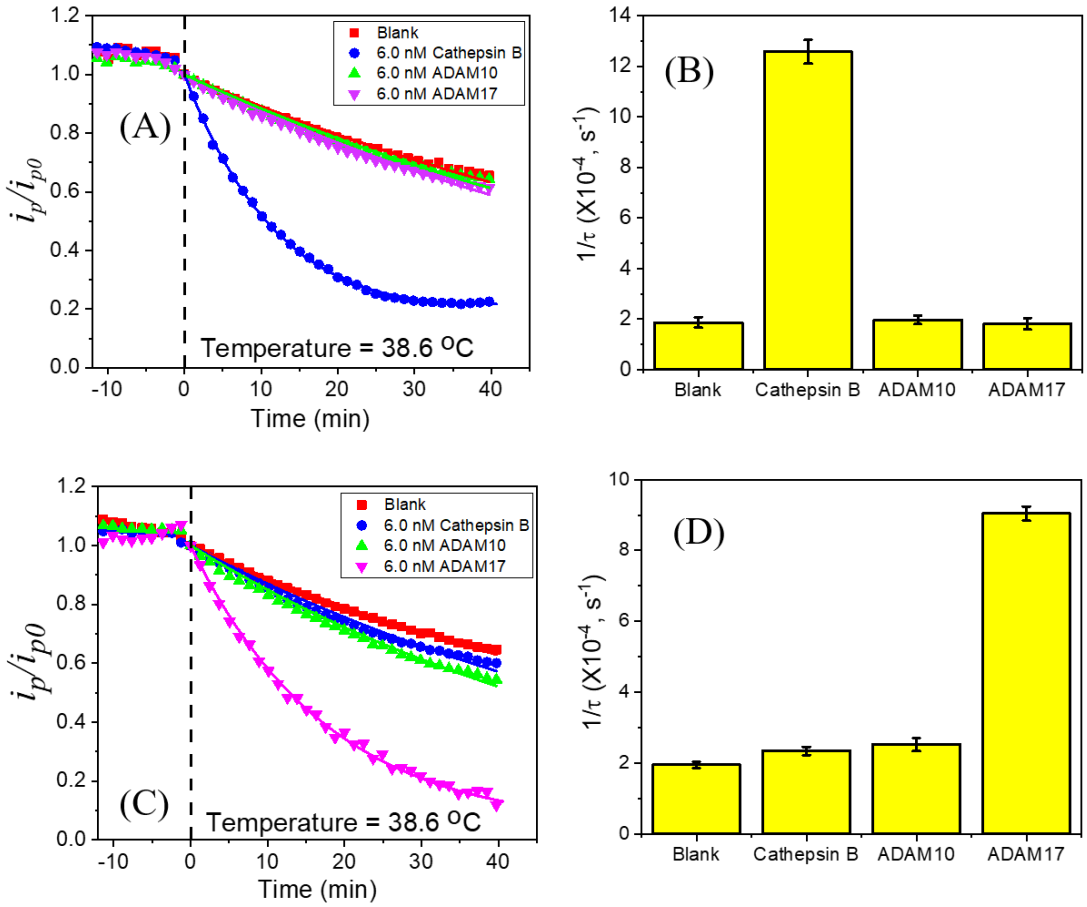

Figure 3.10 (A) Specificity test in 6.0 nM of cathepsin B, ADAM10, and ADAM17, respectively, versus the blank on hexapeptide (peptide #4) functionalized VACNF NEA and (B) bar plot of the corresponding $1/\tau$ values. (C) Specificity test in 6.0 nM of cathepsin B, ADAM10, and ADAM17,

respectively, versus the blank on octapeptide (peptide #6) functionalized VACNF NEA and (D) bar plot of the corresponding 1/τ values. The error bars in panels (B) and (D) represent the standard deviation from three replicates (n=3). Copyright (2019) American Chemical Society.

Figure 3.11A further shows the electrochemical proteolysis curves of hexapeptide (peptide #4) functionalized VACNF NEA in blank, 0.50 nM ADAM10, and 0.50 nM cathepsin B, respectively. The decay rate in 0.5 nM cathepsin B is clearly faster than the other two. The average value of 1/τ in 0.50 nM cathepsin B is 3.02×10^{-4} s^{-1}, larger than those in blank (1.87×10^{-4} s^{-1}) and 0.50 nM ADAM10 (2.16×10^{-4} s^{-1}) in Figure 3.11B. In addition, the 1/τ value of 0.50 nM ADAM10 is comparable with the blank, indicating negligible cross-reaction of ADAM10 with peptide #4 that was specifically designed for cathepsin B.

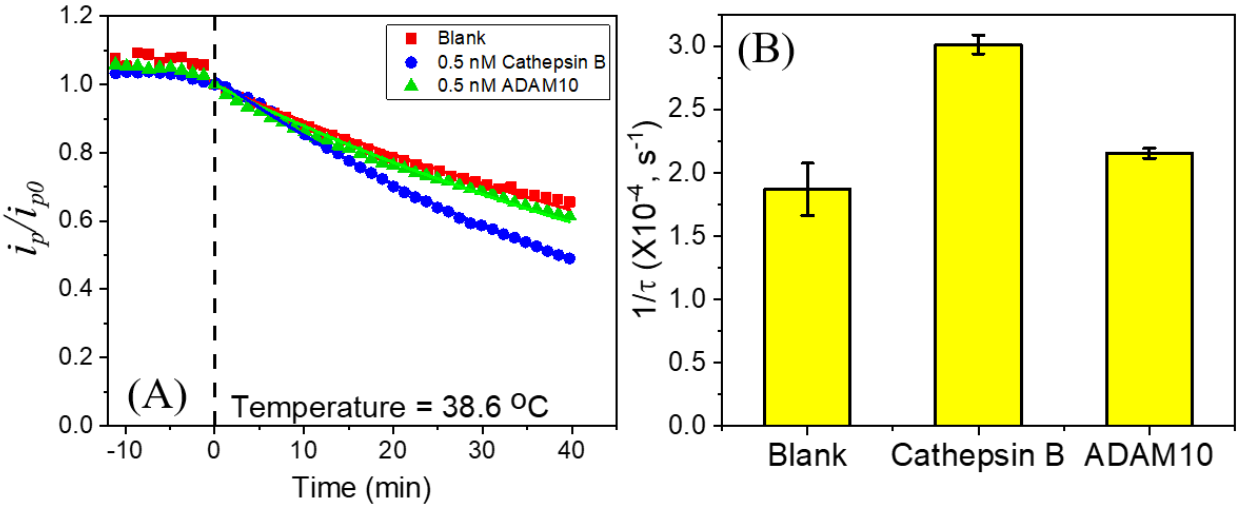

Figure 3.11 (A) The kinetic profile of the hexapeptide modified VACNF NEA in blank, 0.50 nM cathepsin B and 0.50 nM ADAM10. (B) Bar plot of 1/t in blank, 0.50 nM cathepsin B and 0.50 nM ADAM10. The error bars represent the standard deviation obtained from three replicates. Copyright (2019) American Chemical Society.

3.5.5 Cleavage site(s) of the hexapeptide by cathepsin B

According to our previous study, tetrapeptide (peptide #3) H_2N-$(CH_2)_4$-CO-Leu-Arg-Phe-Gly-NH-CH_2-Fc was cleaved by cathepsin B at the Arg-Phe site in the MES assay buffer (pH = 5.0).[73] To our surprise, the hexapeptide (peptide #4) H_2N-$(CH_2)_4$CO-Pro-Leu-Arg-Phe-Gly-Ala-NH-CH_2-Fc extended from the tetrapeptide was cleaved by cathepsin B at two different sites between Gly-Ala and Phe-Gly in MES buffer (see the HPLC results in Figure 3.12). We have synthesized Ala-NH-CH_2-Fc and Gly-Ala-NH-CH_2-Fc molecules independently and found that their HPLC retention times matched those of proteolyzed hexapeptide (peptide #4) by cathepsin B (see Figure 3.12). It is clear that the cleavage sites are different from that in tetrapeptide (peptide #3). Two possible changes in the hexapeptide may contribute to the observed cleavage sites: (1) Addition of Pro at the *C*-terminus and Ala at the *N*-terminus of peptide #3 to synthesize peptide #4 may change the binding conformation of hexapeptide with cathepsin B, leading to different cleavage sites, at the less sterically bulky amino acid residues Gly and Ala; (2) The Pro residue may provide a β-turn of the substrate peptide, resulting in different cleavage sites from that of peptide #3 (absence of Pro). Using Mobyle predictive computational calculation (RPBS Web portal)[74], the minimum energy conformation of peptide #4 adapted a turn structure (see Figure 3.13). In addition, cathepsin B is known to cleave peptides at Gly and Arg sites.

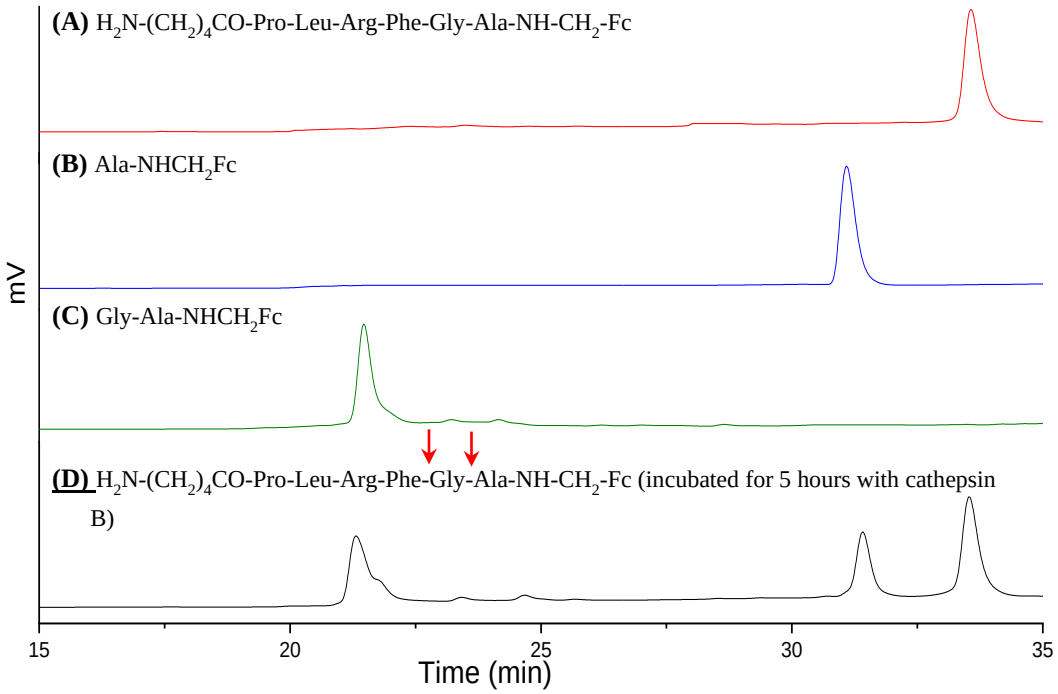

Figure 3.12 Determination of cleavage sites of the hexapeptide using HPLC. (A) HPLC chart of H_2N-$(CH_2)_4$CO-Pro-Leu-Arg-Phe-Gly-Ala-NH-CH_2-Fc in 50 mM MES (pH 5.0) and 250 mM NaCl. The hexapeptide appeared at 33.5 min in the HPLC chart and its structure was verified by mass spectrometry analysis. (B) HPLC chart of Ala-$NHCH_2$Fc in 50 mM MES (pH 5.0) and 250 mM NaCl. The Ala-$NHCH_2$Fc appeared at 31.1 min in the HPLC chart and its structure was verified by ^{1}H and ^{13}C NMR analysis. (C) HPLC chart of Gly-Ala-$NHCH_2$Fc in 50 mM MES (pH 5.0) and 250 mM NaCl. The Gly-Ala-$NHCH_2$Fc appeared at 21.6 min in the HPLC chart and its structure was verified by ^{1}H and ^{13}C NMR analysis. (D) HPLC chart of 6.5 mM H_2N-$(CH_2)_4$CO-Pro-Leu-Arg-Phe-Gly-Ala-NH-CH_2-Fc in 50 mM MES (pH 5.0) and 250 mM NaCl incubated with 5.75 ng/µL (0.17 µM) cathepsin B for 5 hours. Absorbance peak at 31.4 min was showed to be Ala-$NHCH_2$Fc. Absorbance peak at 22.1 min was showed to be Gly-Ala-$NHCH_2$Fc. (This HPLC experiment was done by Dr. Huafang Fan in Dr. Duy H. Hua's laboratory.) Copyright (2019) American Chemical Society.

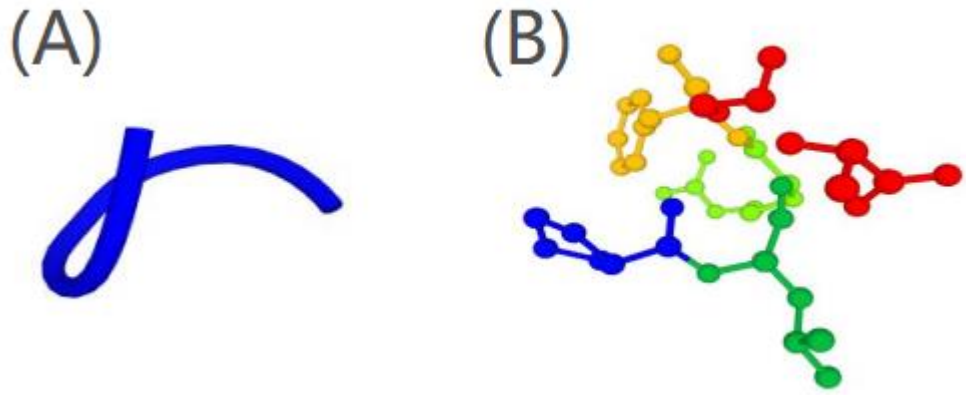

Figure 3.13 Computational calculated minimum structure of peptide #4. (A) a line presentation. (B) a ball-and-stick presentation. Copyright (2019) American Chemical Society.

3.5.6 Proteolysis rate dependence on the pH value and ionic strength of electrolytes

The effect of the pH value of the electrolyte (i.e. assay buffer) on the proteolysis rate and cleavage site was investigated using PBS buffers (pH = 7.3) in comparison with the above-discussed MES buffer (pH = 5.0). Three concentrations (0.2X, 0.5X and 1X PBS) were studied to examine the effect of the ionic strength. Proteolysis of hexapeptide (peptide #4) functionalized VACNF NEAs were measured with 6.0 nM cathepsin B at 38.6º C in these buffers. As shown in Figures 3.14A-C, 0.2X PBS buffer yields the fastest decay (τ = 1654 s) compared to 0.5X PBS buffer (τ = 1863 s) and 1X PBS buffer (τ = 9506 s). The measured activity (i.e. 1/τ) in Figure 3.14D decreases from 12.6×10^{-4} s^{-1} in 25 mM MES buffer (pH = 5.0) to 6.0×10^{-4} s^{-1} in 0.2X PBS buffer, 5.4×10^{-4} s^{-1} in 0.5X PBS buffer, and 1.0×10^{-4} s^{-1} in 1X PBS buffer. This reflects that both the ionic strength and pH value affect the proteolysis rate. The higher pH value and higher ionic strengths in PBS may cause conformational changes in the protease and the peptides. Fortuitously, a relatively high protease activity, about a half of that in 25 mM MES buffer (pH = 5.0), can be

achieved in the 0.2X PBS buffer (pH = 7.3). Thus, the diluted neutral PBS buffer can serve as a common electrolyte in simultaneously detecting multiple proteases with different optimal pH values. The HPLC results in Figure 3.15 further confirmed the effects of the buffer concentration on the proteolysis rate and cleavage site.

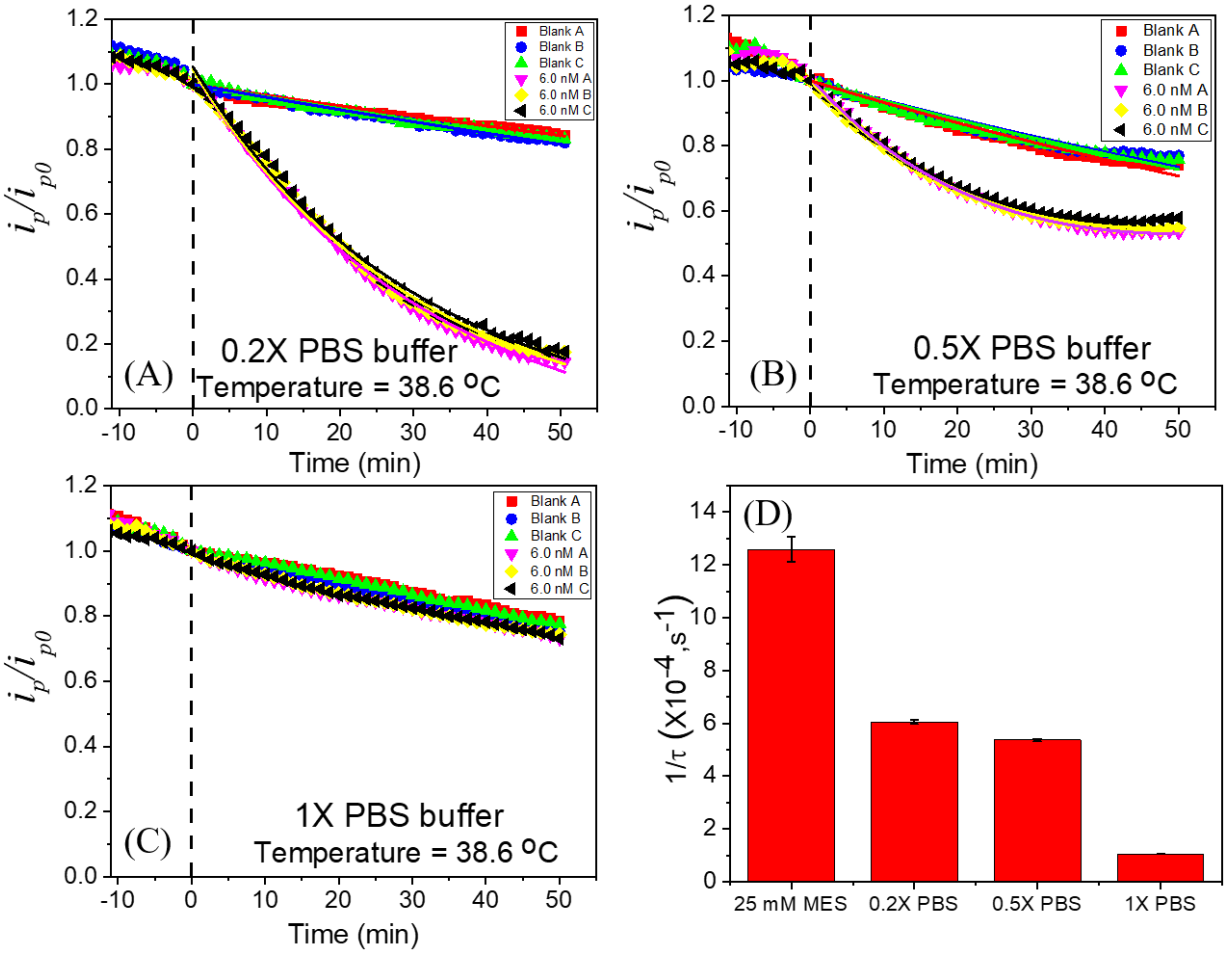

Figure 3.14 (A-C) The kinetic profile of the hexapeptide (peptide #4) modified VACNF NEA at pH = 7.3 in (A) 0.2X PBS buffer, (B) 0.5X PBS buffer, and (C) 1X PBS buffer. (D) Bar plot of 1/τ in 25 mM MES buffer (pH = 5.0) in comparison with 0.2X, 0.5X and 1.0X PBS buffers (pH = 7.3). The error bars represent the standard deviation obtained from three replicate measurements. Copyright (2019) American Chemical Society.

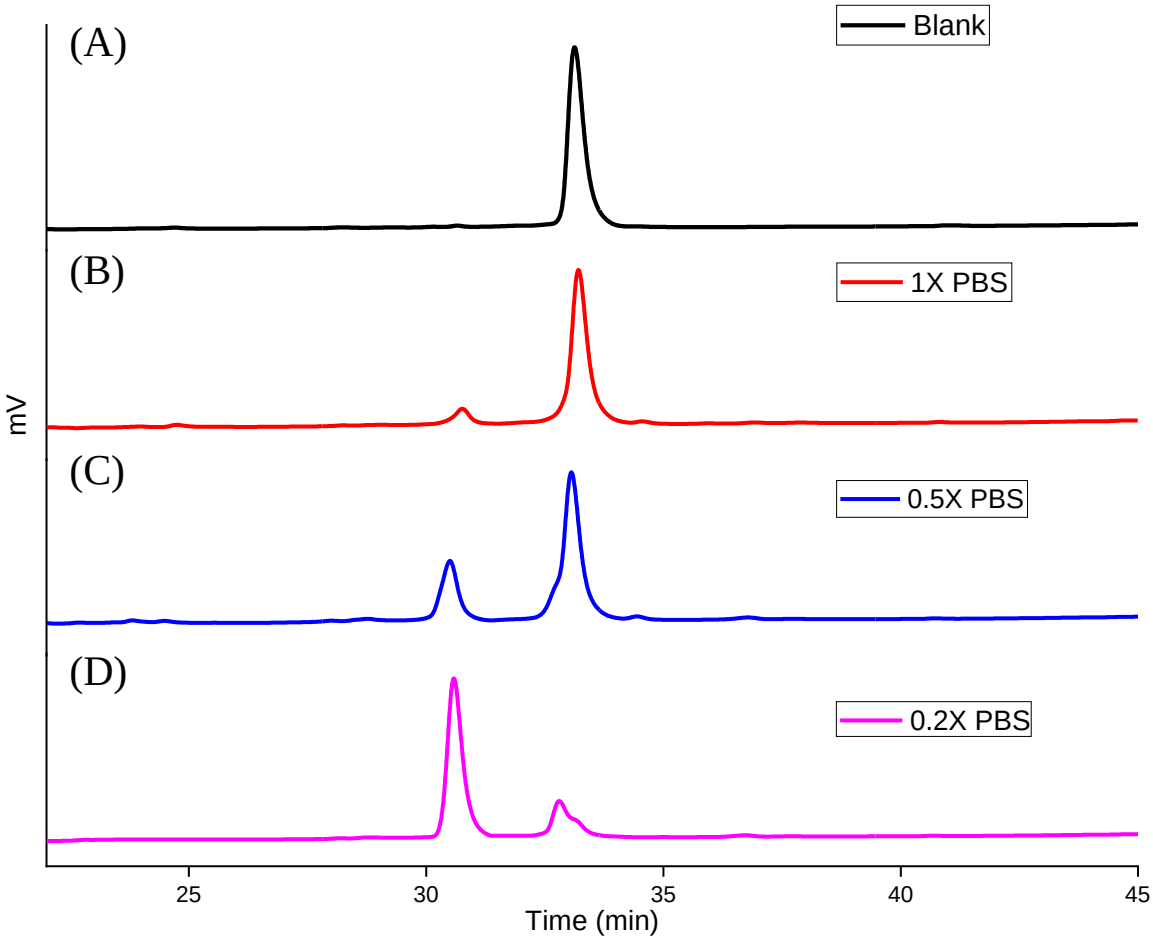

Figure 3.15 Determination of the proteolysis rate of cathepsin B using the hexapeptide (peptide #4) (H_2N-$(CH_2)_4$CO-Pro-Leu-Arg-Phe-Gly-Ala-NH-CH_2-Fc) in varied PBS buffer concentration using HPLC. (A) Blank experiment with hexapeptide in 1X PBS in absence of cathepsin B. Proteolysis chromatograms were obtained in a solution containing 6.5 mM hexapeptide and 5.75 ng/μL cathepsin B in (B) 1X PBS, (C) 0.5X PBS, and (D) 0.2X PBS. The pH was 7.3 in all solutions. The proteolysis reaction was allowed to run for 2 hr. The peak at 31.4 min is due a product of the proteolysis reaction (Ala-$NHCH_2$Fc) and the peak at 33.5 min arises from the intact hexapeptide substrate. (This HPLC experiment was done by Dr. Huafang Fan in Dr. Duy H. Hua's laboratory.) Copyright (2019) American Chemical Society.

3.6 Conclusion

This study has demonstrated the development of an activity-based electrochemical method to detect cathepsin B, a protease as an important prognostic factor for cancer. The protruding VACNF NEAs functionalized with specific peptide substrates labeled with Fc tag show reduced steric hindrance to protease and reliable AC voltammetry signal. The catalytic activity can be accurately derived as the inverse of the exponential decay time constant by measuring the kinetic proteolysis curve with repeated AC voltammetry. Different peptide lengths have been studied, revealing that the hexapeptide H_2N-$(CH_2)_4$-CO-Pro-Leu-Arg-Phe-Gly-Ala-NH-CH_2-Fc is the optimal substrate for measuring cathepsin B activity. The optimal AC frequency for AC voltammetry shifts to a lower value as the peptide length is increased, consistent with the larger separation between the VACNF tip and the Fc tag due to the upstanding peptides. The temperature has a significant effect on cathepsin B activity. The maximal cathepsin B activity is obtained at 38.6 °C, around the average body temperature. The limit of detection of cathepsin B activity and concentration have been determined to be 2.49×10^{-4} s^{-1} and 0.32 nM. This peptide substrate appears to be highly specific to cathepsin B and shows negligible cross-reactions with two other cancer-related proteases, i.e., ADAM10 and ADAM17. The results demonstrate the promising potential for a multiplex electronic chip for rapid profiling of the activity of multiple proteases in cancer diagnosis and treatment monitoring.

Chapter 4 - Fabrication and Characterization of Gold Microelectrode Array (Au MEA) Toward Protease Detection

Au MEA was synthesized by Dr. Morgan Anderson at NASA Ames Research Center and Stanford Nanofabrication Center

4.1 Introduction

Proteases play an essential role in various physiological activities. It targets the amide bonds between amino acids in peptides. Unregulated proteolysis can occur in cancer and neurodegeneration when proteases concentration is too high, or the endogenous inhibitors are lacking at the site of disease.[75-76] Up to now, there are many approaches that have been used to detect the protease, which includes enzyme-linked immunosorbent assays (ELISA), fluorescence resonance energy transfer (FRET), surface plasmon resonance assays (SPR). These methods offer a relatively high sensitivity and accuracy but require high-cost assay kits or equipment. Also, since proteases are catalytically active, quantitatively detecting only the enzyme concentration is less critical than quantifying the enzyme activity. For example, cathepsin B is secreted as an inactive zymogene, which needs activation to obtain the proteolytic function. Unfortunately, the antibodies used in the immunoassay fail to distinguish between the zymogen and active cathepsin B. Moreover, since different proteases interact with each other in complex activation cascades and networks, various proteases coexisted in the tumor cannot be discriminated by immunoassay in a short time. Hence there is a strong demand for developing bioanalytical techniques that can detect multiple protease activities simultaneously. Recently, array-based approaches have been developed for high throughput analysis of proteins and enzyme activities. As a high-throughput method, peptide array is an efficient way to simultaneously profile multiple protease activities in a complex sample such as human serum or plasma. In our previous studies, we have fabricated a

nanoelectrode array (NEA) fabricated with vertically aligned carbon nanofibers (VACNFs). By functionalizing the carbon nanofiber tips with ferrocene labeled peptide substrates, we successfully profiled the cathepsin B activity by fitting the electrochemical signal exponentially decay curve. The inverse of the decay time constant ($1/\tau$) reflects the cathepsin B activity.

However, our previous method is a single channel working electrode that is not able to detect multiple proteases simultaneously or functionalize different peptide substrates on the same chip. In this study, we have fabricated a 3 x 3 gold microelectrode array (MEA) and demonstrated the capability of simultaneous detection of cathepsin B activity by using three different peptide substrates (all three peptide substrates are specifically designed for cathepsin B) functionalized at the MEA. Besides, we have modified the fitting algorithm to obtain a more accurate result. These advances lay the foundation for the future multiplex electronic chips that can be used for the rapid detection of the protease activity profiles in disease diagnosis and treatment monitoring.

4.2 Fabrication of Au MEA

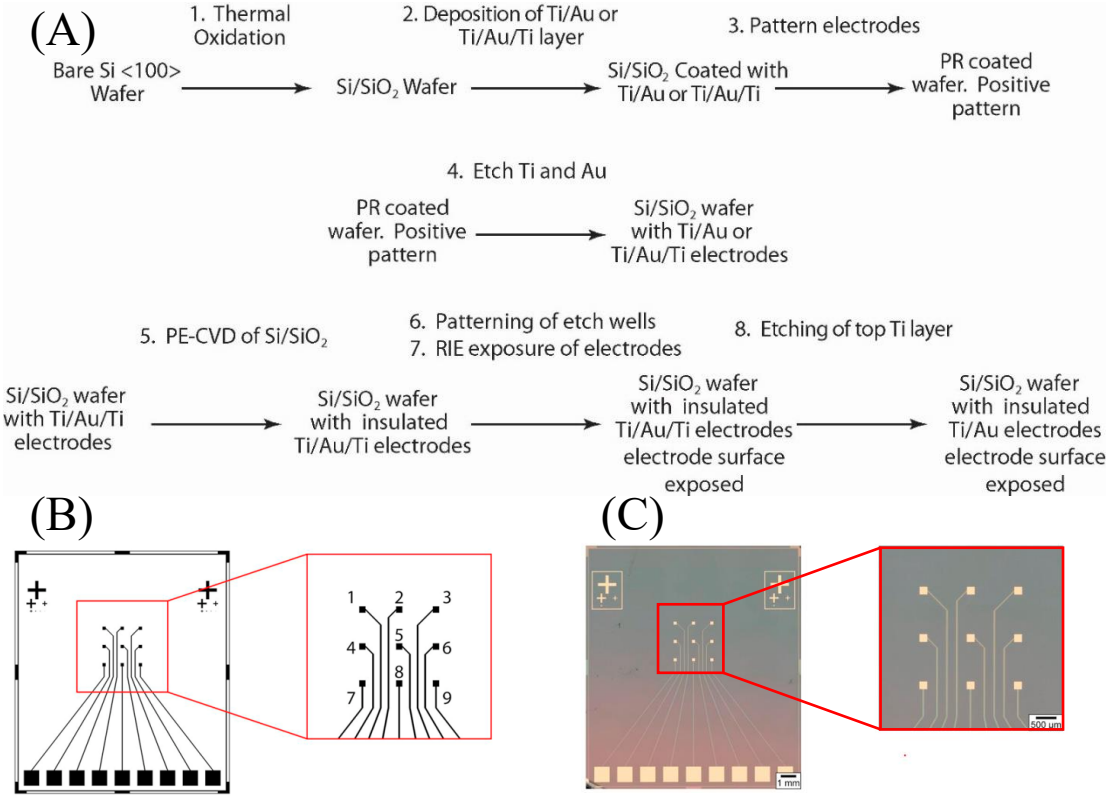

Figure 4.1 (A) Fabrication workflow for wafer-scale MEA fabrication. (B) Schematic diagram of the Au MEA chip layout with a zoom-in picture (right side) to illustrate the channel numbering scheme. (C) Optical micrographs of a fabricated Au MEA chip. Copyright (2020) Elsevier.

The Au MEA was fabricated at the Stanford Nanofabrication Facility (Stanford, CA). Figure 4.1 shows the workflow of the MEA fabrication processes. Thermal oxidized standard 4" Si<100> wafers were used as substrate after holding at 1100 ℃ for 45 min in the presence of gaseous H_2O. The oxidation process produced a thermal oxide with a thickness of ~550 nm. Then, the wafer was coated with 20 nm Ti and 100 nm Au and another 20 nm Ti by electron beam evaporation (Innotec ES26C, Battle Ground, WA). The wafers were then spin-coated with an automated spin-coating track (SVG 8400, San Jose, CA) with 1.0 µm SPR3612 positive

photoresist (Rohm and Haas Electronic Materials, Marlborough, MA) and exposed on a mask aligner (Karl Suss MA-1, Garching, Germany) with an exposure dose of 80 mJ/cm^2 (exposure time = 5.3 s) through a chrome photomask (FrontRange Photomask, Lake Havasu City, AZ). Next, the wafers were developed with an automated developing track (SVG 8600, San Jose, CA), leaving the electrode MEA design patterned in photoresist. The exposed areas on the wafers were then etched with a ratio of 1:50 of HF:H_2O to remove the top layer of Ti, with Transene TFA Au etchant to remove the Au layer, and again with 1:50 HF:H_2O to remove the bottom layer of Ti, leaving the MEA pattern (including contact pads, leads and the microelectrode surface). After etching, the photoresist was stripped off and a 1-µm thick layer of SiO_2 was deposited over the entire wafer by plasma-enhanced chemical vapor deposition (PE-CVD, Plasma-Therm Shuttlelock SLR-730-PECVD, St. Petersburg, FL) with 250 sccm 5% SiH_4/He, 800 sccm He and 1700 sccm N_2O at 350 ^oC, 1100 mTorr and 200 W for 15 min. Next, the SiO_2-coated substrate was spin-coated with a 1.0-µm layer of SPR3612 positive photoresist and subsequently exposed with an exposure dose of 80 mJ/cm^2 leaving the SiO_2 over the microelectrode surface and the contact pads exposed. The exposed SiO_2 was etched with CHF_3 plasma (2 sccm O_2 and 45 sccm CHF_3 at 5.0 mTorr for 8 min) using a reactive ion etcher (RIE, Plasma-Therm Versaline LL-ICP, St. Petersberg, FL), and then the top layer of Ti was etched with HF and H_2O (1:50) to expose the Au surface. Finally, the wafers were coated with a 5.0-µm layer of SPR3612 as a protective layer and the individual chips were diced with a wafer saw (DISCO DAD3240, Tokyo, Japan). Prior to use, the chips were sonicated in acetone and sequentially rinsed with acetone, methanol and isopropanol to remove any residual photoresist. Figure 4.2 illustrates the top and side view of the MEA structure and Figure 4.3 shows the SEM characterization of the fabricated Au MEAs.

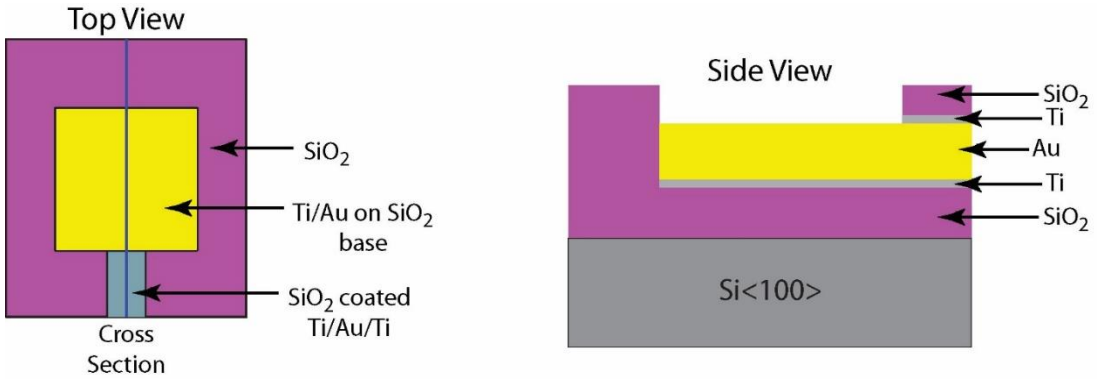

Figure 4.2 Top-view and side-view diagrams illustrating the structure of the MEA. Copyright (2020) Elsevier.

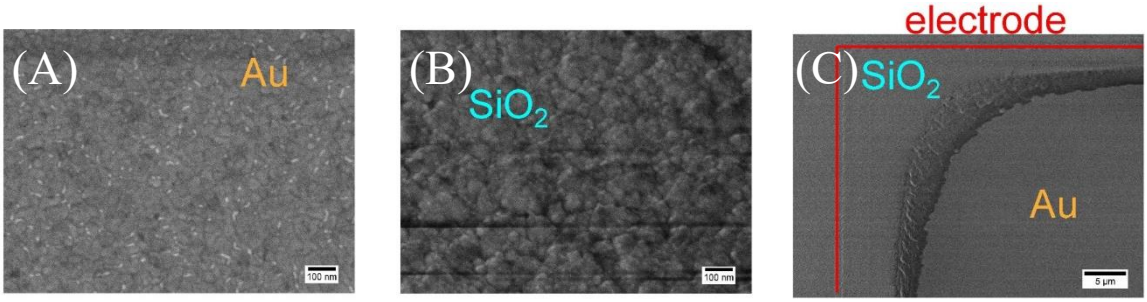

Figure 4.3 SEM images of different regions of a MEA: (A) an exposed Au surface, (B) the top surface of the PECVD SiO_2 layer, and (C) the boundary between the top SiO_2 layer and the exposed Au surface. (SEM images was accomplished by Dr. Morgan Anderson at NASA Ames Research Center.) Copyright (2020) Elsevier.

4.3 General characterization of Au MEA

Cyclic voltammetry characterization

To evaluate the performance of the Au MEA chip, we used cyclic voltammetry (CV) to characterize the electrochemical behavior of the sensor. Electrochemical cleaning of Au electrode by sweeping the DC voltage on the Au electrode is a common characterization method for evaluating the quality of Au electrodes. Here, we were using -0.60 to 0.70 V vs. MSE as the

potential window for 10 full cycles to clean the Au MEA. To avoid dissolution and delamination of both Au and underlying Ti adhesion layer by strong acid (i.e. 0.1 M H_2SO_4), phosphate buffer (pH = 7.4) was used as the electrolyte.

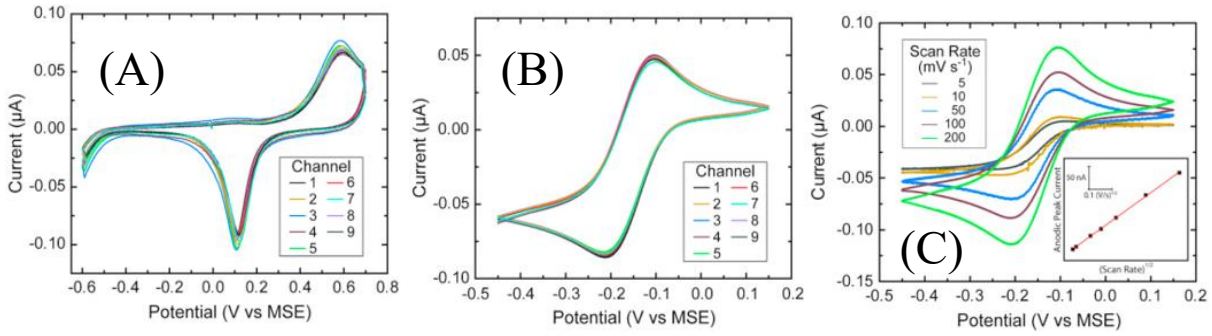

Figure 4.4 Electrochemical characterization of an insulated, unmodified MEA chip. (A) Electrochemical oxidation of Au performed in 0.10 M phosphate buffer (pH = 7.4). The measurements were performed on all nine channels simultaneously with scan rate (v) = 100 mV/s. (B) Simultaneous, multiplex measurement of $Fe(CN)_6^{4-}$ oxidation on all nine channels simultaneously. The measurements were obtained in a solution containing 1.0 mM $K_4Fe(CN)_6$ and 0.10 M KNO_3 with a v = 100 mV/s. (C) The dependence of v on $Fe(CN)_6^{4-}$ oxidation. The measurements were obtained using only channel 5 in a solution containing 1.0 mM $K_4Fe(CN)_6$ and 0.10 M KNO_3. Copyright (2020) Elsevier.

Figure 4.4A shows the tenth complete cycle of an electrochemical Au cleaning performed simultaneously on all nine electrodes on an insulated MEA. The water electrolysis can be observed at -0.60 V which causes a negative current. As the potential continues to move in the positive direction, the current becomes more positive, resulting in a localized peak at 0.60 V. This anodic current is indicative of the formation of Au_2O_3 on the electrode surface. The potential sweep

continues to 0.70 V which is known to form a complete monolayer of Au_2O_3 on the electrode surface.[77-80]

The potential sweep is then reversed. As the potential continues to move in the negative direction, a cathodic peak emerges at 0.11 V vs. MSE. This peak arises from the reduction of Au_2O_3 to Au, and the charge associated with the peak is directly related to the number of Au atoms present on the electrode surface. The average peak height is -94.3 ± 4.7 nA across all 9 electrodes, indicating that they all behave consistently with very similar exposed Au surface areas. These Au cleaning CVs show the characteristic features of clean polycrystalline Au electrodes.

CV measurement in $K_4Fe(CN)_6$ solution was another method to characterize the Au MEA. As shown in Figure 4.4B, the electrodes were cycled between -0.45 to 0.15 V vs. MSE at a scan rate of 100 mV/s in 1.0 M $K_4Fe(CN)_6$ containing 0.10 M KNO_3. Initially, the electrode potential was swept in the positive direction beginning at -0.45 V vs. MSE. As the potential increases, the anodic current increased due to the oxidation of $Fe(CN)_6^{4-}$ to $Fe(CN)_6^{3-}$ and forms a peak at -0.11 V vs. MSE followed by a gradual decay in the current. Upon reversing the potential sweep at 0.15 V vs. MSE, similar behavior was observed in the cathodic direction showing a peak at -0.21 V vs. MSE. The observed half peak potential ($E_{1/2}$) was -0.16 V vs. MSE. The average anodic and cathodic peak heights for all nine channels were 79.0 ± 1.8 nA and -80.9 ± 1.3 nA, respectively, demonstrating good agreement across all nine microelectrodes. This behavior is typical for electrochemical reactions of solution-based redox species. Another interesting phenomenon we observed was when we changed the scan rate in CV experiment, the data curves showed different characteristic feature. Briefly, at the low scan rate (5 mV/s), the CV trace showed a sigmoidal shape. As we know, the sigmoidal shape is the characteristic of microelectrode because the radial diffusion at the electrode edge is the dominate mass transfer method compared with linear

diffusion. This radial diffusion type results in a mass-transport limited steady-state current. As the *v* increases to 10 mV/s (yellow line), small anodic and cathodic peaks emerged at -0.102 V and -0.233 V, respectively. This occurs because at higher values of *v* the reactants near the electrode surface are depleted faster than diffusion layer development. As *v* further increased to 50 mV/s (blue line), the anodic and cathodic peaks shifted to -0.116 V and -0.206 V, respectively, and the peak heights increased. At even higher values of *v*, the peak potentials remain relatively constant and the peak heights continue to increase. The inset of Figure 4.4C shows a plot of the anodic values of i_p vs. $v^{1/2}$. The data for anodic i_p demonstrates a linear relationship with $v^{1/2}$, indicating that the observed signal is dominated by linear diffusion relative to radial diffusion. This is typical for electrochemical reactions of solution-based species under diffusion-controlled conditions. These results demonstrate that these Au MEAs behave as expected and are suitable for use as electrochemical sensors.

4.4 Design and multiplex functionalization of Au MEA toward protease detection

To design a multiplexed macro electrode array, which can simultaneously detect nine different signals, our Au MEA was modified with a SAM in an aqueous solution of mercaptohexanol and mercaptohexanoic acid to introduce carboxy group on the Au surface. The Fc labeled peptide substrates were then covalently functionalized on the electrode surface through amide bond in the presence of coupling reagent EDC and NHS. According to the preliminary data on 2.0 mm Au disk electrode, the density of functionalized peptide-Fc using this functionalization protocol was about 30.3 pmol/cm^2, giving an average spacing of 2.46 nm. Such surface coverage density is significantly lower than the maximum expected surface coverage for a close-packed Fc-

terminated SAM (460 pmol/cm^2). This low density promises adequate space between peptide substrates and reduces the steric hindrance in the proteolysis process. The mercaptohexanol moieties greatly reduces the contact between electrolyte and Au surface and effectively decreases the capacity of the electrode, thus improving the signal-to-noise ratio in the electrochemical measurements.

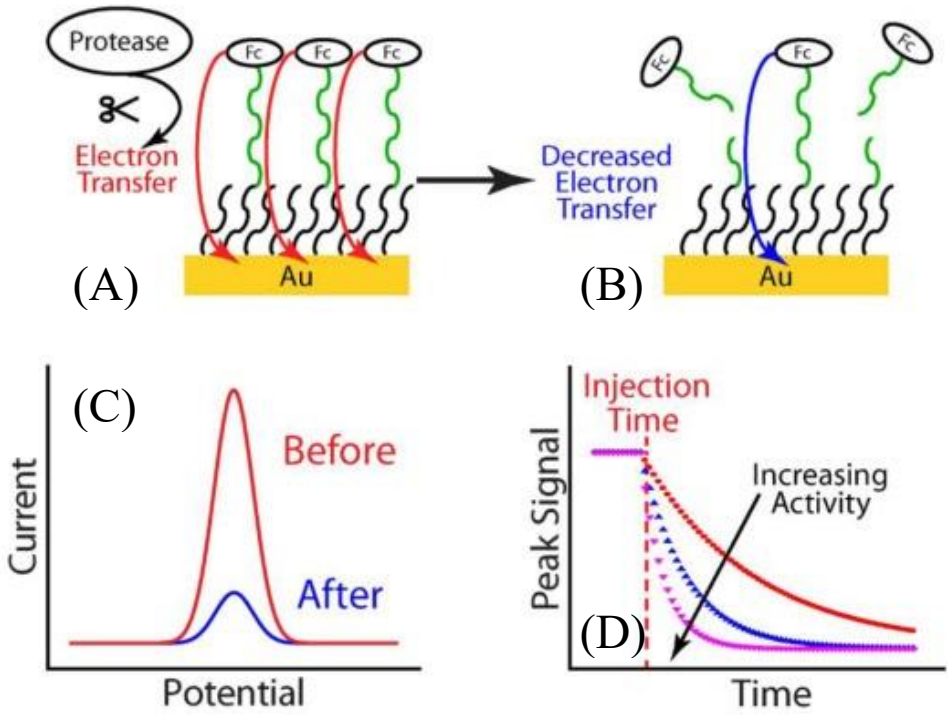

Figure 4.5 Schematic illustration of the proteolysis sensing mechanism. (A) The electrode before and (B) after a proteolysis reaction. The gold box represents the Au electrode surface, the wavy black lines are the alkane thiols bound to the electrode surface and the green wavy lines are the exposed Fc-terminated peptide sequence. (C) The schematic ACV curves before and after proteolysis. (D) The schematic kinetic proteolysis curves at varied protease activities. Copyright (2020) Elsevier.

Figure 4.5 shows the schematic diagram of the sensing strategy. The Au surface is close-packed with mercaptohexanol and mercaptohexanoic acid moieties, which are displayed by black wavy. The green wavy represents the Fc-peptide substrate, which is specific to the cathepsin B (Table 4.1). Before adding the enzyme, Fc can be oxidized into ferrocenium by transferring electrons to the Au electrode as depicted by the red arrows. This electron transfer corresponds to an ACV peak depicted by the red trace in Figure 4.5C. Figure 4.6A shows the raw ACV data of Fc-peptide functionalized Au MEA. The black trace shows the experimental signal, which revealed a Gaussian peak near -0.05 V vs. MSE on top of a tilt background as shown by the red line in Figure 4.6A. The baseline is subtracted from the ACV curve to result in a well-defined peak as shown in Figure 4.6B.

Table 4.1 Peptide-Fc substrates for cathepsin B detection in this study. (Peptide substrates were designed by Dr. Duy H. Hua, synthesized by Dr. Huafang Fan and Ms. Zhaoyang Ren in Dr. Duy H. Hua's laboratory.)

Peptide #	Peptide substrate sequences	Protease	Detection method
1	A-Pro-Leu-Ala-Gly-Val-Ala-B[a]	Cathepsin B	Electrochemical
2	A-Pro-Leu-Ala-Phe-Val-Ala-B	Cathepsin B	Electrochemical
3	A-Pro-Leu-Arg-Phe-Gly-Ala-B	Cathepsin B	Electrochemical

[a]A, linker $H_2N(CH_2)_4CO-$ at the N-terminus; B, redox tag $-NHCH_2Fc$ at the C-terminus.

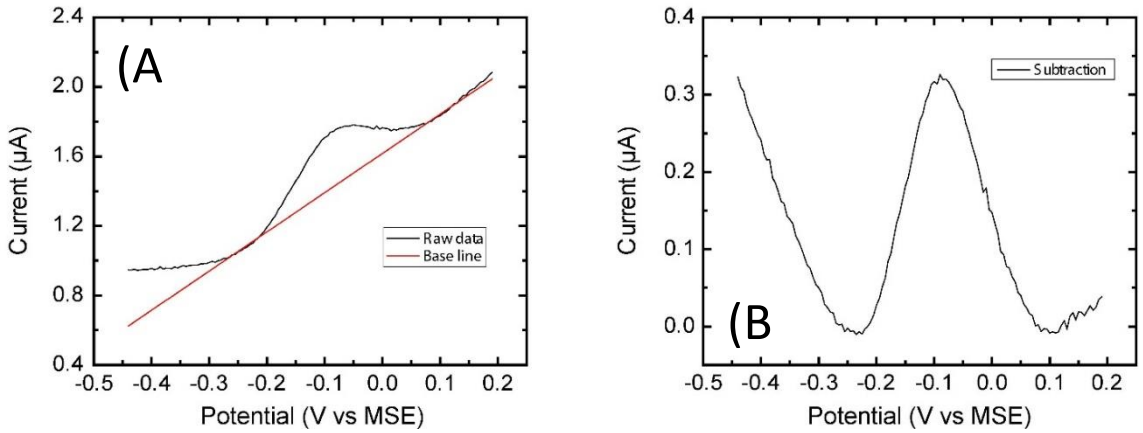

Figure 4.6 Baseline subtraction of ACV data. The ACV data was obtained on a single channel of a peptide-Fc modified MEA. (a) Raw data (black trace) and a linear baseline (red) of ACV data obtained with a peptide modified Au electrode. (b) The processed ACV curve after baseline subtraction. Copyright (2020) Elsevier.

By adding the protease (cathepsin B) in the cell, the peptides are cleaved by the enzyme, causing the Fc moieties diffused away from the Au MEA surface. This led to a decrease of electron transfer as illustrated by the blue arrow in Figure 4.5B. Finally, the ACV peak decreased with the proteolysis going which is represented by the blue trace in Figure 4.5C. Figure 4.5C shows a theoretical plot of the ACV peak height (i_p) vs. time of the proteolytic reaction where t = 0 min is defined as the first measurement after protease injection. These plots are called hereafter referred to as proteolysis plots. Focusing first on the red curve, prior to the injection time, i_p is stable. After the protease is injected into the electrochemical cell, the peak signal decays exponentially until approaching zero. As the activity of the protease increases, the proteolysis reaction rate is raised as depicted by the blue and pink curves, indicated by the faster decay in i_p.

In previous study, we have shown that this exponential decay in i_p corresponds to the proteolysis kinetics predicted by the Michaelis-Menten model for heterogeneous enzymatic reactions.[81] The flowing equation expresses the enzymatic reaction:

$$E + S_s \underset{k_{-1}}{\overset{k_1}{\leftrightarrow}} ES_s \overset{k_{cat}}{\Longrightarrow} E + P_s + P \tag{4.1}$$

Where E is the enzyme, S_s is the intact surface-bound peptide-Fc substrate, ES_s is the enzyme-substrate complex, P_s is the surface bound peptide product remaining after the proteolytic cleavage, P is the Fc-tagged peptide fragment which is free to diffuse into solution, and k_1, k_{-1}, *and*

k_{cat} are the rate constants of the respective reactions. Based on the model, the decay rate, ν, can be described as

$$\nu = -\frac{d\Gamma_{Ss}}{dt} = \frac{k_{cat}}{K_M + [E_0]}[E_0]\Gamma_{Ss} \tag{4.2}$$

where Γ_{Ss} is the surface concentration of Ss and $K_M = (k_{cat} + k_{-1})/k_1$ is the Michaelis-Menten constant. Because $i_p \propto \Gamma_{Ss}$, we can write:

$$\frac{\Gamma_s}{\Gamma_{s0}} = \frac{i_p}{i_{p0}} \tag{4.3}$$

By assuming $K_M \gg [E_0]$ and combining equation (4.2) and equation (4.3), we have:

$$-\frac{d\,{}^{i_p}/_{i_{p0}}}{dt} \approx \frac{k_{cat}}{K_M}[E_0]({}^{i_p}/_{i_{p0}}) \tag{4.4}$$

Integrating equation (4.4) with respect to i_p/i_{p0} yields:

$$t = \int -\frac{K_M}{k_{cat}[E_0]}\frac{1}{{}^{i_p}/_{i_{p0}}}\,d\left({}^{i_p}/_{i_{p0}}\right) = -\frac{K_M}{k_{cat}[E_0]}\mathrm{In}({}^{i_p}/_{i_{p0}}) \tag{4.5}$$

which can be rearranged to:

$$i_p = i_{p0}\exp\left[{}^{-t}/_{\tau}\right] \tag{4.6}$$

Where $1/\tau$ is:

$$\frac{1}{\tau} = (\frac{k_{cat}}{K_M})[E_0] \tag{4.7}$$

The value of $1/\tau$ is defined as the activity of the target protease on the specific peptide-Fc substrate and directly corresponds to the decay rate of i_p.

While this model has been demonstrated in previous reports, several non-idealities have been observed which we have sought to account for here.[82-83] These non-idealities are highlighted in Figure 4.7. First, as illustrated by Figure 4.7A, the baseline value of i_p decreased linearly prior to the injection of the target protease. This is attributed to the instability of the exposed Fc moiety.[84-85] To account for this, a linear term has been added to equation (4.6)

$$i_p = a\left[exp\left(-t/\tau\right)\right] + bt + c \quad (4.8)$$

and consequently, the value of i_{p0} is redefined as

$$i_{p0} = a + c \quad (4.9)$$

Equation (4.8) has been used to fit the proteolysis data and derive the value of $1/\tau$ for each proteolysis measurement.

Furthermore, there was a large drop in signal after the cathepsin B is injected into the electrochemical cell. The cause of this large decrease is illustrated in Figures 4.7B and 4.7C which show ACV traces obtained at t = 0 min and t = 1.2 min, respectively. The data in Figure 4.7B can be fitted into two overlapping Gaussian peaks: the Fc signal peak at -0.101 V vs. MSE and an interference peak at -0.243 V vs. MSE. The cause of the interference peak is not clear yet, but it was observed that it present in ACV traces in some experiments before t = 0 min and always disappeared after adding the protease solution, i.e. at the time with t > 0 min. Figure 4.7C shows the ACV trace obtained at t = 1.2 min, which is the first measurement after t = 0 min. Here, the ACV data can be reliably fitted to a single Gaussian peak (R^2 = 0.943). The presence of the interference peak at t = 0 min and its subsequent absence at later time causes a decrease in the overall current leading to a large drop in i_p observed at these timepoints. Consequently, all data analysis and fitting have been performed omitting the measurement at t = 0 min.

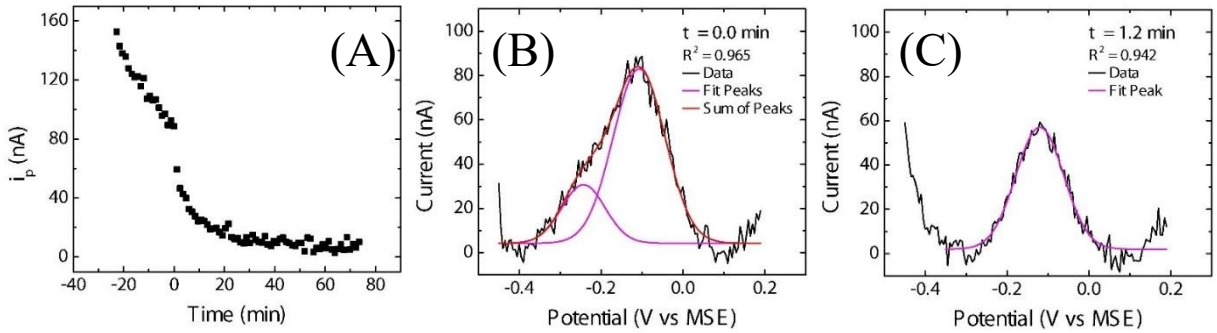

Figure 4.7 Examples of non-idealities in proteolytic measurements. (A) Full proteolysis curve demonstrating the initial drift in peak current drift prior to the protease injection ($t < 0$). The raw ACV curve showing (B) an interference peak at ~-0.25 V (vs. MSE) at t = 0.0 min and (C) the disappearance of the interference peak at t = 1.2 min shortly after adding the protease solution. Copyright (2020) Elsevier.

Functionalize the Au MEA with single peptide

Peptide #2 was a hexapeptide specifically designed for cathepsin B. Here, we used it to functionalize the Au MEA for the feasibility testing of the design. First, the whole Au MEA was modified by incubating the electrodes in an aqueous solution containing 1.0 mM mercaptohexanol and 0.2 mM mercaptohexanoic acid for 40 minutes for form a SAM with exposed hydroxyl and carboxyl terminal groups. Next, a thin layer (1.5 mm) of PDMS was aligned on the Au MEA, the PDMS was slotted before covering the MEA to expose the Au microelectrode and cover the contact line and surrounding area. Then, the top and the medium row of the electrodes (CH 1-6) were incubated in an aqueous solution containing 0.20 g/l EDC, 0.20 g/l sulfo-NHS and 2.0 mM of the peptide-Fc substrate (Peptide #2) for 2 hours to tether the peptide-Fc to the SAM. The bottom row (CH 7-9) was incubated with a solution containing 0.20 g/l EDC, 0.20 g/l sulfo-NHS but omitting the peptide-Fc substrate.

Functionalize the Au MEA with three different peptides

From previous study, this Au MEA shows a great potential toward multiplex detection. We have partially functionalized (CH1-6) the Au MEA with peptide #1, and it shows a distinct difference compared with the control group (CH 7-9). The Fc signal in the control group was negligible and well defined in the experimental group. However, the purpose of this Au MEA is

to fulfill the multiplexed detection, which offers the enhanced capability for medical diagnosis and health monitoring involving complex samples. Here, we functionalized the MEA with three different peptide substrates (CH 1-3 were functionalized with Peptide #1, CH 4-6 were functionalized with Peptide #2, and CH 7-9 were functionalized with Peptide #3). Different substrates give different binding energy with the cathepsin. Hence, it is not surprising to see the variation of proteolysis rate and decay constant.

4.5 Analysis of cathepsin B activity using Au MEA

Functionalize the Au MEA with single peptide

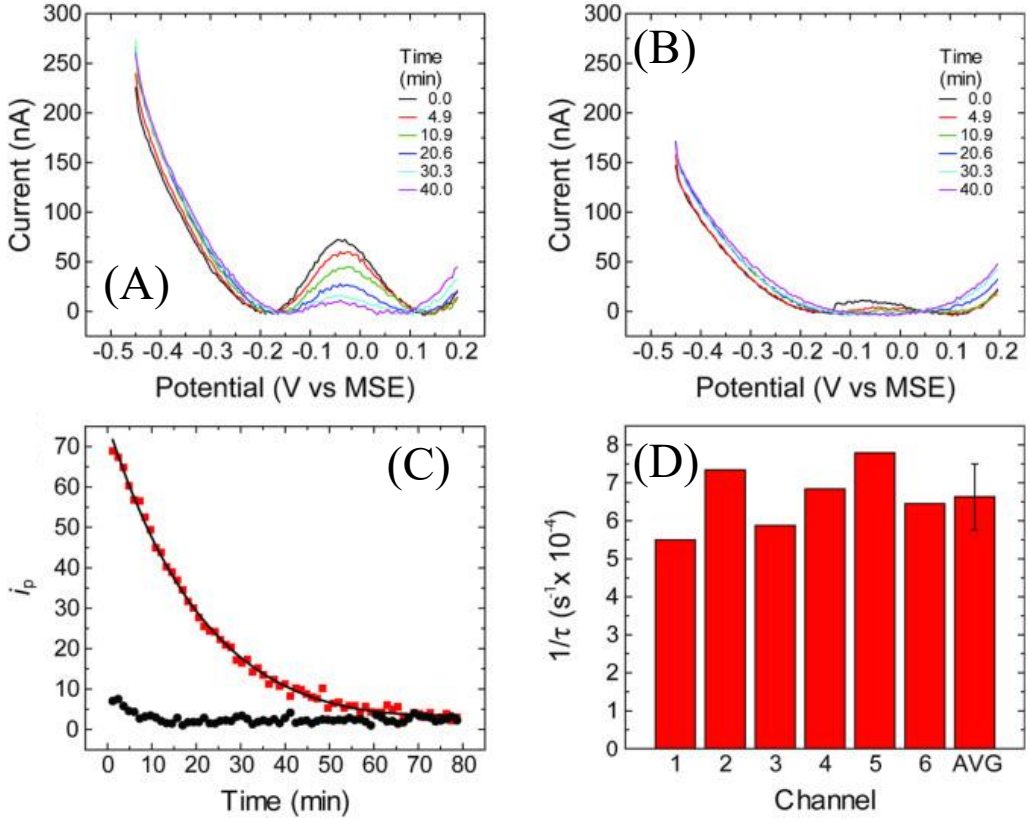

Figure 4.8 Proteolysis measurements obtained with an Au MEA. Measurements were performed in a solution containing 50 mM MES buffer (pH = 5.0) and 6.0 nM cathepsin B. The protease was injected at *t* = 0.0 min. (A) ACVs obtained at a microelectrode modified with peptide #2. (B)

ACVs obtained at a control microelectrode, which was passivated with mercaptohexanol/mercaptohexanoic acid and subsequently treated with an aqueous solution containing 0.20 g/l EDC and 0.20 g/l sulfo-NHS. (C) Proteolysis curves showing the relationship between i_p vs. reaction time for the peptide #2 modified (red squares) and the passivated microelectrodes (black circles) shown in (A) and (B), respectively. The black line represents the exponential fit of the peptide #2 modified microelectrode using eq. 4.8. (D) Bar graph showing the fitted values of $1/\tau$ for all of peptide #2 modified channels (CH 1–6) obtained simultaneously with the data shown in (A), (B) and (C). Copyright (2020) Elsevier.

Figures 4.8A and 4.8B show the baseline subtracted ACV traces for adjacent SAM/peptide-Fc modified (Peptide #2, CH 4) and a SAM passivated (CH 7) electrodes obtained at various time points. These measurements are performed in a solution containing 25 mM MES buffer (pH = 5.0). Immediately after t = 0, a solution containing 6.0 nM cathepsin B is injected into the electrochemical cell. In Figure 4.8A, the trace obtained at t = 0.0 min shows a Gaussian-shaped peak with i_p = 72.5 nA at -0.05 V vs. MSE. At t = 4.9 min, i_p has decreased to 60.3 nA but the peak position has not changed significantly. This observable decrease in i_p occurs as a result of the cleavage and dissipation of peptide-Fc molecules caused by the proteolysis reaction. As t increases, i_p continues to decrease until it reaches 20.0 nA at t = 40.0 min. The value of i_p further decreases beyond t = 40.0 min.

Figure 4.8B shows the control curves obtained on a passivated electrode without peptide-Fc functionalities (CH 7) as described above. These results are obtained simultaneously with the results shown in Figure 4.8A. Here, at t = 0.0 min, a small (11.9 nA) peak can be observed at -0.06 V vs. MSE. This peak is slightly larger than the background noise and is likely due to a small

amount of cross-contamination during the modification process. At t = 10.9 min and later, no observable peak can be distinguished from the background signal.

For comparison, Figure 4.9 shows ACV traces from all 9 channels which were simultaneously obtained during the experiment shown in Figure 4.8. Each frame shows background subtracted ACV traces obtained before (t = 0.0 min, black trace) and after (t = 79.9 min, red trace) the proteolysis reaction. The traces are plotted on the same scale to highlight the differences between the 6 SAM/peptide modified electrodes (CH 1-6) and the 3 SAM modified electrodes (CH 7-9). The 6 SAM modified electrodes show a Gaussian peak corresponding to the presence of the peptide-Fc substrate bound to the electrode surface. The peak potential (E_p) varies slightly from channel to channel (E_p = -0.03 ± 0.01 V vs. MSE), which is mainly due to variations in background subtraction. The average value of i_p before proteolysis is 93.1 ± 18.8 nA across all 6 of the SAM/peptide-Fc modified electrodes. The relatively small variation in i_p is due to the differences in the surface density and conformation of the peptide-Fc tags on the electrode surfaces which can change with the exposed carboxyl functionalities on the surface and the EDC/NHS coupling efficiency. After proteolysis, there is no obvious peak remaining and the average i at -0.03 V is 1.4 ± 3.3 nA, which is within the noise of the measurements. In contrast, the value of i_p measured on the passivated electrodes (CH 7-9) before and after proteolysis was 10.1 ± 9.9 nA and 0.0 ± 6.9 nA, respectively.

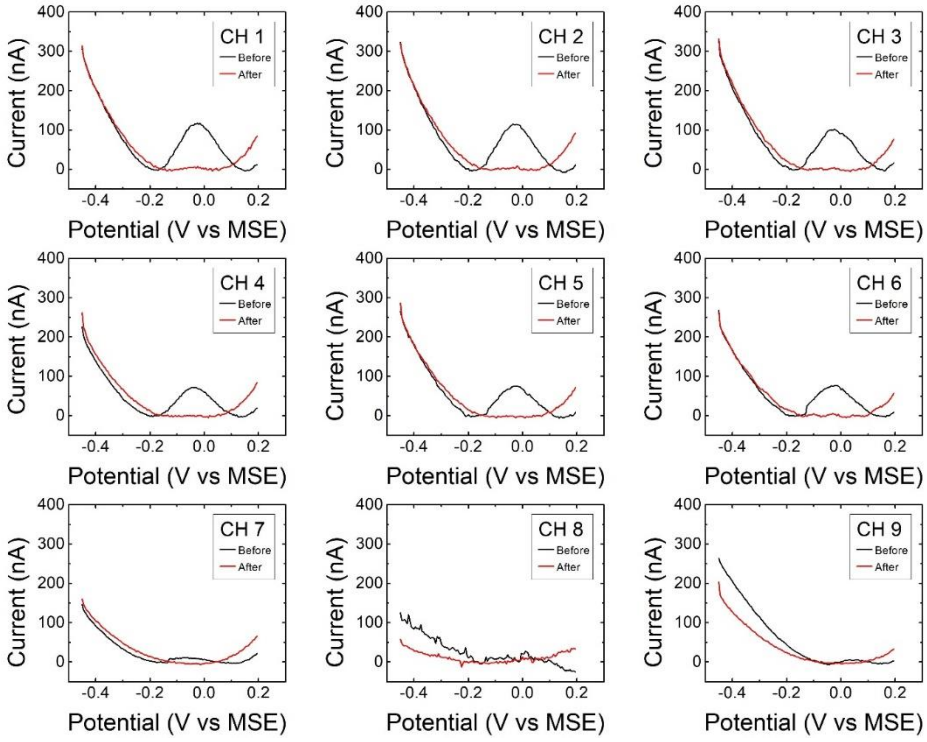

Figure 4.9 ACVs obtained on a modified Au MEA corresponding to Figure 4.8 and Figure 4.10. Channels 1-6 were modified peptide-Fc (peptide #2) by (i) incubating the electrodes in an aqueous solution containing 1.0 mM mercaptohexanol and 0.2 mM mercaptohexanoic acid for 40 minutes to form a SAM with exposed hydroxyl and carboxyl terminal groups and (ii) incubating the SAM modified electrodes with an aqueous solution containing 0.20 g/l EDC, 0.20 g/l sulfo-NHS and 2.0 mM of the peptide-Fc substrate for 2 hours to tether the peptide-Fc substrate (peptide #2) to the terminal ends of the alkanethiol SAM. Channels 7-9 are control electrodes which were prepared by forming the SAM in the same way as channels 1-6 and then incubated in an aqueous solution of 0.20 g/l EDC and 0.20 g/l sulfo-NHS without the presence of the peptide-Fc substrate. The black traces show the ACVs obtained during proteolysis with 6.0 nM cathepsin B at t = 0.0 min and the red traces show the ACVs obtained at t = 73.5 min. Copyright (2020) Elsevier.

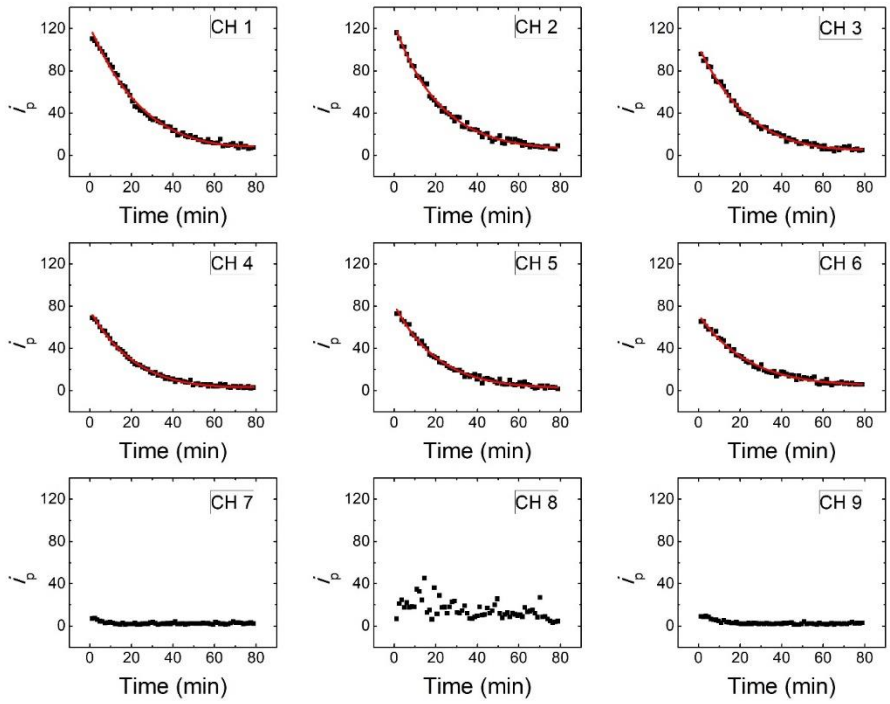

Figure 4.10 Proteolysis curves for the data shown in Figure 4.8 and Figure 4.9. The black squares represent the measured values of i_p and the red lines shown for channels 1-6 are fitting curves to the experimental data. Channels 7-9 were not fitted because there is no clear exponential decay, as these electrodes were not treated with the peptide-Fc substrate. The first data point for each graph was omitted and excluded from the fitting as discussed in the data processing section and Figure 4.7. Copyright (2020) Elsevier.

Figure 4.8C shows the proteolysis curves obtained from the data in Figures 4.8A and 4.8B. Here the red squares show the results obtained from an electrode which has been functionalized with the peptide-Fc substrate Peptide #2 (CH 4), and the black line corresponds to the exponential fit of that data. Here, the first data point is not plotted, and is not included in the exponential fit due to the agitation of the solution when adding the protease solution. The fit shows good agreement with the data ($R^2 = 0.997$) and the fitted value of $1/\tau$ is 6.84×10^{-4} s^{-1}. Figure 4.10 shows the proteolysis curves for all 9 channels. Each peptide-Fc functionalized electrode shows a clear

value of i_p ranging from 65.5 nA to 116.0 nA at the beginning of the proteolysis reaction (t = 1.2 min). Beyond t = 1.2 min, i_p shows a clear exponential decay. The red line shown in the frames corresponding to CH 1-6 are the exponential fits of the data for each channel. For each case, the fit shows good agreement ($R^2 > 0.98$) with the data. In contrast, CH 7-9 do not show any signs of exponential decay and, consequently, no fitting was performed.

Figure 4.8D is a bar graph representing the measured values of $1/\tau$ for CH 1-6 along with the average and standard deviation across the six channels. The average value of $1/\tau$ is (6.63 ± 0.87) x 10^{-4} s^{-1}. All fitting parameters in Eq 4.8 for each of the six peptide-Fc modified channels are shown in Table 4.2 along with the calculated value of i_{p0} and the R^2 of each fit. These results demonstrate that the activity ($1/\tau$) can be determined reproducibly (RSD = 0.13) and simultaneously on these selectively modified Au MEAs, and that the electrodes on the MEA can be selectively modified and clearly differentiated by ACV with minimal interference and cross-contamination between electrodes.

Table 4.2 Fit results for SAM/peptide-Fc (peptide #2) modified Au MEA (channels 1-6) in Figure 4.8, Figures 4.9, and 4.10. Copyright (2020) Elsevier.

Channel	$1/\tau$ x 10^{-4} (s^{-1})	a (nA)	b (nA s^{-1})	c (nA)	i_{p0} (nA)	R^2
1	5.50	154.3	0.374	-32.4	121.9	0.995
2	7.34	125.1	0.058	-1.3	123.8	0.995
3	5.88	127.6	0.287	-24.8	102.8	0.995
4	6.84	89.0	0.169	-13.3	75.7	0.997
5	7.79	83.8	0.044	-2.3	81.5	0.992
6	6.45	75.8	0.079	-3.8	72.0	0.989
Avg	6.63	109.3	0.169	-13.0	96.3	
St Dev	0.87	31.0	0.136	13.0	23.2	
RSD	0.13	0.28	0.81	-1.00	0.24	

Functionalize the Au MEA with three different peptides

Figure 4.11 shows a series of data obtained with multiple peptide-Fc substrates at once on a single MEA chip. For the experiments depicted here, the top row of electrodes (CH 1 - 3) are modified with peptide #1, the middle row of electrodes (CH 4 - 6) are modified with peptide #2, and the bottom row of electrodes (CH 7 - 9) are modified with peptide #3. Slotted PDMS mask was used in the functionalization process to avoid cross contamination.

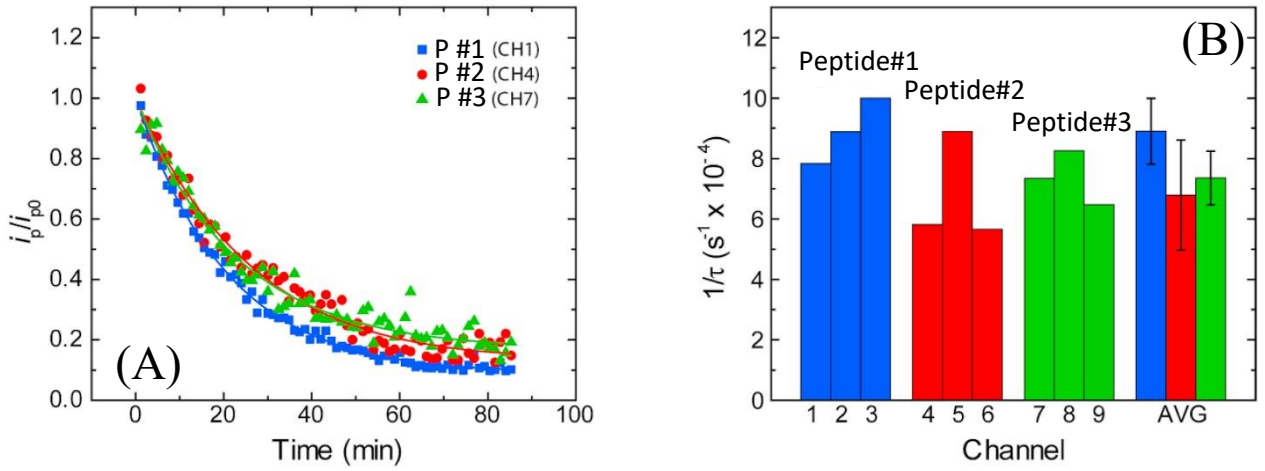

Figure 4.11 Proteolysis data obtained on an Au MEA chip where CH 1–3 were modified with peptide #1 (blue), CH 4–6 were modified with peptide #2 (red), and CH 7–9 were modified with peptide #3 (green). The experiment was performed in a solution containing 50 mM MES buffer (pH = 5.0) and 6.0 nM cathepsin B. (a) Representative proteolysis curves and fitting lines for electrodes modified with peptide #1 (CH 1), peptide #2 (CH 4) and peptide #3 (CH 7). The data is normalized to the fitted values i_{p0} derived from eq 4.8. (b) Bar graph showing the fitted values of $1/\tau$ for the channels modified with peptide #1 (CH 1–3), peptide #2 (CH 4–6), and peptide #3 (CH 7–9), respectively, and their average values at the far right with the standard deviation shown as the error bars. Copyright (2020) Elsevier.

Figure 4.11A shows examples of proteolysis curves obtained on CH 1 (Peptide #1, blue line), CH 4 (Peptide #2, red line), and CH 7 (Peptide #3, magenta line). Each of these proteolysis curves shows a slightly different activity based on the observable rate of decay in i_p. Figure 4.11B is a bar graph illustrating the differences in the measured values of $1/\tau$ broken down by channels with peptide #1 (shown in blue), peptide #2 (shown in red) and peptide #3 (shown in magenta), similar to Figure 4.8. Here the average values of $1/\tau$ were measured to be $(13.1 \pm 1.8) \times 10^{-4}$ s^{-1}, $(15.1 \pm 2.1) \times 10^{-4}$ s^{-1}, and $(8.14 \pm 1.6) \times 10^{-4}$ s^{-1} for peptide #1, #2 and #3, respectively. The proteolysis curves of each electrode are shown in Figure 4.12 and the fitting results for each curve are shown in Table 4.3. These three peptides show similar values of $1/\tau$ since the majority of the amino acid sequences are similar. As discussed in Figures A.5 and A.6 in Appendix B, cathepsin B was found to cleave peptide #1 and #2 between the Pro-Leu and Leu-Ala, respectively, while peptide #3 was cleaved in two locations: between Gly-Ala residues and between Phe-Gly residues as revealed by HPLC analyses in our previous study.[28]

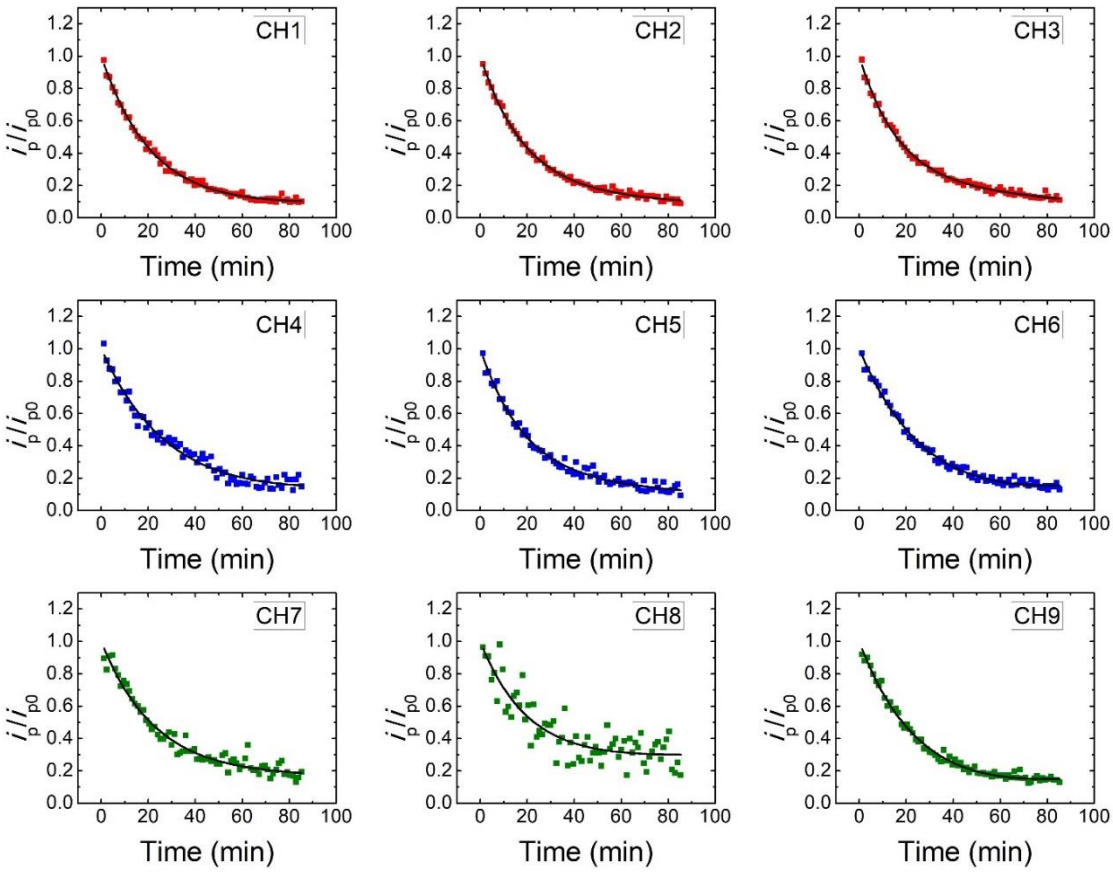

Figure 4.12 Proteolysis curves obtained with an Au MEA chip with the electrodes modified with peptide-Fc substrates peptide #1 (CH 1-3), peptide #2 (CH 4-6) and peptide #3 (CH 7-9) as shown in Figure 4.11. Copyright (2020) Elsevier.

Table 4.3 Fit results for SAM/peptide-Fc modified Au MEA in Figure 4.11 and Figure 4.12. All electrodes were functionalized with the peptides and coupling reagents as described before. Copyright (2020) Elsevier.

Peptide	Channel	$1/\tau$ x 10^{-4} (s^{-1})	a (nA)	b (nA s^{-1})	c (nA)	i_{p0} (nA)	R^2
Peptide #1	1	7.83	308.1	0.08	20.8	308.1	0.996
	2	8.88	347.2	-0.26	62.3	347.2	0.996
	3	10.00	248.6	-0.38	67.9	248.6	0.995
	AVG	8.90	301.3	-0.18	50.3	301.3	
	St Dev	1.08	49.7	0.24	25.7	49.7	
	RSD	0.12	0.16	-1.33	0.51	0.16	
Peptide #2	4	5.82	149.7	0.13	5.6	149.7	0.975
	5	8.89	146.4	-0.15	33.9	146.4	0.986
	6	5.66	222.9	0.48	-22.5	222.9	0.986
	AVG	6.79	173.0	0.15	5.7	173.0	
	St Dev	1.82	43.2	0.32	28.2	43.2	
	RSD	0.27	0.25	2.13	4.95	0.25	
Peptide #3	7	7.34	68.6	0.00	14.1	68.6	0.965
	8	8.26	100.3	0.06	33.2	100.3	0.776
	9	6.48	116.4	0.21	-5.0	116.4	0.991
	AVG	7.36	95.1	0.09	14.1	95.1	
	St Dev	0.89	24.3	0.11	19.1	24.3	
	RSD	0.12	0.26	1.22	1.35	0.26	

4.6 0.5X home-made phosphate buffer as electrolyte

The effect of electrolyte in cathepsin B proteolysis has been investigated in chapter 3. Here we have tested 0.5X home-made phosphate buffer (HM PB) as the assay electrolyte (pH = 7.3). The buffer was prepared in our lab, and it only contains potassium phosphate and monopotassium phosphate. Home-made phosphate buffer can reduce the poison of chloride to the Au surface, extending the lifetime of the MEA. Ten concentrations of cathepsin B (0.15 nM, 0.30 nM, 0.50

nM, 0.70 nM, 1.0 nM, 2.0 nM, 3.0 nM, 4.0 nM, 6.0 nM, and 12 nM) have been tested in 0.5X HM PB. The proteolysis of hexapeptide (peptide #2) functionalized Au MEA was measured at 38.6 ^{o}C. As shown in Table 4.4 and Figure 4.13, the measured activities (i.e., $1/\tau$) are much larger than our previous results obtained on Au MEA with the commercial MES buffer. Even the blank trial has a relatively fast decay rate ($1/\tau = 6.27x10^{-4}$, s^{-1}), compared with the blank trial measured in 25 mM MES buffer ($1/\tau = 2.23x10^{-5}$, s^{-1}). This reflects that different buffer affects the proteolysis rate. However, it is not consistent with our previous conclusion on VACNF NEA. In our previous study, we found that the proteolysis rate decreased if we changed the electrolyte from MES to PBS. As shown in Figure 4.13, the measured activity linearly increases with the cathepsin B concentration from blank to 1 nM. When the cathepsin B concentration goes above 1 nM, the slope of the increase drops. This has not been observed on VACNF NEA. Steric hindrance may cause the slope changes since the over-crowded cathepsin B adsorption on the flat Au surface may interfere with each other and limits the accessibility to the peptide substrates. The proteolytic activity of cathepsin B (6.0 nM) in Figure 4.13 is much higher than the earlier result in Figure 4.11. However, these two experiments were performed at the same temperature (38.6 ^{o}C) and identical functionalization procedures. Ionic strength and pH value of electrolytes are only two variant factors. The ionic strength of 25 mM MES buffer and 0.5X homemade phosphate buffer were 1.8 mM and 13.15 mM, respectively. The increased ionic strength leads to changes in the peptide substrate's secondary structures, mainly reflected in the increased random coil and decreased α-helices content. The destroyed secondary structure of peptide substrates are easier to be accessed by protease, finally caused a faster proteolytic rate. Compared with VACNF NEA, the dynamic range of cathepsin B detection on Au NEA is much smaller, possibly due to the large separation between the exposed VACNF tips and its high curvature generated by the nanoelectrode size. The LOD of

activity (i.e., $1/\tau$) can be determined as 8.37 x $10^{-4}s^{-1}$ by eq. 3.8. The LOD of cathepsin B concentration can be derived from the calibration curve in Figure 4.13B, which shows the best linear fit to the data of 1/t versus the cathepsin B concentration below 1.0 nM. Since the best fit line slope is 3.8 x 10^{6} $M^{-1}s^{-1}$, the LOD of the cathepsin B concentration can be calculated as 58.42 pM by eq. 3.9. The enzyme LOD is ~5.5X lower than what we got on VACNF NEAs (0.32 nM). This may be caused by using different peptide substrates, buffer solution, or working electrodes.

Table 4.4 Measured activity and standard deviation of different concentrations of cathepsin B in 0.5X HM PB.

Cathepsin B concentration	Mean value of $1/\tau$ ($X10^{-4}$, s^{-1})	STD	Background subtracted $1/\tau$ ($X10^{-4}$, s^{-1})	STD (propagation of uncertainty)
Blank	6.27	0.74	0	1.05
0.15 nM	16.40	2.92	10.13	3.01
0.30 nM	20.27	1.19	14	1.4
0.50 nM	26.19	1.71	19.92	1.86
0.70 nM	32.14	3.04	25.87	3.13
1.0 nM	42.1	3.74	35.83	3.81
2.0 nM	46.89	6.14	40.62	6.18
3.0 nM	44.91	3.96	38.64	4.03
4.0 nM	46.6	3.21	40.33	3.29
6.0 nM	50.23	7.07	43.96	7.11
12 nM	65.2	6.58	58.93	6.62

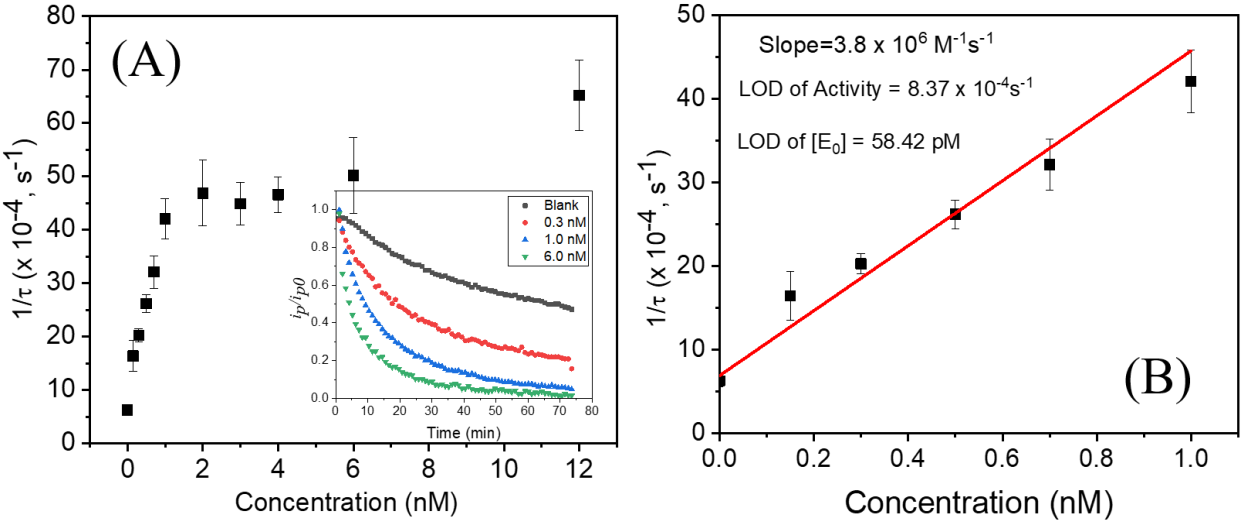

Figure 4.13 Measured activity vs. cathepsin B concentration. The measurement was performed in 0.5X HM PB. The temperature was 38.6 ^{o}C. The error bars represent the standard deviation from seven replicates (n=7). Insert of the panel (A) is the normalized peak current vs. time with different cathepsin B concentrations. (B) The enlarged linear portion below 1.0 nM. The LOD of activity is 8.37 x $10^{-4}s^{-1}$. The LOD of cathepsin B enzyme concentration is 58.42 pM.

4.7 Conclusion

In summary, we have demonstrated the fabrication of an individually addressed 3x3 gold MEA and systematic characterization for rapid multiplex electrochemical detection of cathepsin B activity. The microelectrode arrays are fabricated on 4" Si wafers containing 20 MEA chips. Each gold microelectrodes are about 200 μm x 200 μm in size. The chip surface is protected with a 1-μm thick layer of SiO_2 with only the active electrode surface and the electrical contact areas exposed. Highly consistent signals among the nine microelectrodes have been obtained in electrochemical cleaning and electrochemical characterization with benchmark redox species. Selective functionalization of the gold microelectrode surface with specific ferrocene-labeled

peptide molecules has been achieved. The consistent proteolytic kinetics can be measured by monitoring the decay of the AC voltammetry signal of ferrocene as the peptide molecules are cleaved by cathepsin B. We further demonstrated the simultaneous detection of the proteolysis of cathepsin B on three specific hexapeptides on the same MEA, which can be used for rapid screening of potential peptide candidates. This study has established the sensor platform for future rapid detection of the activity profiles of multiple proteases towards cancer diagnosis.

Chapter 5 - Enzyme-linked Immunosorbent Assay (ELISA) for Protease Detection

Part of these ELISA experiments were accomplished by Jestin Gage Wright

5.1 Introduction

ELISA methods are the most widely used immunoassays for a battery of biomolecules such as enzymes, viruses, or pathogens. It offers a high specificity compared with other molecular methods owing to the antibody-epitope interaction.[86] Secondly, it has a high sample throughput, which means it can dramatically reduce the number of analyses for target molecules. Additionally, the enzyme amplification mechanism provides a high sensitivity for ELISA experiments. Therefore, since the 1970s, various ELISA methods have been developed, and there are many commercially available ELISA kits for a particular matrix of interest. Undoubtedly, this number will continue to grow.[87]

The general protocol of the ELISA experiment consists of the 96-well microplates coated with the primary antibody with specific binding to the target molecule. After washing off the unbound primary antibody, the uncoated spaces are passivated by bovine serum albumin (BSA) to reduce the nonspecific binding. Then the antigen analyte is added. Following an incubation step, unbound material is rinsed away, and the second antibody is added to form a sandwich structure, which has the antigen in the middle of two antibodies. After the third rinse, the second antibody in the sandwich structure is conjugated with an enzyme that can covert colorless substrate into a colored product. As the spectrophotometer collects the optical density of the colored product in the microplate well, quantitatively analyzing the concentration of antigen in matrix can be achieved.

As a sensitive and reliable, ELISA plays an essential role in cancer research. Chen *et al.* used ELISA to determine the sera levels of cathepsin, cathepsin C, u-PA in cancer patient.[88] Finally, their studies show an association of higher serum levels of cathepsin, cystatin C, and u-PA with lung cancer. Wang *et al.* integrated the cell phone imaging with a microchip ELISA to detect ovarian cancer from urine sample.[89] This simple, noninvasive strategy provides a solution to point-of-care to detect ovarian cancer among high-risk populations.

The purpose of this study is to build a standard method to detect protease concentration from the serum of patient and compare with our electrochemical measurement. As discussed before, ELISA method cannot extract the activity of the enzyme. By comparing the concentration and the activity of enzyme in cancer patient, we can better interpret the progression of the tumor.

5.2 Quantitative analysis of recombinant human cathepsin B in PBS buffer

Commercially available cathepsin B was diluted in 1X PBS buffer for building the calibration line. The 1X PBS buffer was prepared from phosphate-buffered saline powder (pH = 7.4, for preparing 1L solutions) (Millipore Sigma, Burlington, MA, USA). The Human Total Cathepsin B DuoSet ELISA and DuoSet ELISA Ancillary Reagent Kit 2 were purchased from R&D systems, Inc. (Minneapolis, MN, USA). This ELISA kit is based on the classic sandwich assay type, which means the primary antibody, cathepsin B enzyme, and second antibody form a complex in the microplates. All measurements were processed on the same microplate and the optical density was read out by Biotek EL 311SX Microplate Autoreader (Winooski, VT, USA). The wavelength of the ELISA reader was set at 450 nm.

A series of ELISA measurement have been carried out at different cathepsin B concentrations (blank, 0.625, 1.25, 2.5, 5, 10, 20, 40, 60, 80, 100, 150, 200, 250, 300, and 500 pM).

100 μL of the cathepsin B solutions were added in the primary antibody immobilized microplate well. After rinsing the plate three times, 100 μL of the second antibody was added in the well to form the sandwich structure. Next, unbound second antibody was rinsed and 100 μL of streptavidin-HRP was added to each well, followed by incubating the plate for 20 at room temperature. After another round of washing, adding 100 μL of substrate solution to each well. 20 min later, a stop solution was added to each well. The optical density of each well was determined immediately. As shown in Table 5.1, the distribution of different concentrations has been illustrated. Figure 5.1 is the cathepsin B concentration vs. the optical density from 0.625 to 500 pM. The inset shows the linear calibration curve of the cathepsin B ELISA experiment.

Table 5.1 Concentration of cathepsin B in each well. Blank well only contains solvent. (Solvent: 1% BSA, 1X PBS buffer)

	1	2	3	4
A	Blank	Blank	60 pM	60 pM
B	500 pM	500 pM	40 pM	40 pM
C	300 pM	300 pM	20 pM	20 pM
D	250 pM	250 pM	10 pM	10 pM
E	200 pM	200 pM	5 pM	5 pM
F	150 pM	150 pM	2.5 pM	2.5 pM
G	100 pM	100 pM	1.25 pM	1.25 pM
H	80 pM	80 pM	0.625 pM	0.625 pM

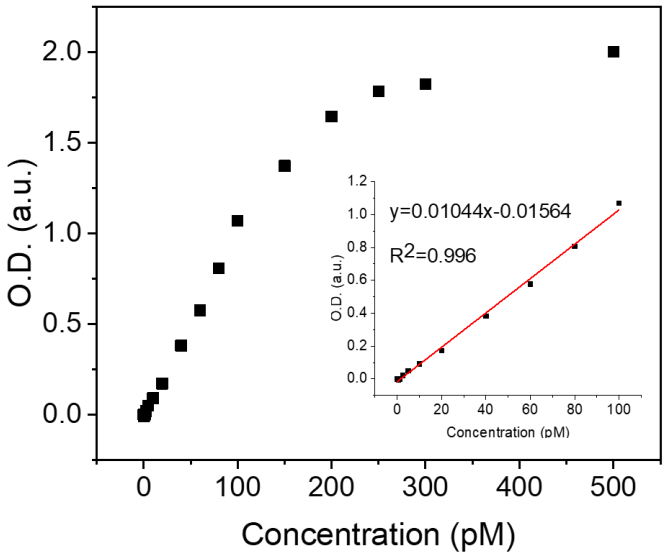

Figure 5.1 Commercial cathepsin B concentration versus the optical density from 0.625 to 500 pM, the inset shows the best fit line of the dynamic range (0.625 to 100 pM).

5.3 Quantitative analysis of cathepsin B in diluted human serum

The purpose of analyzing the human serum is because the complex matrix of the blood serum may have strong interference to cathepsin B or high concentration of cathepsin B. In the future, if we investigate the activity of spiked recombinant cathepsin B in human serum, the interference or cathepsin B in the human serum may change the real cathepsin B activity (k_{cat}/K_M) much lower or higher than what we measured in simple MES buffer solutions in previous studies. Hence it is necessary to investigate the concentration of cathepsin B concentration in human serum.

Table 5.2 Concentrations of diluted pooled human serum in each well (left) and the optical density of each well by using the ELISA reader (Biotek EL 311) (right). Blank well only contains solvent. (Solvent: 1% BSA, 1X PBS buffer)

	1	2	3
A	Blank	Blank	Blank
B	25%	25%	25%
C	10%	10%	10%
D	5%	5%	5%
E	2.5%	2.5%	2.5%
F	1%	1%	1%
G	0.5%	0.5%	0.5%
H	0.1%	0.1%	0.1%

	1	2	3
A	0	0.013	0.009
B	2.252	2.254	2.290
C	2.237	2.254	2.272
D	2.173	2.175	2.225
E	1.828	1.772	1.967
F	0.896	0.852	0.999
G	0.366	0.356	0.463
H	0.080	0.086	0.119

The pooled human serum used here was obtained from Innovative Research, Inc. (Novi, MI, USA). A series of sequential dilutions were prepared from the stock pooled human serum (blank, 25%, 10%, 5%, 2.5%, 1%, 0.5%, and 0.1%). The 1% BSA PBS buffer was used as the solvent. Table 5.2 illustrates the dilution strategy. Figure 5.2 shows the color change after adding color reagent, incubating for 20 min, and adding the stop solution. Figure 5.3 shows the relationship between the dilution factor and optical density. A linear relationship was found between 0.10% to 2.5%. If we compare the optical density reading in Figure 5.1 and 5.2, the linear relationship of cathepsin B in diluted human serum was from 10 to 300 pM. The signal reached a plateau after 5% shown the saturation of the signal, which was higher than 500 pM.

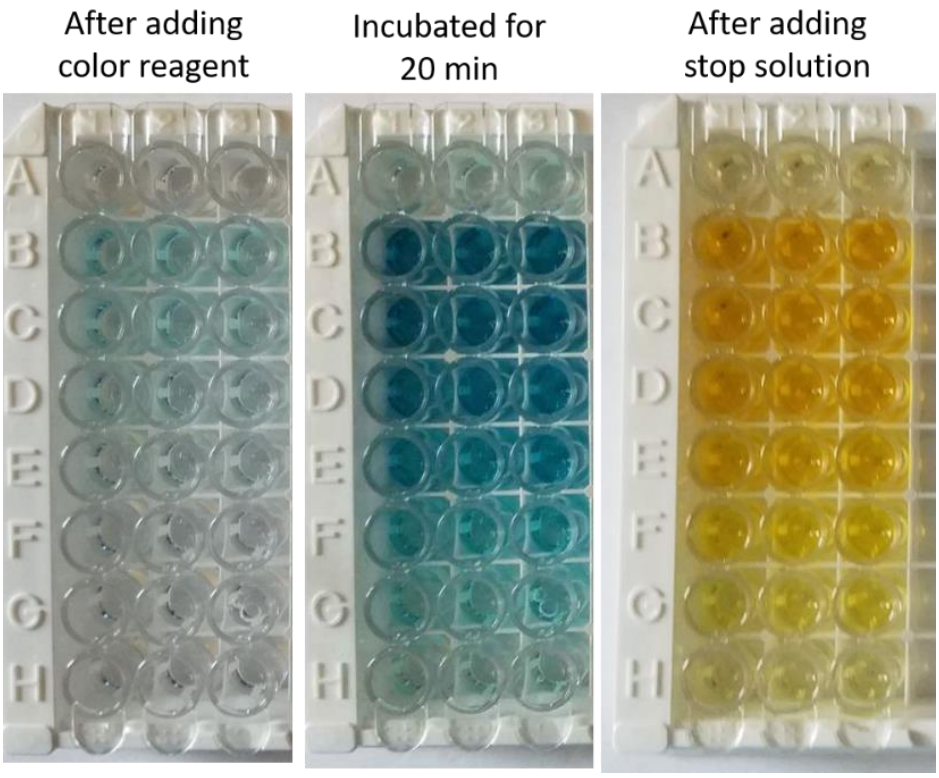

Figure 5.2 Color change after adding color reagent, incubating for 20 min, and adding the stop solution. Three columns are identical. From row A to H are blank, 25%, 10%, 5%, 2.5%, 1%, 0.5%, and 0.1%.

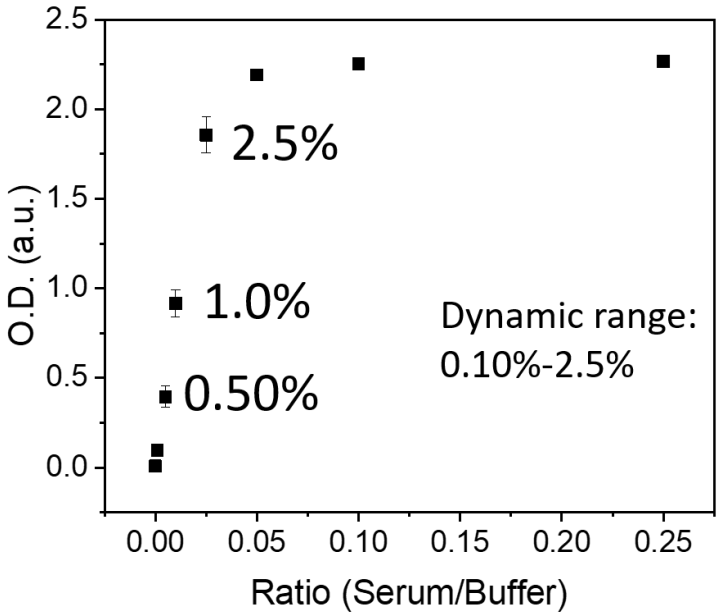

Figure 5.3 Relationship between dilution factor and optical density. A linear relationship was found between 0.10% to 2.5%.

Since the concentration of cathepsin B in the concentrated pooled human serum is high enough to saturate the ELISA signal, diluted pooled human serum (5%) spiked with different concentrations of commercial cathepsin B has been measured (Figure 5.4).

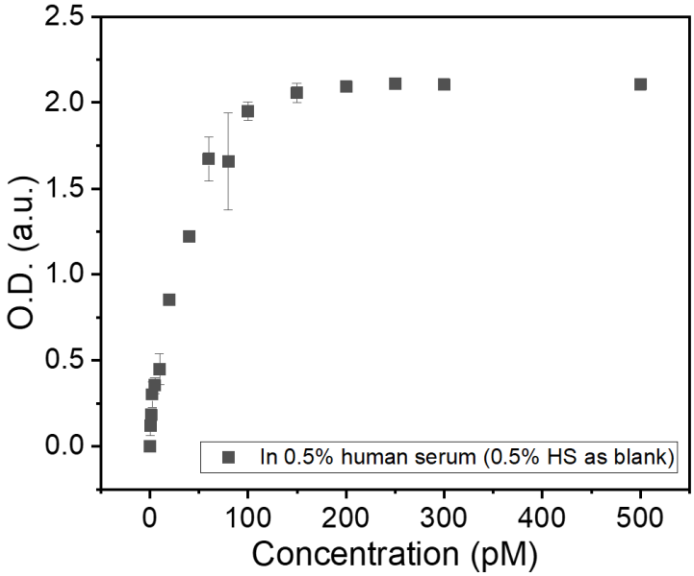

Figure 5.4 The 5% pooled human serum spiked with different concentrations of commercial cathepsin B.

5.4 Conclusion

In this part, we have used the traditional sandwich ELISA method to detect a various concentration of cathepsin B in PBS buffer, and 5% pooled human serum. The purpose of this work is to determine the dynamic range of cathepsin B concentrations in PBS buffer and diluted human serum. Based on the result, the cathepsin B concentration in whole pooled human serum is around 8.0 nM. Such high cathepsin B concentration revels the dilution of whole serum is necessary for both ELISA and electrochemical methods. In the future, the real patient sample measured by the electrochemical method can be quantitatively assessed by comparing these results.

Chapter 6 - Conclusion and Future Plan

In this dissertation, the carbon-based nanoelectrode array and gold microelectrode array have been used for developing biosensors for cancer-related protease detection. Our work is driven by the demand for point-of-care detection of cancer at an early stage to enhance the cure rate and decrease to cost of the patient. We hope our results will benefit other researchers on cancer early diagnosis. In the meantime, we expect our nanoelectrode array and macroelectrode array can provide solutions of device miniaturization and multiplex detection.

6.1 Electrochemical protease biosensor based on AC voltammetry using VACNFs NEA

This study has demonstrated the development of an activity-based electrochemical method to detect cathepsin B, a protease that is an important prognostic factor for cancer. The protruding VACNF NEAs functionalized with specific peptide substrates labeled with Fc tag show reduced steric hindrance to protease and reliable AC voltammetry signal. The catalytic activity can be accurately derived as the inverse of the exponential decay time constant by measuring the kinetic proteolysis curve with repeated AC voltammetry. Different peptide lengths have been studied, revealing that the hexapeptide H_2N-$(CH_2)_4$-CO-Pro-Leu-Arg-Phe-Gly-Ala-NH-CH_2-Fc is the optimal substrate for measuring cathepsin B activity. The optimal AC frequency for AC voltammetry shifts to lower value as the peptide length is increased, consistent with the larger separation between the VACNF tip and the Fc tag due to the upstanding peptides. The temperature has a significant effect on cathepsin B activity. The maximal cathepsin B activity is obtained at 38.6 °C, around the average body temperature. The limit of detection of cathepsin B activity and concentration have been determined to be 2.49×10^{-4} s^{-1} and 0.32 nM. This peptide substrate

appears to be highly specific to cathepsin B and shows negligible cross-reactions with two other cancer-related proteases, i.e., ADAM10 and ADAM17. The results demonstrate the promising potential for a multiplex electronic chip for rapid profiling of the activity of multiple proteases in cancer diagnosis and treatment monitoring.

In the future, the patterned VACNFs NEA can also be studied. First, the patterned VACNF NEA can be used for multiplexed detection by enhancing the throughput of the biosensor. A library of peptides, which is specific to various proteases, can be immobilized on each independent NEA. As described before, understanding the networks of the proteases in cancer progression can help researchers to understand the mechanism of cancer better. Second, the well-arranged VACNFs NEA can further decrease the background current and enhance the signal to background ratio.

We already fabricated the e-beam patterned NEAs, but the process is time-consuming and expensive. Thus, we tried to use UV lithography to pattern the NEAs. However, the contact Cr layer were peered off from the SiO_2 substrate and the growth of the fibers at the corner were not uniform causing a lot of defects on the chip. This might be caused by the unsecured metal deposition or the quality of photolithography. The current results demonstrate that we still need to optimize the design of the pattern (i.e., the size of each Ni catalysts and the spacing between Ni catalysts) or the protocol of the UV lithography (i.e., UV exposure time or photoresist developing time).

6.2 Electrochemical protease biosensor based on AC voltammetry using Au MEAs

We have demonstrated rapid multiplex electrochemical detection of cathepsin B activities through the fabrication of an individually addressed 3x3 Au MEA and systematic characterization.

The microelectrode arrays were fabricated on 4” Si wafers containing 20 MEA chips. The chip surface was protected with a 1-μm thick layer of SiO_2 with only the active electrode surface and the electrical contact areas exposed. Highly consistent signals among the nine microelectrodes have been obtained in electrochemical cleaning and electrochemical characterization with benchmark redox species. Selective functionalization of the Au microelectrode surface with specific ferrocene-labeled peptide molecules was achieved. The consistent proteolytic kinetics can be measured by monitoring the decay of the AC voltammetry signal of Fc as the peptide molecules are cleaved by cathepsin B. We further demonstrated the simultaneous detection of the proteolysis of cathepsin B on three specific hexapeptides on the same MEA, which can be used for rapid screening of potential peptide candidates.

This MEA chip shows a great potential on multiple proteases detection towards cancer diagnosis. The next directions of our research include: (1) Optimizing the peptide substrate sequences. It is well known that peptide sequences can form different 3D structures, which was determined by order of the amino acid. These 3D structures affect proteolysis efficiency. Because of the high throughout property, MEAs can speed up the substrate optimization study; (2) Design a portable potentiostat. The final goal of our research is to realize the point-of-care for cancer patient. Currently, we are using a nine channels potentiostat in the lab. It is ponderous (25 inches x 20 inches x 8 inches) and expensive (each module contains two channels and costs $5000). Minimizing the size and cost of the Potentiostat will determine the marketability of our MEA and is therefore another important obstacle.

References

1. Kaur, H.; Kumar, R.; Babu, J. N.; Mittal, S., Advances in arsenic biosensor development - A comprehensive review. *Biosens Bioelectron* **2015,** *63*, 533-545.

2. Janshoff, A.; Galla, H. J.; Steinem, C., Piezoelectric mass-sensing devices as biosensors - An alternative to optical biosensors? *Angew Chem Int Edit* **2000,** *39* (22), 4004-4032.

3. Parkhey, P.; Mohan, S. V., Chapter 6.1 - Biosensing Applications of Microbial Fuel Cell: Approach Toward Miniaturization. In *Microbial Electrochemical Technology*, Mohan, S. V.; Varjani, S.; Pandey, A., Eds. Elsevier: 2019; pp 977-997.

4. Ding, L.; Bond, A. M.; Zhai, J. P.; Zhang, J., Utilization of nanoparticle labels for signal amplification in ultrasensitive electrochemical affinity biosensors: A review. *Anal Chim Acta* **2013,** *797*, 1-12.

5. Caygill, R. L.; Blair, G. E.; Millner, P. A., A review on viral biosensors to detect human pathogens. *Anal Chim Acta* **2010,** *681* (1-2), 8-15.

6. Law, W. T.; Akmal, N.; Usmani, A., *Biomedical Diagnostic Science*. CRC Press: 2002.

7. Bobade, S.; Kalorey, D. R.; Warke, S., Biosensor Devices: A review on their biological applications. *Biosci Biotechno Res* **2016,** *9* (1), 132-137.

8. Wiseman, M. J., Nutrition and cancer: prevention and survival. *Brit J Nutr* **2019,** *122* (5), 481-487.

9. Sun, L.; Legood, R.; dos-Santos-Silva, I.; Gaiha, S. M.; Sadique, Z., Global treatment costs of breast cancer by stage: A systematic review. *Plos One* **2018,** *13* (11).

10. Saxena, U.; Das, A. B., Nanomaterials towards fabrication of cholesterol biosensors: Key roles and design approaches. *Biosens Bioelectron* **2016,** *75*, 196-205.

11. Guo, S. J.; Dong, S. J., Biomolecule-nanoparticle hybrids for electrochemical biosensors. *Trac-Trend Anal Chem* **2009,** *28* (1), 96-109.

12. Song, H. S.; Park, T. H., Integration of biomolecules and nanomaterials: Towards highly selective and sensitive biosensors. *Biotechnol J* **2011,** *6* (11), 1310-1316.

13. Georgakilas, V.; Perman, J. A.; Tucek, J.; Zboril, R., Broad Family of Carbon Nanoallotropes: Classification, Chemistry, and Applications of Fullerenes, Carbon Dots, Nanotubes, Graphene, Nanodiamonds, and Combined Superstructures. *Chem Rev* **2015,** *115* (11), 4744-4822.

14. Wilson, N. R.; Macpherson, J. V., Carbon nanotube tips for atomic force microscopy. *Nat Nanotechnol* **2009,** *4* (8), 483-491.

15. Kingston, C. T.; Simard, B., Fabrication of carbon nanotubes. *Analytical letters* **2003,** *36* (15), 3119-3145.

16. Jacobs, C. B.; Peairs, M. J.; Venton, B. J., Review: Carbon nanotube based electrochemical sensors for biomolecules. *Anal Chim Acta* **2010,** *662* (2), 105-127.

17. Hagstrom, S.; Lyon, H. B.; Somorjai, G., Surface Structures on the Clean Platinum (100) Surface. *Physical Review Letters* **1965,** *15*, 491-493.

18. May, J. W., Platinum Surface Leed Rings. *Surf Sci* **1969,** *17* (1), 267-&.

19. Angermann, H. H.; Horz, G., Influence of Sulfur on Surface Carbon Monolayer Formation and Graphite Growth on Nickel. *Appl Surf Sci* **1993,** *70-1*, 163-168.

20. Yu, Q. K.; Lian, J.; Siriponglert, S.; Li, H.; Chen, Y. P.; Pei, S. S., Graphene segregated on Ni surfaces and transferred to insulators. *Appl Phys Lett* **2008,** *93* (11).

21. Avouris, P.; Dimitrakopoulos, C., Graphene: synthesis and applications. *Materials Today* **2012,** *15* (3), 86-97.

22. Suvarnaphaet, P.; Pechprasarn, S., Graphene-Based Materials for Biosensors: A Review. *Sensors-Basel* **2017,** *17* (10).

23. Li, D. P.; Zhang, W. S.; Yu, X. Q.; Wang, Z. P.; Su, Z. Q.; Wei, G., When biomolecules meet graphene: from molecular level interactions to material design and applications. *Nanoscale* **2016,** *8* (47), 19491-19509.

24. Feng, L. C.; Xie, N.; Zhong, J., Carbon Nanofibers and Their Composites: A Review of Synthesizing, Properties and Applications. *Materials* **2014,** *7* (5), 3919-3945.

25. Wang, J.; Lin, Y. H., Functionalized carbon nanotubes and nanofibers for biosensing applications. *Trac-Trend Anal Chem* **2008,** *27* (7), 619-626.

26. Lee, C. S.; Baker, S. E.; Marcus, M. S.; Yang, W. S.; Eriksson, M. A.; Hamers, R. J., Electrically addressable biomolecular functionalization of carbon nanotube and carbon nanofiber electrodes. *Nano Lett* **2004,** *4* (9), 1713-1716.

27. Baker, S. E.; Tse, K. Y.; Hindin, E.; Nichols, B. M.; Clare, T. L.; Hamers, R. J., Covalent functionalization for biomolecular recognition on vertically aligned carbon nanofibers. *Chem Mater* **2005,** *17* (20), 4971-4978.

28. Song, Y.; Fan, H.; Anderson, M. J.; Wright, J. G.; Hua, D. H.; Koehne, J.; Meyyappan, M.; Li, J., Electrochemical Activity Assay for Protease Analysis Using Carbon Nanofiber Nanoelectrode Arrays. *Analytical Chemistry* **2019,** *91* (6), 3971-3979.

29. Bond, J. S., Proteases: History, discovery, and roles in health and disease. *J Biol Chem* **2019,** *294* (5), 1643-1651.

30. Mook, O. R. F.; Frederiks, W. M.; Van Noorden, C. J. F., The role of gelatinases in colorectal cancer progression and metastasis. *Bba-Rev Cancer* **2004,** *1705* (2), 69-89.

31. Han, N.; Jin, K. T.; He, K. F.; Cao, J.; Teng, L. S., Protease-activated receptors in cancer: A systematic review. *Oncol Lett* **2011,** *2* (4), 599-608.

32. Poole, A. R.; Tiltman, K. J.; Recklies, A. D.; Stoker, T. A. M., Differences in Secretion of Proteinase Cathepsin-B at Edges of Human Breast Carcinomas and Fibroadenomas. *Nature* **1978,** *273* (5663), 545-547.

33. Thomssen, C.; Schmitt, M.; Goretzki, L.; Oppelt, P.; Pache, L.; Dettmar, P.; Janicke, F.; Graeff, H., Prognostic value of the cysteine proteases cathespins B and cathepsin L in human breast cancer. *Clin Cancer Res* **1995,** *1* (7), 741-746.

34. Hirai, K.; Yokoyama, M.; Asano, G.; Tanaka, S., Expression of cathepsin B and cystatin C in human colorectal cancer. *Hum Pathol* **1999,** *30* (6), 680-686.

35. Saleh, Y.; Wnukiewicz, J.; Trziszka, T.; Siewinski, M.; Ziolkowski, P.; Kopec, W., Cathepsin B and cysteine protease inhibitors in human tongue cancer: Correlation with tumor staging and in vitro inhibition of cathepsin B by chicken cystatin. *J Cancer Molecules* **2006,** *2*, 67-72.

36. Smid, L.; Strojan, P.; Budihna, M.; Skrk, J.; Vrhovec, I.; Zargi, M.; Kos, J., Prognostic value of cathepsins B, D and stefins A and B in laryngeal carcinoma. *Eur Arch Oto-Rhino-L* **1997,** *254*, S150-S153.

37. Gondi, C. S.; Rao, J. S., Cathepsin B as a cancer target. *Expert Opin Ther Tar* **2013,** *17* (3), 281-291.

38. Tiziani, S.; Lopes, V.; Gunther, U. L., Early Stage Diagnosis of Oral Cancer Using H-1 NMR-Based Metabolomics. *Neoplasia* **2009,** *11* (3), 269-U69.

39. Poltavets, V.; Kochetkova, M.; Pitson, S. M.; Samuel, M. S., The Role of the Extracellular Matrix and Its Molecular and Cellular Regulators in Cancer Cell Plasticity. *Front Oncol* **2018,** *8*.

40. Hao, R. Z.; Wang, D. B.; Zhang, X. E.; Zuo, G. M.; Wei, H. P.; Yang, R. F.; Zhang, Z. P.; Cheng, Z. X.; Guo, Y. C.; Cui, Z. Q.; Zhou, Y. F., Rapid detection of Bacillus anthracis using monoclonal antibody functionalized QCM sensor. *Biosens Bioelectron* **2009,** *24* (5), 1330-1335.

41. Stair, J. L.; Watkinson, M.; Krause, S., Sensor materials for the detection of proteases. *Biosens Bioelectron* **2009,** *24* (7), 2113-2118.

42. Gorodkiewicz, E., Surface Plasmon Resonance Imaging Sensor for Cathepsin Determination Based on Immobilized Cystatin. *Protein Peptide Lett* **2009,** *16* (11), 1379-1385.

43. Gorodkiewicz, E.; Ostrowska, H.; Sankiewicz, A., SPR imaging biosensor for the 20S proteasome: sensor development and application to measurement of proteasomes in human blood plasma. *Microchim Acta* **2011,** *175* (1-2), 177-184.

44. Owen, V. M., Optical fluorescence biosensoring application and diversification - A case history. *Biosens Bioelectron* **1996,** *11* (1-2), R5-R8.

45. Zadran, S.; Standley, S.; Wong, K.; Otiniano, E.; Amighi, A.; Baudry, M., Fluorescence resonance energy transfer (FRET)-based biosensors: visualizing cellular dynamics and bioenergetics. *Appl Microbiol Biot* **2012,** *96* (4), 895-902.

46. Kajihara, D.; Abe, R.; Iijima, I.; Komiyama, C.; Sisido, M.; Hohsaka, T., FRET analysis of protein conformational change through position-specific incorporation of fluorescent amino acids. *Nat Methods* **2006,** *3* (11), 923-929.

47. Shi, J. Y.; Chan, C. Y.; Pang, Y. T.; Ye, W. W.; Tian, F.; Lyu, J.; Zhang, Y.; Yang, M., A fluorescence resonance energy transfer (FRET) biosensor based on graphene quantum dots (GQDs) and gold nanoparticles (AuNPs) for the detection of mecA gene sequence of Staphylococcus aureus. *Biosens Bioelectron* **2015,** *67*, 595-600.

48. Lovell, J. F.; Chen, J.; Jarvi, M. T.; Cao, W. G.; Allen, A. D.; Liu, Y.; Tidwell, T. T.; Wilson, B. C.; Zheng, G., FRET Quenching of Photosensitizer Singlet Oxygen Generation. *J Phys Chem B* **2009,** *113* (10), 3203-3211.

49. Engvall, E.; Perlmann, P., Enzyme-linked immunosorbent assay (ELISA). *Protides of the biological fluids* **1971**, 553-556.

50. Wang, Q. X.; Gao, F.; Ni, J. C.; Liao, X. L.; Zhang, X.; Lin, Z. Y., Facile construction of a highly sensitive DNA biosensor by in-situ assembly of electro-active tags on hairpin-structured probe fragment. *Sci Rep-Uk* **2016,** *6*.

51. Liu, G. D.; Wang, J.; Wunschel, D. S.; Lin, Y. H., Electrochemical proteolytic beacon for detection of matrix metalloproteinase activities. *Journal of the American Chemical Society* **2006,** *128* (38), 12382-12383.

52. Huang, Y.; Shi, M.; Hu, K.; Zhao, S. L.; Lu, X.; Chen, Z. F.; Chen, J.; Liang, H., Carbon nanotube-based multicolor fluorescent peptide probes for highly sensitive multiplex detection of cancer-related proteases. *J Mater Chem B* **2013,** *1* (28), 3470-3476.

53. Liao, Z. R.; Wang, J. F.; Zhang, P. J.; Zhang, Y.; Miao, Y. F.; Gao, S. M.; Deng, Y. L.; Geng, L. N., Recent advances in microfluidic chip integrated electronic biosensors for multiplexed detection. *Biosens Bioelectron* **2018,** *121*, 272-280.

54. Pursey, J. P.; Chen, Y.; Stulz, E.; Park, M. K.; Kongsuphol, P., Microfluidic electrochemical multiplex detection of bladder cancer DNA markers. *Sensor Actuat B-Chem* **2017,** *251*, 34-39.

55. Huang, J. S.; Liu, Y.; You, T. Y., Carbon nanofiber based electrochemical biosensors: A review. *Anal Methods-Uk* **2010,** *2* (3), 202-211.

56. Kim Y.A., H. T., Endo M., Dresselhaus M.S., *Carbon Nanofibers*. Springer: 2013.

57. Rawlings, N. D.; Barrett, A. J.; Bateman, A., Using the MEROPS Database for Proteolytic Enzymes and Their Inhibitors and Substrates. *Curr Protoc Bioinformatics* **2014,** *48*, 1 25 1-33.

58. Eatemadi, A.; Aiyelabegan, H. T.; Negahdari, B.; Mazlomi, M. A.; Daraee, H.; Daraee, N.; Eatemadi, R.; Sadroddiny, E., Role of protease and protease inhibitors in cancer pathogenesis and treatment. *Biomed Pharmacother* **2017,** *86*, 221-231.

59. Egeblad, M.; Werb, Z., New functions for the matrix metalloproteinases in cancer progression. *Nature Reviews Cancer* **2002,** *2* (3), 161-174.

60. Funovics, M.; Weissleder, R.; Tung, C. H., Protease sensors for bioimaging. *Anal Bioanal Chem* **2003,** *377* (6), 956-963.

61. Lenarcic, B.; Gabrijelcic, D.; Rozman, B.; Drobnic-Kosorok, M.; Turk, V., Human cathepsin B and cysteine proteinase inhibitors (CPIs) in inflammatory and metabolic joint diseases. *Biological Chemistry Hoppe-Seyler* **1988,** *369*, 257-261.

62. Ben-Nun, Y.; Merquiol, E.; Brandis, A.; Turk, B.; Scherz, A.; Blum, G., Photodynamic quenched cathepsin activity based probes for cancer detection and macrophage targeted therapy. *Theranostics* **2015,** *5* (8), 847.

63. Castillo, G.; Pribransky, K.; Mezo, G.; Kocsis, L.; Csampai, A.; Nemeth, K.; Keresztes, Z.; Hianik, T., Electrochemical and Photometric Detection of Plasmin by Specific Peptide Substrate. *Electroanal* **2015,** *27* (3), 789-798.

64. Yang, H.; Ji, J.; Liu, Y.; Kong, J. L.; Liu, B. H., An aptamer-based biosensor for sensitive thrombin detection. *Electrochem Commun* **2009,** *11* (1), 38-40.

65. Arrigan, D. W. M., Nanoelectrodes, nanoelectrode arrays and their applications. *Analyst* **2004,** *129* (12), 1157-1165.

66. Murray, R. W., Nanoelectrochemistry: Metal nanoparticles, nanoelectrodes, and nanopores. *Chem Rev* **2008,** *108* (7), 2688-2720.

67. Li, J.; Papadopoulos, C.; Xu, J. M.; Moskovits, M., Highly-ordered carbon nanotube arrays for electronics applications. *Appl Phys Lett* **1999,** *75* (3), 367-369.

68. Tang, X. W.; Bansaruntip, S.; Nakayama, N.; Yenilmez, E.; Chang, Y. L.; Wang, Q., Carbon nanotube DNA sensor and sensing mechanism. *Nano Lett* **2006,** *6* (8), 1632-1636.

69. Liu, J. Q.; Chou, A.; Rahmat, W.; Paddon-Row, M. N.; Gooding, J. J., Achieving direct electrical connection to glucose oxidase using aligned single walled carbon nanotube arrays. *Electroanal* **2005,** *17* (1), 38-46.

70. David-Pur, M.; Bareket-Keren, L.; Beit-Yaakov, G.; Raz-Prag, D.; Hanein, Y., All-carbon-nanotube flexible multi-electrode array for neuronal recording and stimulation. *Biomed Microdevices* **2014,** *16* (1), 43-53.

71. Wei, G.; Fujiki, K.; Saitoh, H.; Shirai, K.; Tsubokawa, N., Surface grafting of polyesters onto carbon nanofibers and electric properties of conductive composites prepared from polyester-grafted carbon nanofibers. *Polym J* **2004,** *36* (4), 316-322.

72. Zurawa-Janicka, D.; Jarzab, M.; Polit, A.; Skorko-Glonek, J.; Lesner, A.; Gitlin, A.; Gieldon, A.; Ciarkowski, J.; Glaza, P.; Lubomska, A.; Lipinska, B.,

Temperature-induced changes of HtrA2(Omi) protease activity and structure. *Cell Stress Chaperon* **2013,** *18* (1), 35-51.

73. Swisher, L. Z.; Syed, L. U.; Prior, A. M.; Madiyar, F. R.; Carlson, K. R.; Nguyen, T. A.; Hua, D. H.; Li, J., Electrochemical protease biosensor based on enhanced AC voltammetry using carbon nanofiber nanoelectrode arrays. *The Journal of Physical Chemistry C* **2013,** *117* (8), 4268-4277.

74. Monacell, J. T.; Carbone, I., Mobyle SNAP Workbench: a Web-based Analysis Portal for Population Genetics and Evolutionary Genomics. *Bioinformatics* **2014,** *30* (10), 1488-1490.

75. Lopez-Otin, C.; Bond, J. S., Proteases: Multifunctional Enzymes in Life and Disease. *J Biol Chem* **2008,** *283* (45), 30433-30437.

76. Martinelli, P.; Rugarli, E. I., Emerging roles of mitochondrial proteases in neurodegeneration. *Bba-Bioenergetics* **2010,** *1797* (1), 1-10.

77. Oesch, U.; Janata, J., Electrochemical study of gold electrodes with anodic oxide films - I. Formation and reduction behaviour of anodic oxides on gold. *Electrochimica Acta* **1983,** *28* (9), 1237-1246.

78. Oesch, U.; Janata, J., Electrochemical study of gold electrodes with anodic oxide films - II. Inhibition of electrochemical redox reactions by monolayers of surface oxides. *Electrochimica Acta* **1983,** *28* (9), 1247-1253.

79. Rodríguez-López, J.; Alpuche-Avilés, M. A.; Bard, A. J., Interrogation of Surfaces for the Quantification of Adsorbed Species on Electrodes: Oxygen on Gold and Platinum in Neutral Media. *Journal of the American Chemical Society* **2008,** *130* (50), 16985-16995.

80. Anderson, M. J.; Crooks, R. M., High-Efficiency Generation-Collection Microelectrochemical Platform for Interrogating Electroactive Thin Films. *Analytical Chemistry* **2014,** *86* (19), 9962-9969.

81. Gutiérrez, O. A.; Chavez, M.; Lissi, E., A Theoretical Approach to Some Analytical Properties of Heterogeneous Enzymatic Assays. *Analytical Chemistry* **2004,** *76* (9), 2664-2668.

82. Gutierrez, O. A.; Chavez, M.; Lissi, E., A theoretical approach to some analytical properties of heterogeneous enzymatic assays. *Analytical Chemistry* **2004,** *76* (9), 2664-2668.

83. Song, Y.; Fan, H. F.; Anderson, M. J.; Wright, J. G.; Hua, D. H.; Koehne, J.; Meyyappan, M.; Li, J., Electrochemical Activity Assay for Protease Analysis Using Carbon Nanofiber Nanoelectrode Arrays. *Analytical Chemistry* **2019,** *91* (6), 3971-3979.

84. González-Fernández, E.; Avlonitis, N.; Murray, A. F.; Mount, A. R.; Bradley, M., Methylene blue not ferrocene: Optimal reporters for electrochemical detection of protease activity. *Biosensors and Bioelectronics* **2016,** *84*, 82-88.

85. Kang, D.; Ricci, F.; White, R. J.; Plaxco, K. W., Survey of Redox-Active Moieties for Application in Multiplexed Electrochemical Biosensors. *Analytical Chemistry* **2016,** *88* (21), 10452-10458.

86. Gracias, K. S.; McKillip, J. L., A review of conventional detection and enumeration methods for pathogenic bacteria in food. *Can J Microbiol* **2004,** *50* (11), 883-890.

87. Zhang, H. Y.; Wang, S. O., Review on enzyme-linked immunosorbent assays for sulfonamide residues in edible animal products. *J Immunol Methods* **2009,** *350* (1-2), 1-13.

88. Chen, Q. Y.; Fei, J.; Wu, L. J.; Jiang, Z. Y.; Wu, Y. Q.; Zheng, Y.; Lu, G. H., Detection of cathepsin B, cathepsin L, cystatin C, urokinase plasminogen activator and urokinase plasminogen activator receptor in the sera of lung cancer patients. *Oncol Lett* **2011,** *2* (4), 693-699.

89. Wang, S. Q.; Zhao, X. H.; Khimji, I.; Akbas, R.; Qiu, W. L.; Edwards, D.; Cramer, D. W.; Ye, B.; Demirci, U., Integration of cell phone imaging with microchip ELISA to detect ovarian cancer HE4 biomarker in urine at the point-of-care. *Lab Chip* **2011,** *11* (20), 3411-3418.

Appendix A - Peptide Synthesis and Characterization

This part of work was accomplished by Dr. Duy. H. Hua's lab

The peptides were synthesized by solid-phase peptide synthesis method using a CEM Discover microwave synthesizer.

a. *Standard coupling procedure using microwave*

To 1.0 g of 2-chlorotrityl resin (1.0 eq) with free *N*-terminal amine was added a solution of Fmoc-amino acid (3.0 eq) and HBTU (2.7 eq) in dry DMF (16 mL) containing 4.2% diisopropylethylamine (DIPEA). The mixture was subjected to microwave irradiation (25W, 5 min, 75^{o}C) with stirring. The reaction mixture was filtered and washed with DMF five times (10 mL each).

b. *Standard deprotection procedure using microwave*

A solution of 20% piperidine in DMF (16 mL) was added to the N-Fmoc protected amino acid resin and subjected to microwave irradiation (25W, 3 min, 75^{o}C). The reaction mixture was filtered, and the resin was washed with DMF five times (10 ml each).

c. *Standard cleavage procedure using microwave*

The peptide attached 2-chlorotrityl resin was washed with dichloromethane (DCM) (20 mL) and then treated with 16 mL of cleavage solution containing 95% trifluoroacetic acid (TFA), 2.5% triisopropylsilane (TIPS), and 2.5% water. The mixture was irradiated in the microwave reactor (20W, 38^{o}C) for 18 min. The reaction mixture was filtered into a 100-mL flask and diluted with 60 mL of cold hexane:diethyl ether (1:1) to precipitate out the desired peptide. The solid peptide was collected by centrifugation (4000 rpm, 10 min, 4^{o}C) and washed three times with cold hexane:diethyl ether (1:1) to give the product peptide as a white solid.

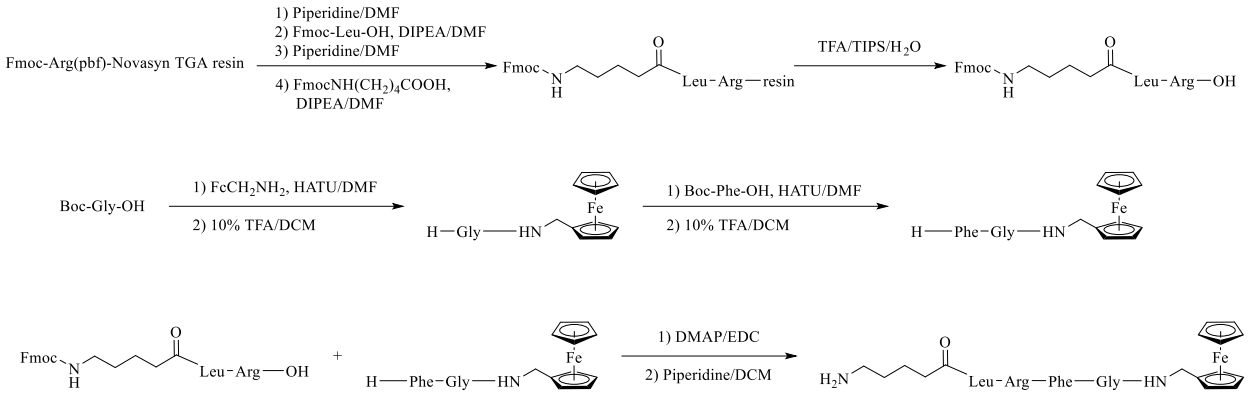

Figure A. 1 Synthesis of tetrapeptide (peptide #3 in Chapter 3) H_2N-$(CH_2)_4$CO-Leu-Arg-Phe-Gly-NH-CH_2-Fc for cathepsin B detection.

Starting with 0.3 g of Fmoc-Arg(pbf)-Novasyn TGA resin (0.23 mmol/g, 200 mesh), sequentially *N*-Fmoc protected leucine amino acid and Fmoc-$NH(CH_2)_4CO_2H$ were condensed using conventional solid-state peptide synthesis by coupling (*Standard coupling procedure*) and deprotection (*Standard deprotection procedure*) strategy in order of Leu and *N*-Boc-5-aminovaleric acid. *Standard cleavage procedure* was used to cleave and recover the peptide from the resin to give white solid Fmoc-HN-$(CH_2)_4$CO-Leu-Arg-OH **(**33.8 mg, 80.5%): ^{1}H NMR (400 MHz, CD_3OD) δ 8.37 (d, *J* = 8.0 Hz, 1H), 8.23 (d, *J* = 7.3 Hz, 1H), 7.79 (d, *J* = 7.5 Hz, 2H), 7.64 (d, *J* = 7.5 Hz, 2H), 7.38 (t, *J* = 7.4 Hz, 2H), 7.30 (td, *J* = 7.5, 1.2 Hz, 2H), 4.40 (ddd, *J* = 16.9, 9.3, 5.1 Hz, 1H), 4.33 (d, *J* = 6.9 Hz, 2H), 4.19 (d, *J* = 6.8 Hz, 1H), 3.73 – 3.53 (m, 7H), 3.14 (dt, *J* = 22.2, 6.6 Hz, 4H), 2.28 (s, 1H), 2.02 – 1.20 (m, 7H), 0.94 (dd, *J* = 15.8, 6.5 Hz, 6H) ppm. ^{13}C NMR (100 MHz, CD_3OD) δ 175.0, 174.1, 173.7, 157.7, 157.4, 144.1, 141.4, 127.6, 127.0, 125.0, 119.8, 70.4, 66.4, 52.2, 51.8, 40.7, 40.5, 40.1, 35.0, 29.2, 28.6, 25.1, 24.7, 22.9, 22.3, 20.8 ppm.

d. ***Synthesis of Boc-Gly-NHCH$_2$-Fc.***

HATU (0.24 g, 0.63 mmol) was added to a solution of Boc-Gly-OH (0.10 g, 0.57 mmol) in dry DMF under argon and the resulting solution was stirred at 25^{o}C for 30 minutes. NH_2CH_2-

Fc (0.14 g, 0.63 mmol) was added to the solution followed by stirring at 25°C for 12 hours. The solvent, DMF, of the crude reaction solution was removed by evaporation under reduced pressure (from a rotary evaporator connected to a vacuum pump), and the residue was chromatographed on silica gel using a mixture of ethyl acetate and hexane (1:2) to give 0.13 g (62% yield) of pure product as a colorless oil. ^{1}H NMR (400 MHz, $CDCl_3$) δ 6.41 (s, 1H), 5.19 (d, *J* = 8.0 Hz, 1H), 4.17 (d, *J* = 2.6 Hz, 6H), 4.14 (s, 3H), 4.13 (s, 1H), 3.80 (d, *J* = 6.0 Hz, 2H), 1.44 (s, 9H) ppm.

e. ***Synthesis of Boc-Phe-Gly-NHCH$_2$-Fc.***

A solution of Boc-Gly-NHCH$_2$-Fc (0.12 g, 0.32 mmol) in 5 mL of 10% TFA and dichloromethane was stirred under argon for 1 hour at 25°C. The resulting solution was gently concentrated on a rotary evaporator and placed under high vacuum for 1 hour to give H-Gly-NHCH$_2$Fc as a green solid. The material was used in the next experiment without purification. A solution of Boc-Phe-OH (86 mg, 0.32 mmol), EDC (0.10 g, 0.65 mmol) and DMAP (0.16 g, 0.12 mmol) in 2 mL of dry DMF under argon was stirred for 30 minute at 25°C. H-Gly-NHCH$_2$-Fc (obtained from the aforementioned experiment) in 1 mL of DMF was added to this solution, and it was stirred at 25°C for 12 hours. The reaction solution was diluted with 20 mL of dichloromethane and 20 mL of deionized water followed by aqueous 2N hydrochloric acid until pH = 2. The organic layer was separated using a separation funnel, and the aqueous layer was extracted four times (20 mL each) with dichloromethane. The combined organic layers were washed with brine, dried (anhydrous Na_2SO_4), filtered, concentrated, and column chromatographed on silica gel using a mixture of dichloromethane and methanol (15:1) as an eluent to give Boc-Phe-Gly-NHCH$_2$-Fc as a yellow oil (0.14 g, 81% yield). ^{1}H NMR (400 MHz, $CDCl_3$) δ 7.98 (s, 1H), 7.32 – 7.21 (m, 2H), 7.20 – 7.14 (m, 5H), 6.75 (d, *J* = 32.6 Hz, 2H), 5.09

(d, *J* = 7.1 Hz, 1H), 4.32 (d, *J* = 7.0 Hz, 1H), 4.23 – 4.11 (m, 6H), 4.11 – 4.07 (m, 3H), 3.85 (dd, *J* = 18.5, 5.7 Hz, 1H), 3.10 (dd, *J* = 13.8, 6.3 Hz, 1H), 2.99 (t, *J* = 6.7 Hz, 1H), 1.37 (s, 9H) ppm.

f. ***Synthesis of Fmoc-HN-$(CH_2)_4$CO-Leu-Arg-Phe-Gly-NH-CH_2-Fc.***

A solution of Boc-Phe-Gly-NHCH$_2$-Fc (25 mg, 0.048 mmol) in 5 mL 10% TFA in dichloromethane was stirred at 25^{o}C for 1 hour. The reaction solution was gently concentrated on a rotary evaporator and placed under high vacuum for 1 hour to give H-Phe-Gly-NHCH$_2$-Fc as a green solid. A solution of Fmoc-HN-$(CH_2)_4$CO-Leu-Arg-OH (28 mg, 0.046 mmol), EDC (15 mg, 0.092 mmol) and DMAP (17 mg, 0.14 mmol) in 2 mL of dry DMF under argon was stirred for 30 minute at 25^{o}C. A solution of H-Phe-Gly-NHCH$_2$-Fc in 1 mL DMF was added to the above, and the solution was stirred at 25^{o}C for 12 hours. The resulting solution was concentrated by removing DMF under reduced pressure (using a rotary evaporator connected to a vacuum pump) at 35^{o}C and column chromatographed on silica gel using a mixture of dichloromethane and methanol (15:1) as an eluent to give 16 mg (34% yield) of the titled product as a pale-yellow oil. ^{1}H NMR (400 MHz, $CDCl_3$) δ 7.74 (d, *J* = 7.5 Hz, 2H), 7.56 (d, *J* = 7.5 Hz, 1H), 7.38 (t, *J* = 7.4 Hz, 2H), 7.29 (d, *J* = 8.2 Hz, 1H), 7.15 (s, 5H), 4.33 (s, 3H), 4.11 (d, *J* = 44.5 Hz, 14H), 3.47 (s, 2H), 3.18 – 2.76 (m, 6H), 2.31 (d, *J* = 18.8 Hz, 2H), 1.43 (d, *J* = 145.0 Hz, 14H), 0.89 (dd, *J* = 19.7, 5.3 Hz, 6H) ppm.

g. ***Synthesis of H_2N-$(CH_2)_4$CO-Leu-Arg-Phe-Gly-NH-CH_2-Fc (peptide #3 in chapter 3).***

A solution of Fmoc-HN-$(CH_2)_4$CO-Leu-Arg-Phe-Gly-NH-CH_2-Fc (15 mg) in 3 mL of 20% piperidine-DMF and stirred at 25^{o}C for 12 hour. HPLC analysis of an aliquot from the reaction solution showed the absence of starting material. The reaction solution was concentrated gently on a rotary evaporator and purified using preparative HPLC with a gradient mixture of water and methanol as eluent. The fractions containing the desired product were combined and lyophilized to give H_2N-$(CH_2)_4$CO-Leu-Arg-Phe-Gly-NH-CH_2-Fc as a green solid (8 mg, 86%). ^{1}H NMR (400

MHz, DMSO-d_6) δ 8.56 – 8.24 (m, 2H), 8.05 (td, J = 21.8, 20.5, 8.7 Hz, 4H), 7.72 (d, J = 18.6 Hz, 4H), 7.34 – 7.08 (m, 5H), 4.50 (s, 4H), 4.40 – 4.02 (m, 10H), 3.03 (d, J = 8.7 Hz, 4H), 2.84 – 2.69 (m, 2H), 1.88 – 1.77 (m, 1H), 1.68 – 1.34 (m, 4H), 1.24 (s, 3H), 0.84 (ddd, J = 23.2, 6.6, 3.6 Hz, 6H) ppm. HRMS calcd for $C_{39}H_{58}FeN_9O_5$ $(M+H)^+$ $(M+H)^+$ 788.3905, found 788.4052.

h. Experimental procedures for the synthesis of hexapeptide (peptide #4 in chapter 3) H_2N-$(CH_2)_4$CO-Pro-Leu-Arg-Phe-Gly-Ala-NH-CH_2-Fc (Figure A.2) for cathepsin B detection.

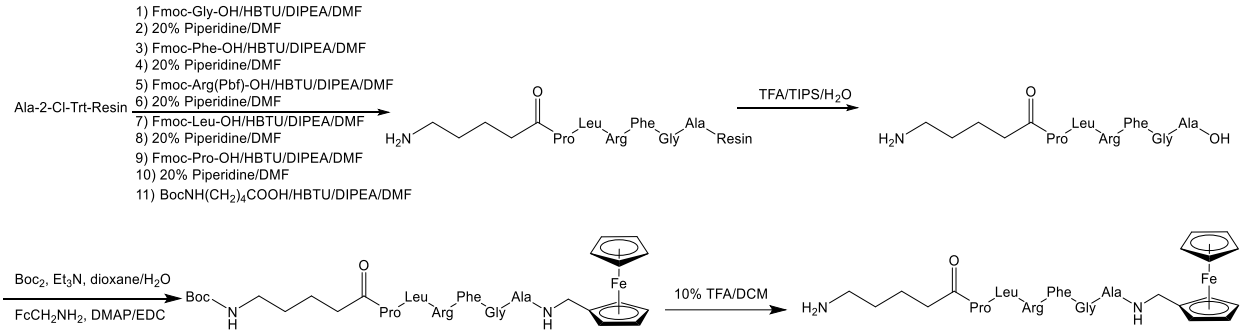

Figure A. 2 Synthesis of hexapeptide (peptide #4 in chapter 3) H_2N-$(CH_2)_4$CO-Pro-Leu-Arg-Phe-Gly-Ala-NH-CH_2-Fc for cathepsin B detection.

1) Synthesis of H_2N-$(CH_2)_4$CO-Pro-Leu-Arg-Phe-Gly-Ala-OH.

Starting with 1.0 g of alanine 2-chlorotrityl resin (0.59 mmol/g; 200 mesh), *N*-Fmoc protected amino acids were coupled using conventional solid-phase peptide synthesis by coupling (Standard coupling procedure) and deprotection (Standard deprotection procedure) strategy in order of Gly, Phe, Arg, Leu, Pro and *N*-Boc-5-aminovaleric acid. Standard cleavage procedure was used to cleave the peptide from the resin to give H_2N-$(CH_2)_4$CO-Pro-Leu-Arg-Phe-Gly-Ala-OH as a white solid (0.29 g, 64%). ^{1}H NMR (400 MHz, Methanol-d_4) δ 7.41 – 7.13 (m, 5H), 4.61 – 4.22 (m, 5H), 4.02 – 3.88 (m, 1H), 3.77 – 3.51 (m, 1H), 3.15 (dt, J = 18.6, 7.7 Hz, 3H), 3.03 – 2.87 (m, 4H), 2.45 (d, J = 6.6 Hz, 1H), 2.22 (td, J = 6.0, 2.6 Hz, 0H), 1.98 (dt, J = 13.1, 4.8 Hz, 2H), 1.67 (ttd, J = 13.4, 10.0, 5.8 Hz, 11H), 1.53 (ddd, J = 14.5, 10.4, 6.1 Hz, 3H), 1.41 (d, J = 7.3

Hz, 3H), 0.99 – 0.75 (m, 6H) ppm. HRMS calcd for $C_{16}H_{30}N_5O_6$ $(M+H)^+$ 759.4512, found 759.4687.

2) *Synthesis of Boc-HN-$(CH_2)_4$CO-Pro-Leu-Arg-Phe-Gly-Ala-OH.*

Triethylamine (35 μL, 2x mmol) was added to a solution of H_2N-$(CH_2)_4$CO-Pro-Leu-Arg-Phe-Gly-Ala-OH (73 mg, x mmol) in 10 mL of dioxane:water (1:1) under argon. After stirring the solution for 10 min at 25°C, di-*t*-butyl dicarbonate (Boc_2O) (37 mg, 2x mmol) was added and stirred for 12 hours. The reaction solution was concentrated under high vacuum for 5 hours to yield Boc-HN-$(CH_2)_4$CO-Pro-Leu-Arg-Phe-Gly-Ala-OH as a white solid (82 mg, 99% yield).

3) *Synthesis of Boc-HN-$(CH_2)_4$CO-Pro-Leu-Arg-Phe-Gly-Ala-NH-CH_2-Fc.*

DMAP (31 mg, 0.25 mmol) and EDC (26 mg, 0.25 mmol) were added to a solution of Boc-HN-$(CH_2)_4$CO-Pro-Leu-Arg-Phe-Gly-Ala-OH (82 mg, 0.084 mmol) in 2 mL of DMF and the solution was stirred at 25°C for 30 min. A solution of aminomethylferrocene (20 mg, 0.092 mmol) in 1 mL of DMF was added to this and the reaction mixture was stirred for 12 hours (the reaction was completed based on HPLC analysis of an aliquot), filtered and purified using a preparative HPLC (a gradient mixture of water and methanol was used as eluent). The fractions containing the desired product were combined and lyophilized to yield Boc-HN-$(CH_2)_4$CO-Pro-Leu-Arg-Phe-Gly-Ala-NH-CH_2-Fc as a yellow solid (68 mg, 67% Yield). ^{1}H NMR (400 MHz, Chloroform-*d*) δ 8.41 (s, 2H), 7.80 (s, 1H), 7.67 (s, 3H), 7.58 (s, 4H), 7.24 – 7.19 (m, 11H), 4.41 – 3.80 (m, 10H), 3.70 (s, 7H), 3.07 (d, *J* = 24.5 Hz, 8H), 2.70 (s, 50H), 1.45 (s, 7H), 1.42 (s, 18H), 1.25 (s, 5H), 1.00 – 0.89 (m, 5H), 0.76 (dd, *J* = 22.3, 5.6 Hz, 6H) ppm.

4) *Synthesis of H_2N-$(CH_2)_4$CO-Pro-Leu-Arg-Phe-Gly-Ala-NH-CH_2-Fc (peptide #4 in chapter 3).*

A solution of Boc-HN-$(CH_2)_4$CO-Pro-Leu-Arg-Phe-Gly-Ala-NH-CH_2-Fc (68 mg) in 10% TFA-dichloromethane was stirred at 25°C for 1 hour, and the absence of the starting material was

found from HPLC analysis of a reaction aliquot. The reaction solution was concentrated gently on a rotary evaporator and the residue was dissolved in deionized water (2 mL) and lyophilized on a lyophilizer to give H_2N-$(CH_2)_4$CO-Pro-Leu-Arg-Phe-Gly-Ala-NH-CH_2-Fc as a green solid. ^{1}H NMR (400 MHz, DMSO-d_6) δ 8.48 – 8.26 (m, 2H), 8.05 (td, J = 21.8, 20.5, 8.7 Hz, 6H), 7.72 (d, J = 18.6 Hz, 5H), 7.23 (d, J = 6.0 Hz, 6H), 4.32 – 4.03 (m, 12H), 3.03 (d, J = 8.7 Hz, 5H), 2.90 – 2.71 (m, 3H), 1.70 – 1.31 (m, 5H), 1.24 (s, 4H), 0.96 – 0.74 (m, 6H) ppm. HRMS calcd for $C_{47}H_{70}FeN_{11}O_7$ $(M+H)^+$ 956.4804, found 956.4904.

i. Experimental procedures for the synthesis of octapeptide (peptide #5 in chapter 3) H_2N-$(CH_2)_4$CO-Ala-Pro-Leu-Arg-Phe-Gly-Ala-Ala-NH-CH_2-Fc for cathepsin B detection (Figure A.3).

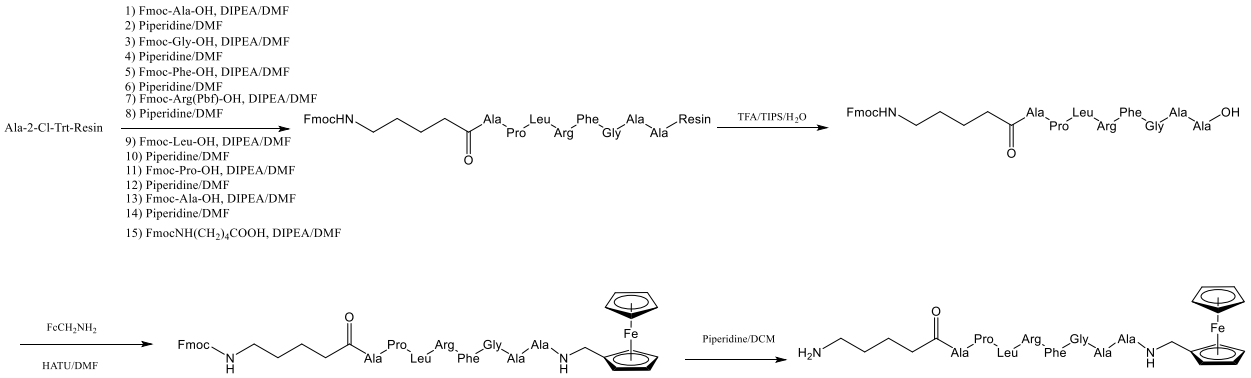

Figure A. 3 Synthesis of octapeptide (peptide #5 in chapter 3) H_2N-$(CH_2)_4$CO-Ala-Pro-Leu-Arg-Phe-Gly-Ala-Ala-NH-CH_2-Fc for cathepsin B detection.

1) Synthesis of Fmoc-HN-$(CH_2)_4$CO-Ala-Pro-Leu-Arg-Phe-Gly-Ala-Ala-OH.

Starting with 1.0 g of alanine 2-chlorotrityl resin (0.45 mmol/g, 200 mesh), *N*-Fmoc protected amino acids were coupled using conventional solid-phase peptide synthesis by coupling (Standard coupling procedure) and deprotection (Standard deprotection procedure) strategy in order of Ala, Gly, Phe, Arg, Leu, Pro, Ala and N-Fmoc-5-aminovaleric acid. Standard cleavage

procedure was used to cleave the peptide from the resin to give Fmoc-HN-$(CH_2)_4$CO-Ala-Pro-Leu-Arg-Phe-Gly-Ala-Ala-OH as a white solid (0.15 g, 30% yield). ^{1}H NMR (400 MHz, DMSO-d_6) δ 8.35 – 8.20 (m, 2H), 8.00 (q, *J* = 8.0, 7.4 Hz, 3H), 7.90 (t, *J* = 8.9 Hz, 3H), 7.81 – 7.62 (m, 4H), 7.42 (q, *J* = 7.6, 6.6 Hz, 3H), 7.32 (t, *J* = 7.4 Hz, 2H), 7.23 (d, *J* = 4.6 Hz, 4H), 4.50 (dt, *J* = 8.3, 4.2 Hz, 1H), 4.25 (ddt, *J* = 39.0, 14.0, 7.3 Hz, 9H), 3.11 – 2.92 (m, 4H), 2.80 (dd, *J* = 14.0, 9.2 Hz, 1H), 2.00 (dd, *J* = 11.7, 7.2 Hz, 1H), 1.83 (dt, *J* = 13.2, 6.4 Hz, 2H), 1.66 – 1.55 (m, 2H), 1.41 (dq, *J* = 14.4, 6.9 Hz, 5H), 1.32 – 1.15 (m, 9H), 0.83 (dd, *J* = 20.5, 6.5 Hz, 6H) ppm.

2) Synthesis of Fmoc-HN-$(CH_2)_4$CO-Ala-Pro-Leu-Arg-Phe-Gly-Ala-Ala-NH-CH_2-Fc.

HATU (22 mg, 1.3x mmol) was added to a solution of Fmoc-HN-$(CH_2)_4$CO-Pro-Leu-Arg-Phe-Gly-Ala-OH (50 mg, x mmol) in 2 mL of DMF under argon and the solution was stirred at 25°C for 30 min. Aminomethylferrocene (13 mg, 1.3x mmol) in 1 mL of DMF was added to the above and the solution was stirred for 12 hours (the progress of the reaction was checked by HPLC analysis of an aliquot from the reaction mixture), filtered, and purified using preparative HPLC. The fractions containing the desired product were combined and lyophilized to yield Fmoc-HN-$(CH_2)_4$CO-Ala-Pro-Leu-Arg-Phe-Gly-Ala-Ala-NH-CH_2-Fc as a yellow solid (32 mg, 64% yield). ^{1}H NMR (400 MHz, Chloroform-*d*) δ 8.61 (d, *J* = 4.6 Hz, 2H), 8.39 (d, *J* = 8.3 Hz, 2H), 8.23 – 8.05 (m, 1H), 7.60 (d, *J* = 7.5 Hz, 1H), 7.48 (t, *J* = 7.7 Hz, 1H), 7.42 (dd, *J* = 8.4, 4.6 Hz, 1H), 5.30 (s, 1H), 4.19 (s, 7H), 4.52 – 3.84 (m, 14H), 3.49 (s, 1H), 2.96 (s, 2H), 2.79 (s, 8H), 1.77 – 1.65 (m, 1H), 1.25 (s, 31H), 0.87 (q, *J* = 8.1, 7.2 Hz, 3H) ppm.

3) Synthesis of H_2N-$(CH_2)_4$CO-Ala-Pro-Leu-Arg-Phe-Gly-Ala-Ala-NH-CH_2-Fc (peptide #5 in chapter 3).

A solution of Fmoc-HN-$(CH_2)_4$CO-Ala-Pro-Leu-Arg-Phe-Gly-Ala-Ala-NH-CH_2-Fc (30 mg, x mmol) in x mL of 20% piperidine-DMF was stirred at 25°C for 30 hour and the progress of

the reaction was followed by HPLC analysis of an aliquot from the reaction solution. The reaction solution was concentrated gently on a rotary evaporator and purified using preparative HPLC. The fractions containing the desired product were combined and lyophilized to give H_2N-$(CH_2)_4$CO-Ala-Pro-Leu-Arg-Phe-Gly-Ala-Ala-NH-CH_2-Fc as a pale green solid (12 mg, 48% yield). ^{1}H NMR (400 MHz, Acetone-d_6) δ 7.29 (s, 4H), 5.35 (d, J = 4.8 Hz, 0H), 4.58 – 4.14 (m, 3H), 3.76 (s, 4H), 3.56 (q, J = 7.0 Hz, 1H), 2.09 (s, 5H), 1.50 – 1.21 (m, 198H), 1.11 (s, 1H), 1.02 – 0.80 (m, 6H) ppm. HRMS calcd for $C_{47}H_{70}FeN_{11}O_7$ $(M+H)^+$ 1098.5551, found 1098.5497.

j. Experimental procedures for the synthesis of Hexapeptide (peptide #2 in chapter 4) H_2N-$(CH_2)_4$CO-Pro-Leu-Ala-Phe-Val-Ala-NH-CH_2-Fc and Hexapeptide (peptide #2 in chapter 4) H_2N-$(CH_2)_4$CO-Pro-Leu-Ala-Gly-Val-Ala-NH-CH_2-Fc for cathepsin B detection (Figure A.4).

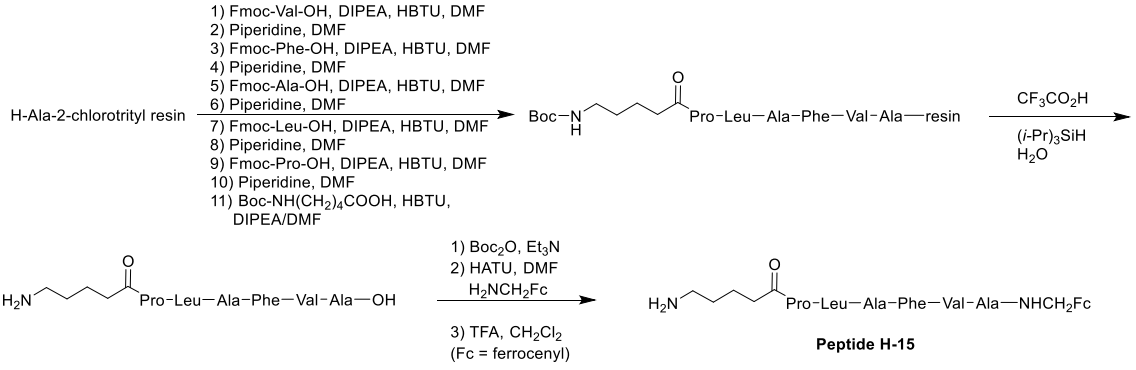

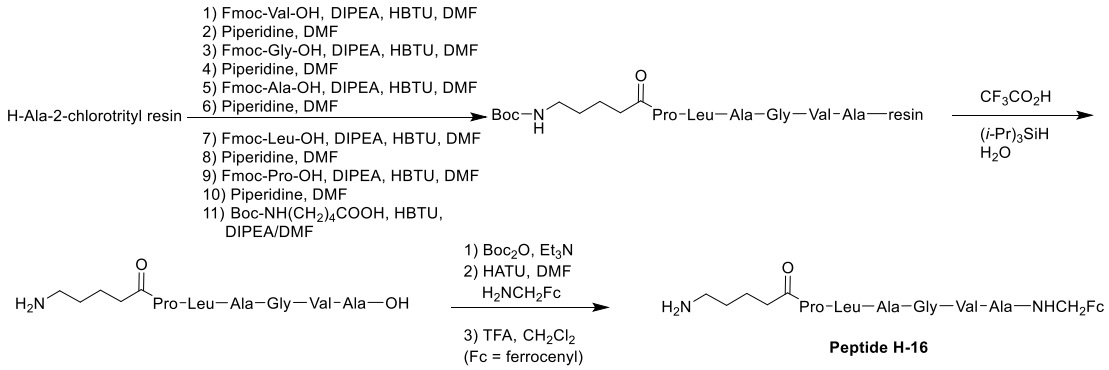

Figure A. 4 Synthesis of Hexapeptide peptide #2 (in chapter 4), H_2N-$(CH_2)_4$CO-Pro-Leu-Ala-Phe-Val-Ala-NH-CH_2-Fc, and Hexapeptide peptide #1 (in chapter 4), H_2N-$(CH_2)_4$CO-Pro-Leu-Ala-Gly-Val-Ala-NH-CH_2-Fc.

Preparation of peptide #2 in chapter 4:

Starting from 1.0 g (0.45 mmol) of H-Ala-2-chlorotrityl resin (200 mesh), the following reaction sequence was carried out: (i) coupling with *N*-Fmoc-Val-OH (1.35 mmol) and HBTU (2.7 equiv., for all amino acid coupling steps); (ii) deprotection of Fmoc group with piperidine in DMF; (iii) coupling with *N*-Fmoc-Phe-OH (1.35 mmol); (iv) deprotection with piperidine/DMF; (v) coupling with *N*-Fmoc-Ala-OH (1.35 mmol); (vi) deprotection with piperidine/DMF; (vii) coupling with *N*-Fmoc-Leu-OH (1.35 mmol); (viii) deprotection with piperidine/DMF; (ix) coupling with *N*-Fmoc-Pro-OH (1.35 mmol); (x) deprotection with piperidine/DMF; (xi) coupling with *N*-(*tert*-butoxycarbonyl)-$NH(CH_2)_4CO_2H$ [or *N*-Boc-$NH(CH_2)_4CO_2H$] (1.35 mmol) with HBTU (2 equiv.); and (xii) cleavage of the peptide from resin with TFA and $(i\text{-Pr})_3SiH$ in water. The peptide was then precipitated out using a mixture of hexane and diethyl ether, and dried to yield 310 mg of $H_2N(CH_2)_4$CO-Pro-Leu-Ala-Phe-Val-Ala-OH. This material was used in the subsequent reaction without further purification.

To a solution of 0.14 g (0.20 mmol) of $H_2N(CH_2)_4$CO-Pro-Leu-Ala-Phe-Val-Ala-OH in 10 ml of *p*-dioxane and water (1:1) were added 75 µl (0.60 mmol) of triethylamine and 0.128 g (0.60 mmol) of di-*tert*-butyl dicarbonate (Boc_2O). The solution was stirred at room temperature for 12 h, and additional 50 µl of triethylamine and 95 mg of Boc_2O were added. It was stirred for 8 h and HPLC-MS analysis of an aliquot of the solution showed the absence of starting material peptide and only the presence of desired peptide. The solution was concentrated under reduced

pressure for 3 h to give the Boc protected crude product, which was used without purification in the following reaction. To the aforementioned *N*-Boc-HN(CH_2)$_4$CO-Pro-Leu-Ala-Phe-Val-Ala-OH and 0.11 g (0.28 mmol) of 1-[bis(dimethylamino)methylene]-1*H*-1,2,3-triazolo[4,5-*b*]pyridinium 3-oxide hexafluorophosphate (HATU) in 1 ml of DMF was added a solution of 60 mg (0.24 mmol) of 1-(aminomethyl)ferrocene•HCl salt in 1 ml of DMF. The solution was stirred at 25 ^{o}C for 12 h and an aliquot was analyzed by HPLC showing the absence of starting peptide. The reaction mixture was filtered through a Chromafil Xtra PTFE-20/25 syringe filter (0.20 µm) and the filtrate was purified by preparative HPLC using water and acetonitrile (1:1; 10 ml/min) as the running solvent to give 0.10 g of *N*-Boc-HN(CH_2)$_4$CO-Pro-Leu-Ala-Phe-Val-Ala-NHCH$_2$-Fc (Fc = ferrocenyl). MS (ESI; positive mode): *m/z* calculated for $C_{52}H_{77}FeN_8O_9$ $(M+H)^+$: 1013.51, found 1013.37 (100%).

Peptide #2 (in chapter 4): $H_2N(CH_2)_4$CO-Pro-Leu-Ala-Phe-Val-Ala-NHCH$_2$-Fc. To a solution of 0.10 g of *N*-Boc-HN(CH_2)$_4$CO-Pro-Leu-Ala-Phe-Val-Ala-NHCH$_2$-Fc in 10 ml of dichloromethane was added 1 ml of TFA, and the solution was stirred at 25 ^{o}C for 30 min. An aliquot was removed and analyzed by TLC, showing the absence of the starting peptide. The reaction mixture was diluted with 15 ml of water and concentrated on a rotary evaporator to remove most of the dichloromethane and TFA, leaving a mixture of solid and liquid. The yellow solid was collected by filtration to give 85 mg (86% yield) of **peptide #2 (in chapter 4)**. MS (ESI; positive mode): *m/z* calculated for $C_{47}H_{69}FeN_8O_7$ $(M+H)^+$: 913.46, found 913.34 (100%). ^{1}H NMR (400 MHz, DMSO-D_6) δ 8.2 – 7.5 (a series of m, 6H, NHC=O), 7.25 – 5.15 (m, 5H, Ar), 4.6 – 4.48 (m, 1H), 4.48 – 4.24 (m, 2H, NCH$_2$-Fc), 4.15 (s, 5H, Cp ring of Fc), 4.07 (s, 2H, Cp ring of Fc), 4.02 – 3.95 (m, 2H, Cp ring of Fc), 3.10 – 2.95 (m, 1H), 2.75 – 1.27 (a series of m), 1.23 (d, *J* = 7 Hz, 3H, Me), 1.15 (d, *J* = 7 Hz, 3H, Me), 0.80 – 0.75 (a series of 4 d, 12H, 4 Me's

of 2 isopropyl groups) ppm. ^{13}C NMR (100 MHz, DMSO-D_6) δ 172.4, 171.9, 171.2, 171.0, 170.7, 138.1, 129.7 (2C), 128.5 (2C), 126.7, 68.9 (Cp's Cs of ferrocene), 67.8 (Cp's Cs of ferrocene), 59.8, 57.9, 51.4, 48.5, 47.3, 37.9, 33.5, 31.2, 29.8, 27.2, 24.6, 23.6, 22.7, 21.9, 21.4, 19.7, 18.9, 18.5 ppm.

Preparation of peptide #1 in chapter 4:

Starting from 1.0 g (0.45 mmol) of H-Ala-2-chlorotrityl resin (200 mesh), the following reaction sequence was carried out: (i) coupling with *N*-Fmoc-Val-OH (1.35 mmol) and HBTU (2.7 equiv., for all amino acid coupling steps);; (ii) deprotection of Fmoc group with piperidine in DMF; (iii) coupling with *N*-Fmoc-Gly-OH (1.35 mmol); (iv) deprotection with piperidine/DMF; (v) coupling with *N*-Fmoc-Ala-OH (1.35 mmol); (vi) deprotection with piperidine/DMF; (vii) coupling with *N*-Fmoc-Leu-OH (1.35 mmol); (viii) deprotection with piperidine/DMF; (ix) coupling with *N*-Fmoc-Pro-OH (1.35 mmol); (x) deprotection with piperidine/DMF; (xi) coupling with *N*-Fmoc-$NH(CH_2)_4CO_2H$ (1.35 mmol); and (xii) cleavage of the peptide from resin with TFA and (*i*-Pr)$_3$SiH in water. After precipitation of the peptide using a mixture of hexane and diethyl ether and drying, 164 mg of $H_2N(CH_2)_4$CO-Pro-Leu-Ala-Gly-Val-Ala-OH was obtained. This material was used in the subsequent reaction without further purification.

To a solution of 0.83 g (0.13 mmol) of $H_2N(CH_2)_4$CO-Pro-Leu-Ala-Gly-Val-Ala-OH in 10 ml of *p*-dioxane and water (1:1) were added 52 μl (0.40 mmol) of triethylamine and 0.087 g (0.40 mmol) of di-*tert*-butyl dicarbonate (Boc_2O). The solution was stirred at room temperature for 12 h, and additional 40 μl of triethylamine and 45 mg of Boc_2O were added. It was stirred for 8 h and HPLC-MS analysis of an aliquot of the reaction solution showed the absence of the starting amine. The reaction solution was concentrated under reduced pressure for 3 h to give the Boc protected crude product. It was used in the following step without purification. To the

aforementioned *N*-Boc-HN$(CH_2)_4$CO-Pro-Leu-Ala-Gly-Val-Ala-OH and 66 mg (0.17 mmol) of HATU in 1 ml of DMF was added a solution of 37 mg (0.15 mmol) of 1-(aminomethyl)ferrocene•HCl salt in 1 ml of DMF. The solution was stirred at 25ºC for 12 h and an aliquot was analyzed by HPLC showing the absence of the starting peptide. The reaction mixture was filtered through a Chromafil® Xtra PTFE-20/25 syringe filter (0.20 μm) and the filtrate was purified by preparative HPLC using water and acetonitrile (1:1; 10 ml/min) as the running solvent to give *N*-Boc-HN$(CH_2)_4$CO-Pro-Leu-Ala-Gly-Val-Ala-NHCH$_2$-Fc (Fc = ferrocenyl).

Peptide #1 (in chapter 4): $H_2N(CH_2)_4$CO-Pro-Leu-Ala-Gly-Val-Ala-NHCH$_2$-Fc. To a solution of 40 mg of N-Boc-HN$(CH_2)_4$CO-Pro-Leu-Ala-Gly-Val-Ala-NHCH$_2$-Fc in 5 ml of dichloromethane was added 0.5 ml of TFA, and the solution was stirred at 25 ºC for 30 min. An aliquot was removed and analyzed by TLC, showing the absence of the starting peptide. The reaction mixture was diluted with 10 ml of deionized water and concentrated on a rotary evaporator to remove most of the dichloromethane and TFA. The resulting solution was diluted with deionized water and lyophilized on a freeze-dry instrument to give 30 mg of peptide #1 (in chapter 4). MS (ESI; positive mode): m/z calcd for $C_{40}H_{63}FeN_8O_7$ $(M+H)^+$: 823.409, found 823.303 (100%). ^{1}H NMR (400 MHz, D2O) δ 4.4 – 4.25 (m, 9H, Cp's Hs of Fc), 3.91 (s, 1H), 3.84 – 3.82 (m, 1H), 3.66 – 3.58 (m, 2H), 3.04 – 2.93 (m, 6H), 2.50 – 2.44 (m, 2H), 2.10 – 1.80 (m, 4H), 1.78 – 1.56 (m, 10H), 1.47 (d, J = 8 Hz, 2H), 1.39 (d, J = 8 Hz, 2H), 1.02 – 0.75 (a series of d, 18H) ppm. 13C NMR (100 MHz, D2O) δ 174.7 (3C), 174.5 (4C), 60.1 (Cp's Cs of ferrocene, 5C), 58.6 (Cp's Cs of ferrocene, 5C), 54.0, 52.2, 49.7, 48.0, 42.1, 39.5, 39.1 (2C), 38.2, 33.2, 29.6, 26.3, 24.4 (2C), 22.1, 21.0, 20.6, 18.2, 18.1, 17.6, 17.4, 17.3, 16.5 ppm.

Appendix B - Peptide Used in Chapter 4 Cleavage Position Investigation

This part of work was accomplished by Dr. Duy. H. Hua's lab

The cleavage sites of the hexapeptide-Fc substrates were examined using HPLC as shown in Figures A.5 and A.6. Analytical HPLC was performed with a Shimadzu SCL-10A HPLC system fitted with a proto 300 C18 reverse phase semi-prep column (10 μm, 250 × 10 mm). The flow rate was 1 ml/min with a gradient elution starting from 100% solvent A (water containing 0.1% TFA) to 20% solvent A and 80% solvent B (acetonitrile containing 0.1% TFA) over 50 min. The UV absorbance was monitored at 254 nm. Figure A.5 shows the HPLC chromatogram of peptide #2 (chapter 4), H_2N-$(CH_2)_4$CO-Pro-Leu-Ala-Phe-Val-Ala-NH-CH_2-Fc in 50 mM MES (pH 5.0) and 250 mM NaCl. The hexapeptide appeared at 35.9 min in the chromatogram (Figure A.5a) and its structure was verified by mass spectrometry analysis. Figures A.5b and A.5c showed the chromatograms after peptide #2 (chapter 4) was treated with cathepsin B for 2 h and 3 h, respectively. The cleavage product, Ala-Phe-Val-Ala-NHCH_2-Fc (mass of 603.5 + 23 of sodium$^+$ = 626.5) appeared at 16.0 min in the chromatogram and its structure was verified by MS analysis. A mass of 626.2 was found from the peak at 16.0 min.

Figure A.6a shows the HPLC chromatogram of 6.5 mM peptide #1 (chapter 4), H_2N-$(CH_2)_4$CO-Pro-Leu-Ala-Gly-Val-Ala-NH-CH_2-Fc, in 50 mM MES (pH 5.0) and 250 mM NaCl, and Figures A.6b and A.6c show chromatograms obtained after peptide #1 (chapter 4) was incubated with 5.75 ng/μL (0.17 μM) cathepsin B for 2 h and 3 h, respectively. The absorbance peak at ~33.5 min was peptide #1 (chapter 4) and peak at 16.0 min is assigned as [Leu-Ala-Gly-Val-Ala-NH=CH-Fc]$^+$ (mass of 625.288).

Based on the observed mass of 625.043 found in the mass spectrum of this 33.5-min. peak, it is proposed to derive from a loss of H_2 (from beta-elimination of the N*H* and C*H*$_2$-Fc) following protonation by H^+. Based on these results, we conclude that cathepsin B cleaves peptide #2 (chapter 4) between Leu-Ala and peptide #1 (chapter 4) between Pro-Leu. Previously, cathepsin B was found to cleave peptide #3 (chapter 4) in two places: between the Gly-Ala residues and between the Phe-Gly residues.[28]

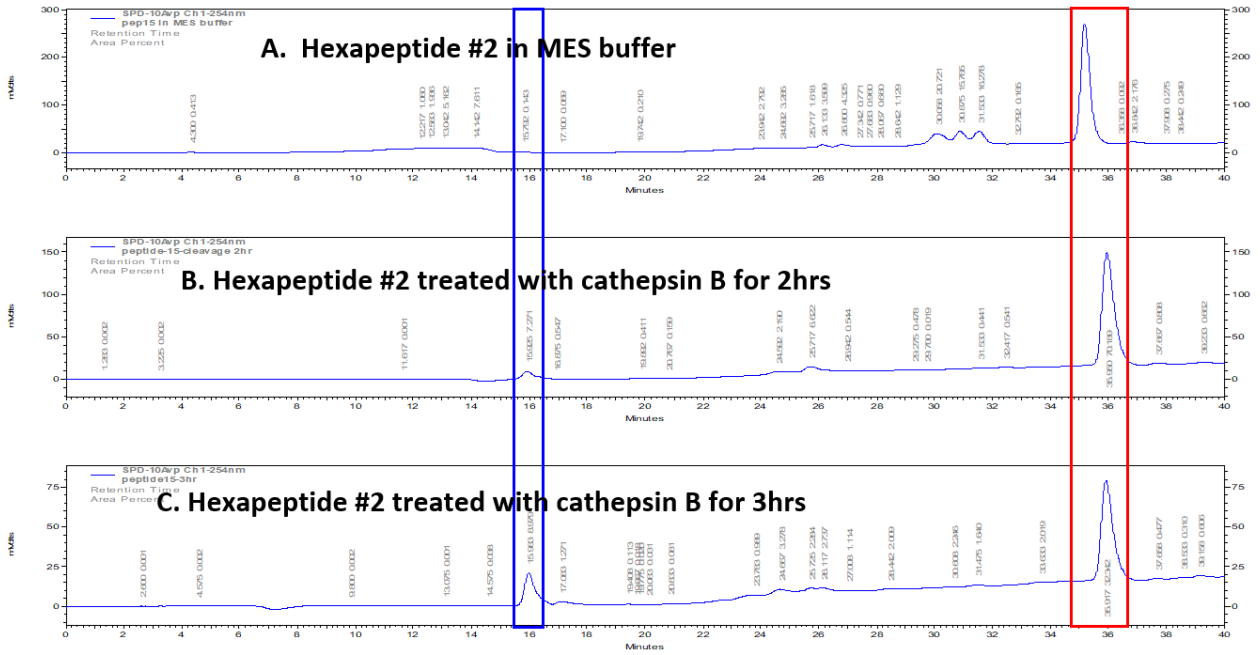

Figure A. 5 Determination of cleavage sites of the peptide #2, H_2N-$(CH_2)_4$CO-Pro-Leu-Ala-Phe-Val-Ala-NH-CH_2-Fc, using HPLC. All analyte solutions contained 6.5 mM peptide #2, 50 mM MES buffer (pH 5.0) and 250 mM NaCl. (a) Chromatogram of peptide #2 in the aforementioned analyte solution. Peptide #2 appeared at 35.9 min in the chromatogram (highlighted with the red box) as verified by mass spectrometry. (b) Chromatogram of peptide #2 obtained after incubation with cathepsin B for 2 h. The cleaved Ala-Phe-Val-Ala-NH-CH_2-Fc fragment appeared at 16.0 min in the chromatogram (highlighted with the blue box) as verified by mass spectrometry [showing a mass of 626.5 [M+23(Na)] in the mass spectrum]. (c) Chromatogram of peptide #2 obtained after incubation with 5.75 ng/µL (0.17 µM) cathepsin B for 3 h.

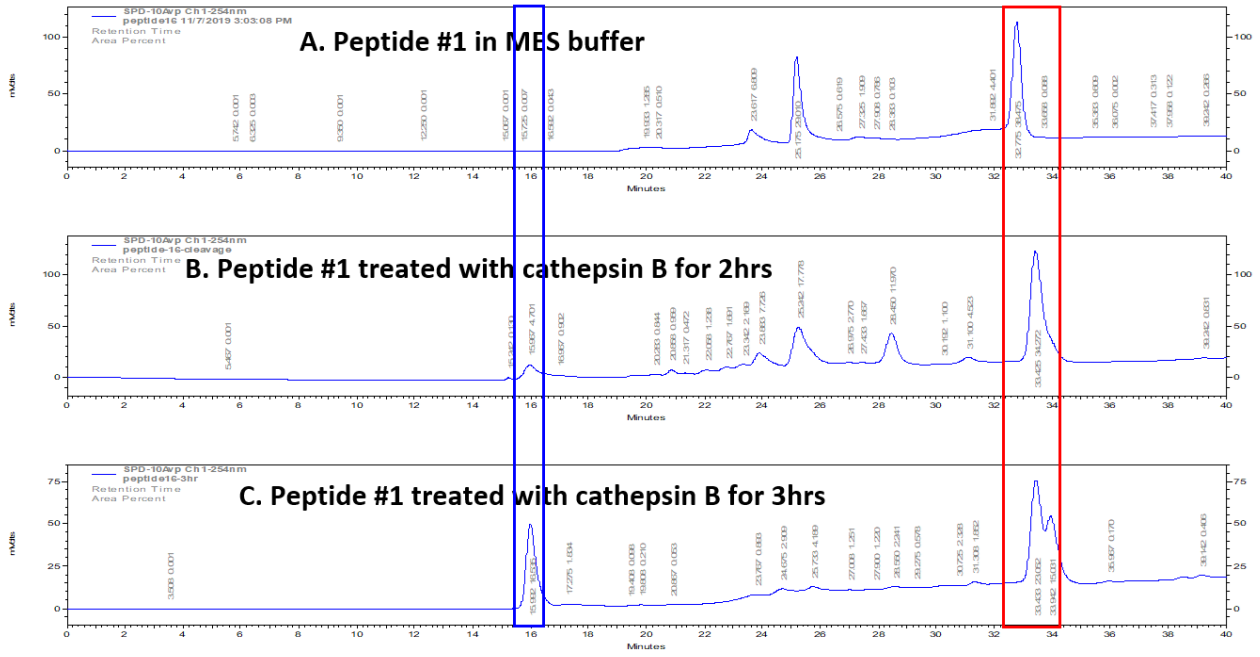

Figure A. 6 Determination of cleavage sites of the peptide #1 using HPLC. (a) HPLC chart of peptide #1, H_2N-$(CH_2)_4$CO-Pro-Leu-Ala-Gly-Val-Ala-NH-CH_2-Fc in 50 mM MES (pH 5.0) and 250 mM NaCl. The hexapeptide appeared at 33.4 min (highlighted by the rex box) in the HPLC chart and its structure was verified by mass spectrometry analysis. (b) HPLC chart from the treatment of hexapeptide #1 with cathepsin B in 50 mM MES (pH 5.0) and 250 mM NaCl after 2 h. The Leu-Ala-Gly-Val-Ala-NHCH$_2$-Fc appeared at 16.0 min (highlighted by the blue box) in the HPLC chart and its structure was verified by MS analysis [showing a mass of 625.043 (M-H_2+1) [Leu-Ala-Gly-Val-Ala-NH^+=CH-Fc] in the mass spectrum]. (c) HPLC chart from the treatment of 6.5 mM peptide #1 in 50 mM MES (pH 5.0) and 250 mM NaCl incubated with 5.75 ng/µl (0.17 µM) cathepsin B for 3 h.